Simulation of the impact of diesel-biodiesel and diesel-HVO (Hydrotreated vegetable oil) fuel blends on regulated and unregulated emissions in a vehicle under Colombian driving cycles.

Víctor Camilo Cuaical Arciniegas

Trabajo de investigación presentado para optar al título de Magíster en Ingeniería Química

Asesor
Felipe Bustamante Londoño, Doctor (PhD) en Ingeniería Química

Coasesora
Ana María Valencia López, Doctor (PhD) en Ingeniería Química

Universidad de Antioquia
Facultad de Ingeniería

Ingeniería Química

Medellín, Antioquia, Colombia

2024

Cita	Muñoz Zapata y Martínez Naranjo [1]
Referencia Estilo IEEE (2020)	[1] V. C. Cuaical Arciniegas, “Simulation of the impact of diesel-biodiesel and diesel-HVO (Hydrotreated vegetable oil) fuel blends on regulated and unregulated emissions in a vehicle under Colombian driving cycles”, Tesis de maestría, Maestría en Ingeniería Química, Universidad de Antioquia, Medellín, Antioquia, Colombia, 2024.

Maestría en Ingeniería Química, Cohorte L.

Grupo de Investigación Catálisis Ambiental.

CONTENTS

1.1 Introduction **9**

1.2 Objectives **11**

1.3 Background **11**

1.3.1 Diesel engine basics 11
1.3.2 Diesel engine emissions 12
1.3.3 Performance Parameters of CI engines 13
1.3.4 Biodiesel 14
1.3.5 Hydrotreated vegetable oil (HVO) 16
1.3.6 Engine modeling 17
1.3.7 Numerical studies of diesel engines using biodiesel-diesel and HVO-diesel blends 18
1.3.8 Kinetic mechanisms for modeling biodiesel combustion 19
1.3.9 GT-Suite 22
1.3.10 Numerical studies using GT-Suite 22
1.3.11 Engine and vehicle models under in dynamic conditions: estimation of emissions 24
1.3.12 Driving Cycles 25
1.3.13 Regulatory framework 27

2.1 Experimental measurements in test cell **29**

2.1.1 Engine bench 29
2.1.2 Calibration of measuring equipment 30
2.1.3 Repeatability 33
2.1.4 Engine maps (emissions and performance) 35

2.2 Modeling **37**

2.2.1. Engine model 37
2.2.2. Engine model calibration and validation 40
2.2.3. Vehicle model 47

3.1 Calibration of the Predictive Combustion Models (DI-pulse) **51**

3.2 Engine model validation **55**

3.3 Calibration of the Predictive Combustion Model (DISRM) **59**

3.3.1 ULSD mechanism selection 59
3.3.2 Biodiesel mechanism selection 62
3.3.3 Selection ULSD surrogate. 64
3.3.4 Biodiesel surrogate selection 67

3.4 Engine simulation results with biodiesel/diesel and HVO/diesel blends **75**

3.4.1 Engine performance 75
3.4.2 Regulated emissions 78
3.4.3 Unregulated emissions 80

3.5 Vehicle model **85**

3.5.1 Model Validation 85

4.1 Conclusions **103**

4.2 Future work **104**

LIST OF FIGURES

Figure 1. Schematic visualization of the Stochastic Reactor Model (SRM) concept. 18
Figure 2. WLTC driving cycle. 26
Figure 3. Driving cycle of light vehicles in Colombia. 26
Figure 4. Driving cycle of light vehicles for the AMVA. 26
Figure 5. Schematic diagram of the diesel engine test bench. 30
Figure 6. NOx verification. 31
Figure 7. CO2 and CO verification. 32
Figure 8. Steady state PN measurements. 34
Figure 9. PN measurement procedure. 35
Figure 10. PN measurement results. 35
Figure 11. Operation points measured for B20 36
Figure 12. Operation points measured for ULSD 36
Figure 13. Methodology followed for engine calibration and validation. 41
Figure 14. Single cylinder model CPOA. 41
Figure 15. Non predictive model. 42
Figure 16. Full engine model 44
Figure 17. General approach to calibrate an engine model. 45
Figure 18. A schematic of the vehicle simulation model in GT-Suite. 48
Figure 19. Results of consistency checks. 51
Figure 20. IMEP error, ULSD-DI-pulse model. 52
Figure 21. IMEP error, B20-DI-pulse model. 52
Figure 22. CA50 error, ULSD fuel-DI-pulse model 52
Figure 23. CA50 error, B20 fuel-DI-pulse model. 53
Figure 24. Peak pressure error, ULSD fuel-DI-pulse model. 53
Figure 25. Peak pressure error, B20 fuel-DI-pulse model. 53
Figure 26. CO2 error, ULSD fuel-DI-pulse model 54
Figure 27. CO2 error, B20 fuel-DI-pulse model. 54
Figure 28. NOx error, ULSD fuel-DI-pulse model. 54
Figure 29. NOx error, B20 fuel- DI-pulse model. 55
Figure 30. Engine model validation: combustion parameters. 56
Figure 31. Engine model validation: performance parameters. 56
Figure 32. Engine model validation: emissions. 57
Figure 33. Engine model validation: In-cylinder pressure and burn rate (a) ULSD – (b) B20. . 58
Figure 34. Simulated in-cylinder pressure for each reaction mechanism ULSD. Residuals equals to difference between measured and predicted profiles. 61
Figure 35. Simulated heat release rate for each reaction mechanism ULSD. Residuals equals to difference between measured and predicted profiles. 61
Figure 36. Simulated in-cylinder pressure for each reaction mechanism B20. Residuals equals to difference between measured and predicted profiles. 63
Figure 37. Simulated heat release rate for each reaction mechanism B100. Residuals equals to difference between measured and predicted profiles. 63
Figure 38. Chemical and physical properties error for tested ULSD surrogates. 65
Figure 39. Simulated heat release rate for each ULSD surrogate. Residuals equals to difference between measured and predicted profiles. 66
Figure 40. Simulated in-cylinder pressure for each ULSD surrogate. Residuals equals to difference between measured and predicted profiles. 67

Figure 41. Chemical and physical properties error for tested BD surrogates. 68
Figure 42. Simulated heat release rate for B20 surrogates. Residuals equals to difference between measured and predicted. 70
Figure 43. Simulated in-cylinder pressure for each B100 surrogate. Residuals equals to difference between measured and predicted. 71
Figure 44. IMEP error, ULSD fuel-DISRM. 72
Figure 45. IMEP error, B20 fuel-DISRM. 72
Figure 46. CA50 error, ULSD fuel - DISRM. 73
Figure 47. CA50 error, B20 fuel - DISRM. 73
Figure 48. Peak pressure error, ULSD fuel - DISRM. 73
Figure 49. Peak pressure error, B20 fuel - DISRM. 73
Figure 50. CO2 error, ULSD fuel - DISRM. 74
Figure 51.CO2 error, B20 fuel - DISRM. 74
Figure 52. NOx error, ULSD fuel - DISRM. 74
Figure 53. NOx error, B20 fuel - DISRM. 75
Figure 54. Simulated Brake Thermal Efficiency (a) ULSD, (b) B20 effect, (c) HVO20 effect. 76
Figure 55. Simulated Brake Specific Fuel Consumption (a) ULSD, (b) B20 effect, (c) HVO20 effect. 76
Figure 56. Simulated Volumetric Efficiency (a) ULSD, (b) B20 effect, (c) HVO20 effect. 77
Figure 57. Simulated Mechanical efficiency (a) ULSD, (b) B20 effect, (c) HVO20 effect. 77
Figure 58. Simulated CO2 emissions (a) ULSD, (b) B20 effect, (c) HVO20 effect. 78
Figure 59. Simulated NOx emissions (a) ULSD, (b) B20 effect, (c) HVO20 effect. 79
Figure 60. Simulated HC emissions (a) ULSD, (b) B20 effect, (c) HVO20 effect. 80
Figure 61. Simulated CO emissions (a) ULSD, (b) B20 effect, (c) HVO20 effect. 80
Figure 62. Simulated naphthalene (A2) emissions (a) ULSD, (b) B20 effect, (c) HVO20 effect. 81
Figure 63. Simulated phenanthrene (A3) emissions (a) ULSD, (b) B20 effect, (c) HVO20 effect. 81
Figure 64. Simulated pyrene (A4) emissions (a) ULSD, (b) B20 effect, (c) HVO20 effect. 82
Figure 65. Simulated Benzene emissions (a) ULSD, (b) B20 effect, (c) HVO20 effect. 83
Figure 66. Simulated Toluene emissions (a) ULSD, (b) B20 effect, (c) HV20 effect. 83
Figure 67. Simulated formaldehyde emissions (a) ULSD, (b) B20 effect, (c) HV20 effect. 84
Figure 68. Simulated PN emissions (a) ULSD, (b) B20 effect, (c) HVO20 effect. 84
Figure 69. Target and actual vehicle speeds for each simulated driving cycle. ULSD as fuel. AMVA+S stands for the Andean cycle with slope. 85
Figure 70. Experimental and simulated emission factors for WLTC Class 1 cycle. Error bars correspond to the standard deviation. a) CO_2, b) NOx, c) A2, d) A3, e) A4, f) Total PAHs, g) PN 88
Figure 71. Experimental and simulated fuel consumption for WLTC Class 1 cycle. Error bars correspond to the standard deviation. 88
Figure 72. Operating points (OP) required by the vehicle model to follow each driving cycle. 90
Figure 73. Simulated fuel consumption and comparison between fuels under the studied driving cycles. 91
Figure 74. Simulated emission factors of CO2 and comparison between fuels under the studied driving cycles. 92
Figure 75. Simulated emission factors of CO and comparison between fuels under the studied driving cycles. 92
Figure 76. Simulated emission factors of NOx and comparison between fuels under the studied driving cycles. 93

Figure 77. Simulated emission factors of HC and comparison between fuels under the studied driving cycles. 94
Figure 78. Simulated emission factors of PN and comparison between fuels under the studied driving cycles. 94
Figure 79. Simulated emission factors of PAHs and comparison between fuels under the studied driving cycles. 95
Figure 80. Simulated emission factors of Benzene and comparison between fuels under the studied driving cycles. 96
Figure 81. Simulated emission factors of Toluene and comparison between fuels under the studied driving cycles. 96
Figure 82. Simulated emission factors of Formaldehyde and comparison between fuels under the studied driving cycles. 97

LIST OF TABLES

Table 1. Composition of pure fuels. 19
Table 2. Fuel properties. 20
Table 3. Reaction mechanisms and surrogate for diesel. 20
Table 4. Reaction mechanisms and surrogate for biodiesel. 21
Table 5. Maximum permissible emission limits for road land mobile sources classified as light and medium vehicles with compression ignition engines in dynamic testing, evaluated using the European Union cycle (NEDC). 27
Table 6. Engine specifications. 29
Table 7. CAPELEC CAP 3010-4G gas analyzer technical specification. 30
Table 8. Error in NOx concentration. 31
Table 9. Error in CO2 and CO concentrations. 32
Table 10. Results of repeatability tests. 33
Table 11. Data required to build the engine model. 37
Table 12. DI-Pulse multipliers range. 43
Table 13. Recommended NOx calibration limits. 43
Table 14. Model accuracy targets. 46
Table 15. Parameters of the simulated vehicle. 48
Table 16. Speed thresholds for the gear-shifting strategies. 49
Table 17. Correlation (R) and Determination (R2) coefficients for all compared parameters. 57
Table 18. DISRM multipliers. 59
Table 19. Results of preliminary testing to select USLD mechanism. 60
Table 20. Results of preliminary testing to select a biodiesel mechanism. 62
Table 21. ULSD surrogates. 64
Table 22. Consistency checks and simulated results for ULSD surrogates. 65
Table 23. B100 surrogates. 68
Table 24. Consistency checks and simulated results for B20 surrogates. 69
Table 25. Merged mechanism and surrogates for ULSD, B20, HVO20. 71
Table 26. Correlation (R) and Determination (R2) coefficients for all driving cycles with both fuels, ULSD and B20. 86
Table 27. Recommended settings for search algorithm. 119

Abstract

Vehicle exhaust emissions, a significant challenge in densely populated urban areas, adversely impact air quality and human health. The use of renewable fuels, particularly biodiesel (BD) and hydrotreated vegetable oil (HVO), has emerged as a promising solution. BD, blended seamlessly with fossil diesel, is gaining popularity globally, with over 60 countries that have implemented their use. In Colombia, a palm oil biodiesel industry aligns with the nation's commitment to sustainability. Resolution 40103 of Colombia further supports renewable fuels, encompassing not only BD but also HVO, an innovative renewable diesel, which exhibits superior properties compared to traditional biodiesel, resulting in reduced exhaust regulated emissions and improved engine performance. However, information regarding emissions of highly toxic and unregulated pollutants, such as Polycyclic Aromatic Hydrocarbons (PAHs) and carbonyls, remains limited. Furthermore, evaluating emissions under both steady-state and transient conditions is crucial for understanding the true impact of renewable fuels. In particular, Colombian driving cycles, representative of heavy traffic conditions in urban areas, could play a pivotal role in assessing impact of biofuels on performance and emissions.

This research, through modeling and simulation using GT-Suite, evaluates the effects of diesel-biodiesel and diesel-HVO fuel blends on both regulated and unregulated emissions under actual Colombian driving conditions. The study focuses on 20 vol.% blends (B20 and HVO20), chosen for their representativeness in balancing operability, performance, and regulated emissions benefits. The methodology involves a comprehensive review of the literature, input data collection, experimental measurements, construction and calibration of models, and analysis of results. While the engine model shows high precision in predicting combustion emissions for regulated pollutants and performance parameters, predicting unregulated emissions remains challenging. The vehicle model, however, exhibits a strong correlation between simulated results and experimental measurements, particularly under transient conditions. It was found that the use of B20 led to a decrease of 27 – 35% in particle number (PN) emissions, and 12 – 20.5% in unburned hydrocarbon (HC) emissions with respect to Ultra Low Sulfur Diesel (ULSD), while the effect was not significant in carbon monoxide (CO) and carbon dioxide (CO_2), and a slight increase in nitrogen oxides (NOx) emissions was observed. The use of B20 decreased PAH emissions by up to 33.2%, while it did not have a significant impact on carbonyl emissions. The use of HVO20 did not have a significant impact on CO, CO_2, NOx and PN emissions, while a positive impact was observed on HC emissions, with reductions ranging between 15.6% and 19.5%. Consideration of road slope within the driving cycle had the most significant effect on emissions, increasing them with all fuels. The results of this study aim to provide valuable insights into the environmental performance of alternative fuel blends, considering the Worldwide harmonized Light vehicles Test Cycle (WLTC) and unique characteristics of Colombian driving cycles and their implications for the transportation sector.

Chapter 1. Introduction and Background

1.1 Introduction

Pollution from vehicle exhaust emissions represent a significant challenge in densely populated urban areas, where mobile sources, including diesel vehicles, are major contributors to pollutant emissions [1]. This adversely affects air quality and human health [2]. To mitigate these environmental and health concerns, the use of renewable fuels has appeared as a promising alternative.

Biodiesel (BD) has shown potential for reducing emissions of certain regulated pollutants, such as particulate matter (PM), unburned hydrocarbons (HC), and carbon monoxide (CO). Furthermore, it can be directly incorporated to fossil diesel in different amounts, with no need for engine adjustments for blends up to 20 vol.% BD [3]. Thus, biodiesel has become increasingly popular as a replacement for petroleum-based diesel in transportation, and more than 60 countries have BD blending mandates, including Indonesia (B20), the United States (up to B10 in some states), Argentina (B10), and Brazil (B10) [4]. In Colombia, a palm oil biodiesel (methyl esters of fatty acids) industry has been established to partially replace diesel and reduce polluting emissions, particularly PM, in diesel engines. This initiative aligns with the country's commitment to promoting sustainable practices and reducing its carbon footprint. In 2021, Resolution 40103 expanded the range of biofuels accepted for mixtures, encompassing not only biodiesel but also renewable diesel (hydrotreated oils of vegetable or animal origin HVO). This regulatory step further encourages the adoption of renewable fuels in transportation.

HVO is an innovative, globally produced, renewable diesel obtained from renewable raw materials by the hydrotreatment technique. In comparison to Fatty Acid Methyl Ester (FAME) biodiesel, HVO exhibits enhanced properties, such as a greater cetane number, improved ability to flow in cold temperatures, and exceptional stability against oxidation during storage. The literature shows that HVO and HVO blends with fossil diesel typically result in reduced exhaust emissions and improved engine performance, particularly, significant decrease in NOx, particle mass (PM), CO, and HC emissions has been documented on heavy-duty engines. The reduction of CO, HC and PM emissions is directly proportional to the amount of HVO in the diesel biofuel blends [5].

Despite generally positive reports on regulated emissions with the use of BD and HVO, information about emissions of highly toxic and unregulated pollutants, including polycyclic aromatic hydrocarbons (PAHs), carbonyls, benzene, and toluene, remains limited and inconclusive [6], [7], [8]. For example, carbonyl emissions such as formaldehyde and acetaldehyde increased or decreased depending on BD fraction and source. In several studies, a shorter combustion duration reduces toluene and xylene emissions for biodiesels/diesel blends, but benzene emissions increased, where both engine operating conditions and physicochemical properties of the fuel play a key role in forming those emissions [7], [8], [9], [10].

Evaluating emissions under both steady-state and transient conditions is essential for understanding the true impact of renewable fuels and their blends. While steady-state conditions offer a controlled setting for precise emission measurements, transient conditions mirror real-world driving scenarios, capturing the dynamic nature of emissions during acceleration, deceleration, and varying loads [11], [12]. Furthermore, incorporating road slope can significantly increase NOx and CO_2 emissions, along with fuel consumption [13]. Driving cycles play a pivotal role in assessing vehicle performance in terms of fuel consumption and pollutant emissions [14].

For diesel vehicles, the Worldwide harmonized Light Vehicles Test Cycle (WLTC) and the US legislative cycle FTP-75 are widely used [15]. However, ideally, driving cycles should be region-specific, reflecting the differences in vehicle fleet composition, traffic patterns, driving habits, and topography. Consequently, several studies have focused on developing local driving cycles [16], [17], [18]. In Colombia, representative driving cycles have been developed for each vehicle category (motorcycles, light vehicles, buses, and trucks). These cycles were specifically designed for Colombia's largest cities [19]. Compared to the WLTC, Colombian driving cycles exhibit lower speed ranges and incorporate more stop-and-go events, even during the middle and high fluid traffic phases, accurately reflecting the heavy traffic conditions prevalent in urban areas. Additionally, the driving cycle for light vehicles incorporates steep slopes, with some exceeding 10% grades.

Modeling and simulation facilitate the evaluation of exhaust emissions from combustion engines under several operational scenarios (real driving conditions with different fuels), while time and costs are saved in comparison with the experimental tests. The combustion process is the most important aspect of an internal combustion engine, so its modeling is of great relevance when simulating its behavior. Combustion models are usually classified according to the spatial representation of the process. 3D models have high prediction accuracy in terms of engine performance and (mainly) regulated emissions; several commercial codes have been increasingly used, such as SPEED®, FLUENT® and KIVA® [20], [21], [22] to simulate internal combustion engines fueled with biofuels mixtures [23], [24], [25]. These models simultaneously solve the mass and heat conservation equations and the kinetic equations that describe the consumption and production rates of the distinct species, considering the pressure and temperature fluctuations inside the engine. However, their high computational cost makes them unviable for evaluating a large number of operating conditions and complex Chemical-Kinetic Mechanisms [25]. In contrast, 0 and 1D methods provide a valuable alternative. By simplifying engine geometry and physics into one or fewer dimensions, these methods enable significantly faster simulations. This computational efficiency makes them particularly well-suited for real-time applications. Under this approach, GT-Suite® is a software that has stood out for being widely used and accepted in the automotive industry and in the academic world.

This research project seeks to assess and quantify the effects of diesel-biodiesel and diesel-HVO fuel blends on both regulated and unregulated emissions under actual Colombian driving conditions by means of simulations of the engine and the vehicle using the software GT-Suite, with 20 vol.% biofuel blends. These blends were chosen as highly representative, as they provide a good balance between operability, performance, and regulated emissions benefits. A methodology was developed for the simulation of performance parameters and emissions of regulated (CO, NOx), unregulated (PAH, carbonyls and PN) and CO_2 pollutants from a diesel engine and vehicle using diesel-biodiesel mixtures, which involves a review of the literature, input data collection, experimental measurements, model construction, model calibration and validation, and finally the analysis of results. The engine model demonstrates the ability to predict combustion features with high precision. It also effectively captures the effects of biodiesel-diesel and HVO-diesel blends up to 20% by volume. Although predicting unregulated emissions remains challenging due to the need to consider multiple phenomena that occur in exhaust systems and aftertreatment units, which are not fully accounted for in the project scope, the model's predictions regarding the impact of biodiesel on unregulated emissions appear reasonable. On the other hand, the vehicle model demonstrates remarkable capability in forecasting emissions and fuel

consumption under transient conditions, exhibiting a strong correlation between simulated results and experimental measurements.

We aim to provide valuable insights into the environmental performance of these alternative fuel blends, considering the unique characteristics of Colombian driving cycles and, therefore, the environmental implications of adopting alternative fuel blends in Colombia's transportation sector.

For the development of this work, the following research question and objectives were established.

¿What is impact of diesel-Palm-biodiesel and diesel-HVO (Hydrotreated vegetable oi) fuel blends on regulated and unregulated emissions of a vehicle under Colombian driving cycles?

1.2 Objectives

General objective

Assess the impact of diesel-Palm-biodiesel and diesel-HVO (Hydrotreated Vegetable Oil) fuel blends on the performance and emissions of a light vehicle under Colombian driving cycles.

Specific objectives

1. Develop a methodology to model the performance and emissions of an engine fueled with diesel-palm-biodiesel and diesel-HVO blends.
2. Evaluate the impact of several operating modes representative of national driving cycles on the performance and emissions of an engine fueled with blends of diesel-palm-biodiesel and diesel-HVO.
3. Estimate regulated and unregulated emissions of a vehicle powered by diesel-Palm-biodiesel and diesel-HVO fuel blends under national driving cycles.

1.3 Background

This section provides a brief overview of internal combustion engines (ICE), emissions from combustion in diesel engines, as well as some key definitions related to engine performance. Then, some biodiesel and HVO features are presented, and details on the combustion models used in this work are provided. The section finalizes with a description of the software used in this work, and the conditions of the simulations (i.e., driving cycles).

1.3.1 Diesel engine basics

The diesel engine has traditionally been the preferred choice for heavy-duty applications in sectors such as construction, agriculture, industry, and on-highway transportation. This preference is attributed to its torque capacity and fuel efficiency, making it well-suited for demanding operational scenarios [26].

Diesel/compression ignition (CI) engines operate on a fundamentally distinct principle than spark ignition (SI) engines, namely, in SI engines combustion is initiated by a spark within the pre-mixed air-fuel mixture, leading to homogeneous combustion ideally occurring at a constant volume, whereas in CI engines fuel is injected into the cylinder during the later stages of the compression stroke, where it mixes with air and undergoes autoignition at the elevated pressure and temperature conditions present inside the cylinder. As a result, different regions of the cylinder may experience different levels of fuel-air mixing, contributing to the heterogeneous

nature of combustion. Combustion in CI engines occurs at a constant pressure, and the output of the engine is controlled by adjusting the volume of fuel injected into the cylinder [26].

The complex combustion process is influenced by fuel characteristics, engine design, and operating conditions. As mentioned before, in diesel engines fuel is injected into the cylinder where it atomizes and mixes with high-temperature air, leading to spontaneous ignition and burning. The pressure increases as combustion continues, compressing the air + burned gases + fuel mixture, aiding ignition, and atomization, vaporization and mixing continue until all fuel is consumed. Diesel combustion relies on diffusion flames, where fuel and air diffuse before reacting, the turbulent flow making the process primarily an unsteady diffusion flame [27].

1.3.2 Diesel engine emissions

Due to heterogeneous combustion and the forming diffusion flames inside the diesel engines, these devices generate a variety of pollutants, including regulated and unregulated emissions. Regulated emissions, unlike the unregulated, are subject to government regulations. Regulated emissions include particulate matter (PM), nitrogen oxides (NOx), carbon monoxide (CO), and hydrocarbons (HC) [28], [29]. NOx emissions, which contribute to photochemical smog formation, are still a challenge in CI engines. According to the NOx Zeldovich extended mechanism, accepted by most researchers, the main condition for NOx formation is the presence of sufficient concentrations of oxygen and nitrogen together with high temperature [30]. NOx are difficult to control in diesel engines because the measures taken to reduce them tend to increase particulate emissions and fuel consumption. One such strategy is exhaust gas recirculation (EGR), where a fraction of the exhaust gases, containing inert species such as CO_2 and water vapor, is directed back into the engine intake manifold. This recycled exhaust gas, having already undergone combustion, does not actively participate in the combustion process within the cylinder. This action leads to a reduction in in-cylinder temperature, subsequently reducing NOx emissions. However, it can also result in the recirculation of soot and other particulate matter from the exhaust into the combustion process, potentially leading to higher levels of particulate matter emitted from the vehicle's tailpipe. Moreover, EGR can adversely affect fuel consumption. By diluting the fresh air-fuel mixture with recirculated exhaust gas, the combustion process may become less efficient, leading to incomplete combustion and decreased fuel efficiency. Consequently, higher fuel consumption rates may ensue.

Soot emission, on the other hand, reflects poor combustion conditions and a loss of efficiency [31], because it is a result of incomplete combustion of fuel. Soot formation in SI engines (which burn homogenously) is small, whereas the heterogeneous combustion in Diesel engines creates fuel-rich pockets whose breakdown leads to the formation of soot. High temperatures towards the end of combustion help burn some of the soot before it can escape to the environment. The chemical mechanisms involved in the soot reduction process are not well understood because of the complicated fuel molecular structure and the lack of in-depth kinetic studies [32].

Emissions from diesel engines contain not only the so-called regulated pollutants (e.g., NOx and soot) but also a variety of unregulated hydrocarbon species, such as Volatile Organic Compounds (VOC) Indeed, diesel exhaust may contain a large number of unregulated species, such as alkanes, aldehydes, benzene, toluene, xylene (BTX), alcohols and ketones [62].

Improving engine performance often involves optimizing combustion, which can reduce emissions. Efforts to address this balance include the development of cleaner and more efficient engine technologies, such as direct injection, turbocharging, variable valve timing, alongside the

use of emission control systems such as diesel particulate filters and selective catalytic reduction (SCR) [26].

1.3.3 Performance Parameters of CI engines

The performance of a diesel engine is evaluated through a set of key parameters that define its efficiency, power output, and overall operational characteristics. These parameters provide insights into the engine combustion efficiency, fuel consumption, emissions reduction, and ability to convert fuel energy into mechanical work. By understanding and analyzing these performance parameters, engine performance and fuel economy can be optimized, as well as reliable operation ensured. In this context, exploring the key performance parameters of diesel engines becomes crucial for both engine design and operation. Some of these parameters are [27]:

Engine Speed (*N*): refers to the rotational velocity of the crankshaft, denoting the number of revolutions made by the engine per unit of time. Engine speed is measured with a rotational encoder.

Engine Torque (*T*): is a rotating force produced by an engine's crankshaft. It is typically measured using a dynamometer where the shaft is linked to the dynamometer rotor through electromagnetic, hydraulic, or mechanical friction, and coupled to a stationary stator which is upheld by low-friction bearings.

Brake power (*Pb*): is the total power generated by the engine and available at the crankshaft. It can be calculated as the product of torque (T) and angular speed (N).

$$Pb = 2\pi NT \qquad \text{Eq. 1}$$

Brake mean effective pressure (*BMEP*): this factor varies with engine size, therefore is used to compare distinct size engines. It can be expressed in terms of torque and displaced volume (V_d).

$$BMEP = \frac{4\pi T}{V_d} \qquad \text{Eq. 2}$$

Indicated Mean Effective Pressure (*IMEP*): is the relationship between the work generated within the cylinder and the volume displaced. It can be visualized as the average pressure exerted on a piston during the various stages of its cycle.

$$IMEP = \frac{\int P dv}{V_d} \qquad \text{Eq. 3}$$

Where P represents the gas pressure data in the cylinder over the operating cycle, and v is the cylinder volume.

Friction Mean Effective Pressure (*FMEP*): it can be defined as the Mean Effective Pressure lost due to the friction. This can be calculated from the Net Mean Effective Pressure and the Brake Mean Effective Pressure.

$$FMEP = IMEP - BMEP \qquad \text{Eq. 4}$$

Mechanical efficiency (η_m): refers to the ratio of the engine's delivered brake power, which is the useful power, to the indicated power. Under full throttle conditions mechanical efficiency is around 90 percent when the engine speed is below approximately 1800 to 2400 rpm and drops to approximately 75 percent at the highest speed. When the engine throttle is adjusted, the mechanical efficiency diminishes, ultimately reaching zero during idle operation.

$$\eta_m = \frac{BMEP}{IMEP} \qquad \text{Eq. 5}$$

Fuel conversion efficiency (η_f): refers to the ratio of work generated to the quantity of fuel energy provided per cycle, which can be liberated during the combustion process.

$$\eta_f = \frac{W}{m_f Q_{LHV}} \qquad \text{Eq. 6}$$

Where *W* represents the work generated per cycle, estimated by integrating cylinder pressure with respect to the volume.

Brake specific fuel consumption (*BSFC*): is a metric of the effectiveness of an engine in utilizing the provided fuel to generate mechanical output.

$$BSFC = \frac{\dot{m}_f}{Pb} \qquad \text{Eq. 7}$$

Where $\dot{m}_f$ is the fuel consumption as mass flow rate.

Volumetric efficiency (η_v): it is defined as the volume flow rate of air into the intake system divided by the rate at which volume is displaced by the piston.

$$\eta_v = \frac{2\dot{m}_a}{\rho_{a,i} V_d N} \qquad \text{Eq. 8}$$

Where $\dot{m}_a$ is the mass flow rate of air into the cylinder and $\rho_{a,i}$ is the inlet air density. The inlet density may be taken as atmospheric air density (in this case η_v measures the pumping performance of the entire inlet system) or as the air density in the inlet manifold (in this case η_v measures the pumping performance of the inlet port and valve only). From the ideal gas law, the density of dry air $\rho_{a,i}$ can be estimated as a function of pressure and temperature.

Air/fuel ratio (*A*/*F*): ratio between air flow rate and fuel flow rate during the intake process.

$$\frac{A}{F} = \frac{\dot{m}_a}{\dot{m}_f} \qquad \text{Eq. 9}$$

Burn Rate: The instantaneous rate of fuel consumption in the combustion process.

Crack Angle at 50% burned (*CA50*): indicates the crank angle at which 50 % of the heat from combustion has been released.

1.3.4 Biodiesel

The term "biodiesel" commonly denotes an oxygenated type of diesel fuel derived from different sources by transforming triglycerides into methyl or ethyl esters by means of transesterification, a process that involves reacting a triglyceride, found in vegetable oil or animal fat, with a light alcohol (such as methanol or ethanol), yielding glycerin and esters. As methanol is commonly used as alcohol, the biodiesel is typically comprised of methyl esters [33].

Numerous experimental studies have been conducted to explore alternative fuels for compression ignition engines. For instance, the properties and composition of fatty acids from various biodiesel sources have been analyzed, and the performance and emissions have been compared to fossil diesel using different test setups. Typically, alternative fuels are evaluated based on mechanical performance and environmental impact.

Biodiesel can be incorporated in different concentrations into fossil diesel. The expression "biodiesel blend level" (BX) denotes a combination of diesel and biodiesel fuels, encompassing (100 − X) vol. % diesel and X vol. % biodiesel. Generally, biodiesel and biodiesel blends have several advantages, including: no need for engine adjustments for blends up to 20% biodiesel, reduced emissions of CO, PM and unburnt HC compared to regular diesel fuel, and enhanced combustion due to the relatively high (10-12%) oxygen content in biodiesel. However, disadvantages exist as well, such as increased NOx emissions, potential clogging of injector nozzles due to elevated viscosity, and lower heating value in most feedstocks, which leads to higher fuel consumption [3].

Nevertheless, in general, the mechanical performance (including power output, exhaust gas temperature, specific fuel consumption and brake thermal efficiency), which is considered by many researchers to be the most significant, is slightly reduced when using certain biodiesel blends or pure biodiesel [34]. For instance, in a single-cylinder, four-stroke, naturally aspirated, direct-injection engine operating at a constant speed of 1,500 rpm and with a maximum power output of 5.5 kW, no significant changes in engine power were observed for any of the palm-biodiesel and diesel blends assessed (B10-B100). The lower brake specific fuel consumption (*BSFC*) was obtained within the range of B10 to B40 blends. Engine efficiency increased with higher loads, with the B10 blend exhibiting the best performance in terms of engine power, *BSFC* and engine efficiency [35].

Regarding the emissions, [36] reported reductions of up to 9.3% in CO, 3.8% in HC, 6.6% in NOx, and 2.7% in smoke of a single-cylinder, four-stroke, air-cooled diesel engine fueled with palm oil biodiesel + pentanol blends (10 and 20 vol.% pentanol), and palm-oil biodiesel and diesel.

In [37], blends of biodiesel (B20 and B100) and palm oil (PO20) were investigated in a diesel engine. Similar results were observed for thermal efficiency and brake specific fuel consumption (*BSFC*) of biodiesel and oil blends, which were found to be lower and higher than of diesel, respectively. HC and CO emissions decreased for biodiesel blends, while they increased for oil blends, compared to diesel. Additionally, there was a slight increase in NOx emissions for both biodiesel and palm oil blends. Ultimately, it was recommended to use diesel-biodiesel blends containing up to 20 vol. % biodiesel due to the improvement in performance and emissions.

In Colombia, several studies have been conducted to assess the impact of palm-oil biodiesel + diesel blends [38], [39], [40], [41], [42]. A one-zone heat release model was utilized to determine key combustion parameters, including the maximum average pressure and temperature within the combustion chamber, delay time, heat release rate, and combustion duration. It was found that lower concentrations of palm-oil biodiesel (up to 20% BD) yielded environmental benefits, though at a slight cost of fuel consumption and brake efficiency. Notably, a decrease in combustion duration, maximum mean temperature, temperature at exhaust valve opening, and exhaust gas efficiency was observed. Conversely, peak pressure and exergy destruction rate increased. Smoke opacity was significantly reduced (40% to 80%) for all engine loads by halving the biodiesel content in the blend (2.5%, 5%, and 10% for B5, B10, and B20, respectively). Furthermore, the impact on NOx emissions varied, either decreasing or increasing depending on the engine operation conditions [39].

Results of unregulated pollutant emissions — olefins, aromatic hydrocarbons (benzene, toluene, and xylene - BTX), polycyclic aromatic hydrocarbons (PAHs), carbonyls (acetaldehyde, formaldehyde, acrolein, etc.) — are less conclusive. In general, BD from several sources such as

palm, soybean, Jatropha and waste cooking oil showed higher carbonyl emissions compared to baseline diesel, with formaldehyde and acetaldehyde being the major components. The emissions of carbonyl compounds varied with different biodiesel feedstocks and engine operating conditions. Biodiesels exhibited emissions of unsaturated hydrocarbons such as 1,3-butadiene, propene and ethene. Biodiesels and their blends resulted in emissions of aromatic compounds such as benzene, xylene, and toluene, and generally showed reductions in particulate matter (PM) compared to baseline diesel. The reduction in PM emissions was attributed to the oxygen content in biodiesel, which improved combustion efficiency. Overall, biodiesels exhibited different emissions than baseline diesel, with variations depending on the biodiesel feedstock and engine operating conditions [6].

The toxicity and carcinogenicity potential of unregulated emissions [7], [8], coupled with the lack of consensus on their production in engines fueled with biodiesel blends, raises concerns about the ability of these fuels to improve air quality, especially in urban centers. For instance, some studies indicate that exposure to biodiesel particulates might be more toxic than exposure to diesel particulates at equivalent concentrations [9], while it was reported that palm biodiesel presence (B10, B20, B100) decreased PAH compounds in emissions but increased their oxidative potential of ascorbic acid and ecotoxicity (Daphnia pulex mortality test) [43].

1.3.5 Hydrotreated vegetable oil (HVO)

Hydrotreated vegetable oil (HVO) is an innovative, globally produced, renewable diesel obtained from renewable raw materials by the hydrotreatment technique. In comparison to Fatty Acid Methyl Ester (FAME) biodiesel, HVO exhibits enhanced properties, such as a greater cetane number, improved cold flow properties, reduced emissions, and exceptional stability against oxidation during storage due the absence of oxygen [44].

The literature shows that HVO and HVO blends typically result in reduced exhaust emissions and improved engine performance, particularly, significant decrease in NOx, PM, CO and HC emissions has been documented on heavy-duty engines. The reduction of CO, HC and PM emissions is directly proportional to the amount of HVO in the diesel-biofuel blends [5].

Due to its unique paraffinic characteristics, engine normal operating parameters are not ideal for HVO combustion and fine tuning of the engine settings will likely result in improved reduction of some exhaust emissions. In [45], the HC, soot, CO, CO_2 and NOx emissions of HVO in a light-duty Euro 5 diesel were studied under steady-state operation, as well as with the New European Driving Cycle, adjusting Main Injection Timing (MIT) and EGR rate, and comparing the results with those of standard diesel fuel. The use of HVO led to a considerable reduction in all regulated emissions with MIT and EGR set to their default values, while further MIT and EGR adjustments can improve HVO potential for emissions reduction. Similarly, the energy and environmental performance of different HVO-diesel and fatty acid methyl ester (FE)-diesel blends was studied in [46] at various engine loads (BMEP) with identical start of injection (SOI) for all fuel types. It was found that HVO blends yielded the lowest NOx emissions and thermal efficiency, along with no significant differences in CO emissions. Additionally, HVO demonstrated lower CO_2 emissions compared to other blends and diesel fuel. While blends with higher levels of FE produced more NOx and had poorer thermal efficiency than diesel.

The toxicity and mutagenic potential (ability of a substance or agent to induce changes or mutations in the genetic material (DNA) of an organism) of HVO blends has also been studied [47]. A Euro 5 1.3L passenger car (diesel engine) was fueled with Ultra Low Sulphur Diesel (ULSD) and 30% vol of biofuel blends (Rapeseed Methyl Ester - RME and HVO). A characterization of chemical composition, mass, particle number, size distribution and mutagenic potential of the Particulate Matter (PM) was conducted, finding that biofuel blends, RME30 and HVO30, have small impact on particle number distributions compared to regular diesel. In addition, the mutagenic potential of PM samples of RME30 was lower among the tested fuels, while HVO30 blend displayed the highest genotoxic activity, indicating its strongest potential to induce genetic changes or mutations.

1.3.6 Engine modeling

Numerical simulations can reduce the costs of design and development of new engine technologies. Several approaches are available, all varying in computation time and accuracy, and it is up to the engine designers to choose the right method to strike a reasonable balance between computational time and accuracy.

Multidimensional models or CFD (Computational Fluid Dynamics) are models that have the potential to individually describe each of the physical and chemical phenomena that take place in the injection-combustion process. These are based on the numerical solution of the differential equations that govern the processes occurring inside the combustion chamber, and typically use two main reference frameworks: the continuous Eulerian description, and the discrete Lagrangian description; the latter is the most used because it has certain advantages from the point of view of numerical solution [23]. The 3D models have a high accuracy of prediction in terms of the performance of engine and emissions, but the exceedingly high computational cost make them unfeasible for evaluating large number of design and operating conditions.

A zero dimensional (0D) numerical method, on the other hand, can provide a computationally inexpensive alternative. These models, based mainly on the conservation of energy, assume spatial homogeneity of the variables involved in the process, and can be broadly classified into two categories: thermodynamic models and phenomenological models. Thermodynamic models assume a single combustion chamber zone with a mixture of different chemical species, employing empirical submodels to predict heat release rate. Phenomenological models divide the chamber into multiple zones with different temperature and composition to consider processes such as spray dynamics and combustion chemistry and solve mass and energy conservation equations for each zone [48]. However, the lack of detailed chemistry sub-models impact the quality of engine-out emission predictions.

One promising alternative to conventional 0-D simulations that incorporate both turbulent mixing and detailed chemistry is the Stochastic Reactor Model (SRM). Unlike traditional approaches, SRM operates within a computational domain where the trapped mass within the cylinder is discretized into a multitude of particles. These particles are capable of both inter-particle mixing and heat exchange with the cylinder walls. ***Figure 1*** offers a visual representation of this concept, including a sample distribution of key particle properties like enthalpy or gas composition. At Intake Valve Closure (IVC), each particle is assigned specific initial conditions based on the

overall system state, including chemical composition, temperature, and mass. However, pressure is assumed to be uniform across all particles within the model [49].

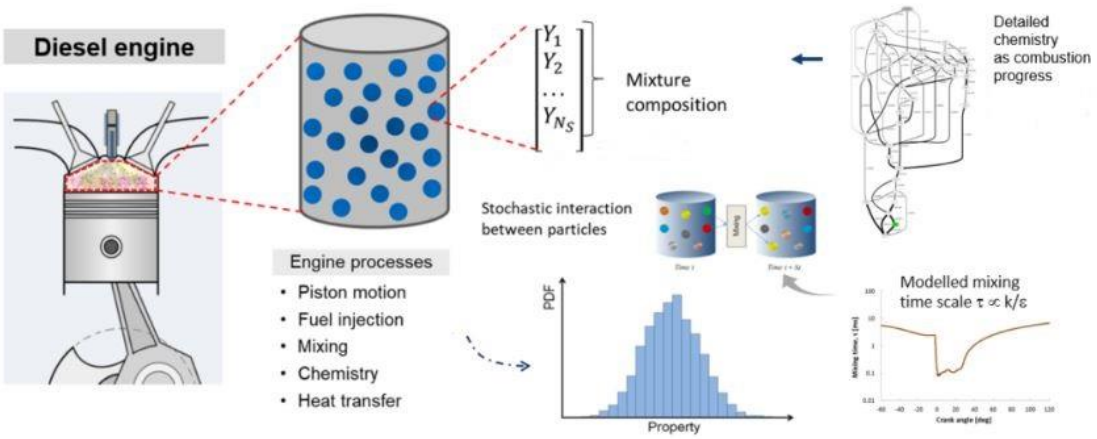

Figure 1. Schematic visualization of the Stochastic Reactor Model (SRM) concept.

1.3.7 Numerical studies of diesel engines using biodiesel-diesel and HVO-diesel blends

The development of combustion technologies with higher efficiencies and lower polluting emissions requires a fundamental understanding of fuel oxidation, specifically the processes of formation of unwanted substances. Simulation tools play a fundamental role since they can provide information that is difficult to obtain experimentally and allow to examine different scenarios of engine operation and fuel composition at low costs [50], [51], [52]. However, engine simulation is a large and complex field of research due to the presence of turbulent flows and chemical kinetic limitations. In particular, kinetics plays a key role as it defines the rate of heat release and the formation of pollutants [53].

A variety of models have been developed to simulate a diesel engine operated with blends of biodiesel. For example, Novaes et al. [51] modeled the thermodynamic phenomena of compression, combustion, and expansion in a diesel engine cycle, and performed parametric analyzes of the use of biodiesel blends, time of combustion initiation and equivalence ratio on engine performance. Although the biodiesel source is not specified and emissions are not analyzed, the authors report that the increase in biodiesel content decreases the temperature and pressure inside the cylinder, reducing the mechanical performance of the engine (i.e., work and power obtained). A SRM has been used has been used to study the effect of BD in [24], [25], [54]. For instance, the effect of biodiesel pilot fuel injection pressure on engine performance was investigated with the 'Kinetics & SRM Engine Suite' software based on SRM, using a reduced chemical kinetic mechanism for a biodiesel surrogate, including 71 species and 217 reactions [24]. Although good prediction of the performance was reported, no information about emissions was presented.

The use of multidimensional CFD models has increased in recent years to simulate internal combustion engines using biodiesel blends [55], [56], [57]. These models simultaneously solve the mass and heat conservation equations and the kinetic equations that describe the consumption and production rates of the different species, considering the fluctuations in pressure and

temperature inside the engine. The mesh used for the numerical solution of the equations includes the change of the geometry over time during each cycle, resulting in extremely high computational cost, especially in the presence of a large number of chemical reactions [52], [58].

1.3.8 Kinetic mechanisms for modeling biodiesel combustion

Reliable and complete combustion kinetics is required for proper engine simulation. However, developing detailed kinetic models with a high degree of precision represents a great computational challenge, especially for complex fuels such as biodiesel and diesel + biodiesel blends; for example, ***Table 1*****Table *1*** and ***Table 2*** present the approximate composition of the "pure" fuels of interest in this work and their properties. Therefore, a common practice is the use of representative molecules ("surrogates") or mixtures with physical and chemical characteristics that approximate those of the fuel, so that its injection, vaporization, mixing and combustion can be adequately modeled while computational requirements are reduced [54].

Table 1. Composition of pure fuels.

ULSD (Ultra-Low Sulfur Diesel) (vol. %)	
Aliphatic	76.30
Aromatics	23.70
*** Monoaromatics (wt. %)**	80.41
*** Polyaromatics (wt. %)**	5.97

HVO (Hydrotreated Vegetable Oil) (wt. %)		Palm Biodiesel (wt. %) Methyl-esters (#C: # instaurations)	
Aromatics	0.3	Laurate (12:0)	0.31
Linear Hydrocarbons < C:15	1.99	Myristate (14:0)	1.03
$C_{15}H_{32}$	20.16	Palmitate (16:0)	43.30
$C_{16}H_{34}$	19.82	Stearate (18:0)	4.20
$C_{17}H_{36}$	32.81	Palmitoleate (16:1)	0.15
$C_{18}H_{38}$	23.03	Oleate (18:1)	41.80
C19: and others	2.19	Linoleate (18:2)	9.10
		Linoleate (18:3)	0.15
		Total saturates (%)	48.80
		Total instaurations (%)	51.10

Table 2. Fuel properties.

Properties	Method	ULSD	HVO100	B100	HVO20	B20
Density at 15 °C [kg/m^3]	ASTM D4052-11	861	780.6	875.4	845.61	856.0
Kinematic viscosity at 40 °C [mm^2/s]	ASTM D445-12	4.356	2.92	4.467	3.96	3.731
Lower heating value [MJ/kg]	ASTM D240-09	42.43	44	37.9	42.69	41.5
Cetane number	ASTM D7668-14	51.36	79.5	69	61.87	49.4

Note: BD and HVO derived from palm. [43], [59].

Several authors have proposed different surrogates, both for diesel and biodiesel from different raw materials, considering mixtures of two to six compounds. ***Table 3*** shows the number of species and reactions of the mechanisms proposed for diesel, as well as the fuel surrogate components and the validation conditions.

Table 3. Reaction mechanisms and surrogate for diesel.

#	Mechanism	Species and reactions	Surrogate	Validation conditions
1	(Hernández et al., 2014) [60]	184 species 463 reactions	(wt. %) *n*-heptane: 50/64 Toluene: 50/36	Cylinder pressure and heat release rate (HRR) simulated in homogeneous charge compression ignition (HCCI) engine
2	(Wang et al., 2015) [61]	109 species 543 reactions	(vol. %) Surrogate 1: 85 *n*-heptane 15 toluene Surrogate 2: 70 *n*-heptane 30 toluene	Laminar flame speeds, species profiles in premixed flames, HCCI and direct injection compression ignition (DICI) engine combustion data
3	(Ren et al., 2017) [62]	178 species 758 reactions	(wt. %) *n*-heptane: 80 Toluene: 10 Cyclohexane: 10	Each individual species and surrogate mixtures were validated with ignition delay time
4	(Yu et al., 2018) [63]	74 species189 reactions	(mol %) Dodecane: 36.02 Octane: 7. 50 Isooctane: 31.49 Decalin: 5.49 Toluene: 19. 50	Cylinder pressure and HRR in diesel engine under 40% load
5	(Bai et al., 2020)) [64]	83 species 234 reactions	(mol %) *n*-hexadecane: 41.3 iso-cetane: 36.8	Cylinder pressure and HRR simulated in HCCI engine

			1-methyl naphthalene: 21.9	

In biodiesel surrogates, straight-chain hydrocarbons such as *n*-heptane or *n*-hexadecane are added to compensate for the energy content and C/H ratio of biodiesel [58]. ***Table 4*** shows the number of species and reactions of the mechanisms proposed for biodiesel fuel, as well as the fuel surrogate components and validation conditions.

Table 4. Reaction mechanisms and surrogate for biodiesel.

#	Mechanism	Species and reactions	Surrogate	Validation conditions
1	(Luo et al., 2012) [65]	115 species 460 reactions	(mol %) methyl decanoate (MD): 25 methyl-9-decenoate (MD9D): 25 *n*-heptane: 50	Experimental reactor ignition delay (Jet Stirred Reactor, JSR) data for *n*-heptane and MD, and species profiles of MD. Data from homogeneous systems, 1D flames, and 3D turbulent spray combustion under diesel engine conditions were also used.
2	(Brakora & Reitz, 2010) [66]	69 species204 reactions	(wt. %) methyl decanoate: 32 methyl-9-decenoate: 32.9 *n*-heptane: 35.1	Experimental pressure and HRR curves for Biodiesel, with EGR=0, 4 speeds and high load. It was also validated with NOx exp. data. For diesel, pure soybean BD and B20 blends (SME20 and PME20), simulation results were compared with exp. data on low temperature combustion in an engine (pressure and HRR), and with data on NOx, CO, HC and Indicated specific fuel consumption (ISFC)
3	(Zhang et al., 2020) [67]	156 species 589 reactions	(mol %) methyl decanoate: 25 methyl-9-decenoate: 25 *n*-heptane: 50	Ignition delay times in closed homogeneous reactor and mole fractions of MD, MD9D, *n*-heptane, C_2H_2, CO, O, OH, H, HO_2. Comparisons were made against the predictions of the detailed Lawrence Livermore National Laboratory (LLNL) mechanism.

4	(Bai et al., 2021) [68]	98 species 314 reactions	(mol %) 1,4-hexadiene: 12.7 methyl decanoate: 62.9 methyl-trans-3-hexenoate: 15 *n*-hexadecane: 9.4	Validation with experimental ignition delays in rapid compression and shock tube machines, and with species concentration in JSR, laminar flame velocity and flame rise length in a constant volume combustion chamber. Also validated with diesel engine data (pressure and HRR).

As shown in Table 1, the main difference between the ULSD and HVO is the large content of aromatics in ULSD. Therefore, to simulate the combustion of an HVO+ULSD blend the diesel surrogate should contain at least one aromatic compound, otherwise, there would be no distinction between the surrogates for ULSD, HVO and their blends.

Inasmuch as no studies incorporating detailed kinetic mechanisms have reported ULSD-HVO blend surrogates in engine models, a simplified approach is adopted here. Since the primary difference between the fuels, as shown in Table 1, lies in the aromatic content, the existing ULSD surrogate can be used as a base, with adjustments made to the aromatic content to reflect the specific blend properties. However, it's important to acknowledge the limitations of this approach. While adjusting aromatic content captures a crucial difference between ULSD and HVO, other chemical properties of HVO blends might influence combustion behavior. These properties are not captured by simply modifying the aromatic content in the surrogate model.

1.3.9 GT-Suite

The simulations of this work were performed with the software GT- Suite®, developed by Gamma Technologies. It is a complete set of simulation tools for engine and vehicle systems that includes a wide range of validated component libraries that can be used to model the various systems of an engine or vehicle. The library developed for engine simulation is GT-Power. It operates in a 1D simulation environment, solving the 1D unsteady, nonlinear Navier-Stokes equation. It integrates thermodynamic and phenomenological models to include factors such as combustion, heat transfer, evaporation, turbulence, or tailpipe emissions [69]. Furthermore, the GT-Suite Vehicle Library provides a set of standard driveline components and connections that can be used to construct various driveline layouts and configurations [70]. This is a software that has stood out for being widely used and accepted in the automotive industry and in the academic world.

1.3.10 Numerical studies using GT-Suite

GT-Suite is a leading engine and vehicle simulation tool used by engine makers and suppliers. It is suitable for analysis of a wide range of issues related to vehicle and engine performance [70]. The incorporation of predictive combustion models has improved the capability in emission prediction. Recently, a zero-dimensional stochastic reactor model (0DISRM) was developed by

GT, using the transported Probability Density Function (tPDF) method, which it is often used in 3D-simulation of combustion systems to capture the turbulence and chemistry interaction effects. In this model the in-cylinder mass (including injected spray mass and intake flow mass) is divided among hundreds of particles of different composition and temperature, depicting the thermal and composition stratification more accurately which, in turn, helps to improve emissions predictions [70].

McCrady et al. [71] developed a model in GT-Suite to analyze the performance and NOx emissions of different types of diesel and biodiesel fuels, using the so-called Direct Injection- Jet (DI-Jet) model and the Extended Zeldovich mechanism. The engine model was calibrated to match burn rate data from a previous work, but NOx emissions were not compared with experimental data. The results showed BD leads to higher In-cylinder pressures and temperatures, and as a consequence higher NOx emissions. Rahim et al. [72] evaluated the performance of a diesel engine with a 1D simulation of a four-cylinder diesel engine using several types of fuels and blends (straight vegetable oil (SVO), biodiesel 20 vol. % blend (B20) and biodiesel 5 vol. % blend (B5)). Although no emissions were reported, this study provides relevant information on the data required for the construction of an engine model in GT. A similar study was developed in [73] to predict engine performance when operating on different blends of soy BD and ULSD. The simulation utilized detailed physical and chemical properties of the blends to estimate cylinder pressure, fuel consumption, and emissions of NOx. DI-Jet was also used as combustion model and the Extended Zeldovich mechanism for NOx prediction. Interestingly, the model was calibrated for the engine at two operating points using ULSD fuel and allows the user to change fuel properties to assess the impact of variations in blend composition on exhaust emissions, which suggests that a calibration for each blend is not required. The predicted results in fuel consumption and NOx emissions showed comparable trends.

Even though other studies have modeled engines with biodiesel [74], [75], [76] very little attention has been paid to other emissions, most of the cases just analyzing the influence on mechanical performance and NOx. In contrast, [77] presents emissions modeling and testing of a four-stroke, single cylinder diesel engine using pure soybean, cottonseed, and algae biodiesel fuels, using the DI-Jet modeling technique. The GT-Power predictive combustion simulation was primarily developed to predict the NOx emissions using the Extended Zeldovich mechanism, while the rest of emissions were calculated using equilibrium chemistry, and, consequently, there were some relatively large differences between predicted and measured emissions in some tests. Similarly, Ahmadipour et al [78] simulated a six-cylinder engine with GT-Power to study the effect of injection timing and fuel type on performance and engine exhaust emissions; the model was validated with experimental data of specific fuel consumption and engine power at 8 different operation conditions. Emissions of CO, CO_2, HC, and NOx were compared at different injection timings, but experimental emissions results were not included in the calibration and validation process. The use of pure BD leads to reductions of CO and HC up to 83.88% and 64.87% respectively.

Despite the growing interest in Hydrotreated Vegetable Oil (HVO) as a promising alternative fuel, numerical studies using GT-Suite remain scarce. To address this gap, a recent study [79] developed two engine models representing the same architecture fueled with either diesel or HVO. Calibration and validation were conducted against experimental data for the combustion (DI-Pulse) and emissions (NOx, soot) models. The results were highly encouraging, displaying excellent agreement between predicted and measured values for both fuels across key parameters: fuel economy, emissions (NOx and soot), and ignition and combustion characteristics. This

demonstrates the effectiveness of GT-Suite simulations in modeling HVO performance, potentially streamlining the extensive experimental testing often required for model calibration and validation.

However, it's important to note that the aforementioned study did not delve into the specific effects of HVO on engine performance and emissions. Exploring these areas using a numerical approach could provide valuable insights and accelerate the adoption of HVO as a sustainable fuel option.

Based on this literature review, several key points can be drawn about GT-Suite simulations involving biodiesel/ULSD-HVO/ULSD fueled engines:

1. Limited Scope: Most studies primarily focus on performance analysis and comparisons of regulated emissions. Broader aspects, including impacts on unregulated emissions.
2. Combustion Model Choice: The DI-Jet model is a common choice, but it relies on a multizone approach with equilibrium chemistry for emission calculations. This limits its ability to capture the detailed chemical reactions involved in fuel combustion, potentially affecting the accuracy of predictions.
3. Limited Exploration of BD Effects: While studies investigate the effects of biodiesel (BD) on performance and emissions under specific operating conditions, a comprehensive understanding of BD's interaction with engine speed and load remains elusive. This gap hinders the development of robust predictive models for diverse operating scenarios.

The literature review highlights the need for future research efforts to address these limitations:

- Expand the scope of simulations to encompass unregulated emissions alongside regulated emissions.
- Explore more advanced combustion models that incorporate detailed chemistry calculations, potentially providing more accurate predictions of emissions and combustion behavior.
- Conduct comprehensive studies to map the influence of BD on engine performance and emissions across a wider range of operating conditions, particularly varying engine speed and load.
- Such advancements will contribute to a deeper understanding of biodiesel/ULSD and HVO/ULSD blends impact on engine performance and emissions, ultimately paving the way for its more informed and efficient utilization.

1.3.11 Engine and vehicle models under in dynamic conditions: estimation of emissions

One of the most frequently used methods to simulate fuel consumption and vehicle emissions under transient conditions is to map the steady-state emissions as a function of the load and speed, and then perform interpolations assuming that the engine moves through a series of "quasi-stationary" state conditions [80]. However, the production of pollutants is highly dependent on dynamic effects such as the rate of change of the load, hysteresis phenomena [55], and the transient behavior of emission control systems (e.g., catalysts, control valves, exhaust gas recirculation, etc.), which should ideally be considered for the simulation of real driving conditions [81], [82]. For example, Pelkmans et al. [82] developed a tool for simulating the fuel consumption and regulated emissions (CO_2, CO, THC, NOx, and PM) of a vehicle under real conditions --the VeTESS Vehicle Transient Emissions Simulation Software-- based on the calculation of the power required by the engine to drive a given vehicle on a particular route

including the transient effects. The traditional maps in three dimensions (pollutant vs load vs speed) were complemented with the change in the throttle position to involve the dynamic performance of the engine by calculating the transient fuel consumption and emissions as time integrals during the driving cycle.

On the other hand, Ericson et al. [83] presented a transient correction model that considers the delay introduced by the turbocharger with the resulting variations in air flow, and consequently in air-fuel ratios, lower than those predicted by the stationary maps. The model estimates a transient air-fuel equivalence relationship at each time step and is used to offset the emissions of regulated pollutants that are initially estimated as extrapolations from quasi-stationary maps. Another method for correcting the steady-state maps and estimating regulated emissions from transient state engines was proposed by Gao et al. [84] based on the combination of a global dynamic lag for exhaust temperature with an index of engine heating, to interpolate the instantaneous fuel consumption and pollutant emissions based on recent operating histories. In this way it is possible to estimate the current state of exhaust gases and their rate of change over time with hot or cold starting conditions and tracking the intermediate conditions. The authors reported that the proposed methodology correctly predicts general trends in emissions, exhaust gas temperature, and fuel economy in both gasoline and diesel engines under real driving cycles. However, transient experimental data, such as time constants for the relevant processes, as well as hot and cold limit states appropriate for each engine are necessary to apply this method.

1.3.12 Driving Cycles

A driving cycle is a speed-time profile for a vehicle operating under specific conditions, typically chosen to simulate a real-world scenario. Driving cycles have long been used by concerned parties, for instance, to estimate fuel consumption for a particular location [32]. In fact, driving cycles are primarily employed in research and regulatory contexts in type-approval tests to certify vehicle emissions. In particular, different internationally standardized engine dynamometer cycles have been developed to certify engine emissions of heavy-duty and non-road engines, including the World Harmonized Stationary Cycle (WHSC), World Harmonized Transient Cycle (WHTC), and Non-Road Transient Cycle (NRTC). Moreover, a globally standardized test procedure for motorcycle emissions has been established, namely, the World Motorcycle Test Cycle (WMTC). Each of these driving cycles has its own advantages and disadvantages. For instance, the New European Driving Cycle (NEDC), comprising several steady-state test modes, is relatively straightforward to operate and repeatable, but does not adequately represent pollutant emissions and fuel consumption due to its failure to mirror real driving behavior in actual traffic. Thence, the Worldwide Harmonized Light-Duty Driving Test Cycle (WLTC) (***Figure 2***) was developed to estimate exhaust emissions and fuel consumption more accurately under actual driving conditions. This cycle has been used as part of a global certification procedure since 2014 [85].

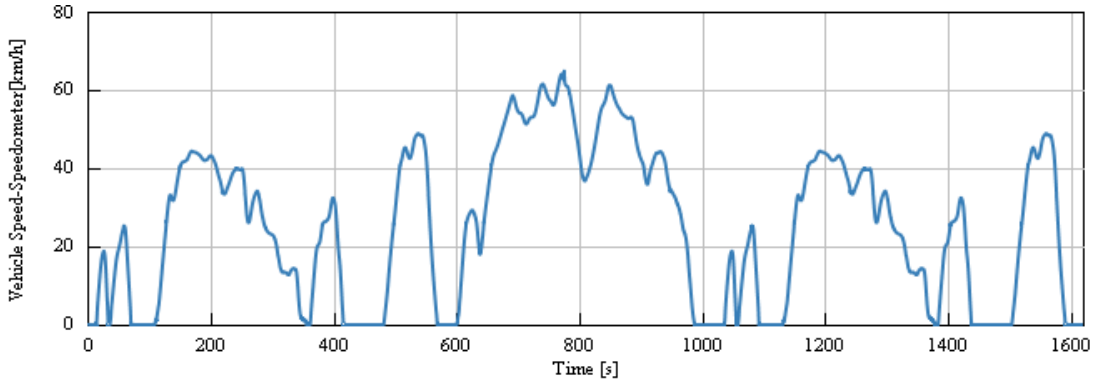

Figure 2. WLTC driving cycle.

In Colombia, representative driving cycles have been developed for each vehicle category (motorcycles, light vehicles, buses and trucks). For each cycle, three groups were identified based on traffic patterns: congested (low traffic speed, high gear changes), fluid (high traffic speed with long micro-trips and few gear changes), and mixed. These cycles were developed for the largest cities in Colombia [19]. ***Figure 3*** shows the driving cycle for the light vehicle category.

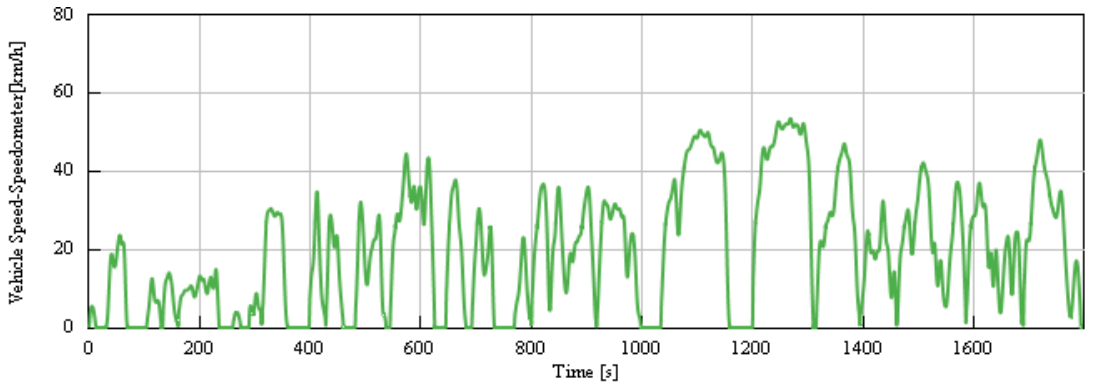

Figure 3. Driving cycle of light vehicles in Colombia.

Furthermore, a driving cycle for light vehicles (less than 3.8 tons) and another for motorcycles were developed [86]. Each cycle comprises 5 micro trips that reflect distinct driving characteristics within the Metropolitan Area of the Aburrá Valley (AMVA). Each micro trip corresponds to actual on-route measures, and, as such, each is associated with the specific slope of the section traveled. ***Figure 4*** illustrates the light-vehicle cycle along with the corresponding topographic slope that should be replicated.

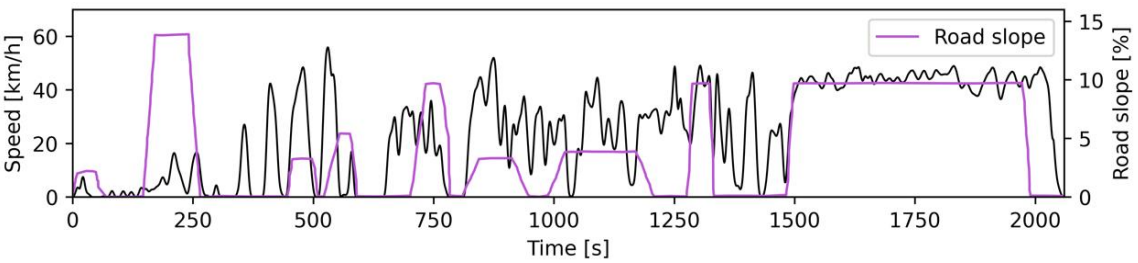

Figure 4. Driving cycle of light vehicles for the AMVA.

Compared to the WLTC, Colombian driving cycles have lower speed ranges and include more stop-and-go steps, even during the middle and high fluid traffic phases, which is representative of heavy traffic in urban areas. In addition, the driving cycle of light vehicles for the AMVA includes

steep slopes, some reaching grades higher than 10%.

1.3.13 Regulatory framework

Colombia has implemented policies for incorporating biofuels into gasoline (naphtha) and diesel blends. Biodiesel, specifically, is being mixed with fossil diesel as a state initiative to reduce pollutant emissions and reliance on petrofuels. Produced from palm oil cultivated by large oil companies. Resolution 40111 of 2021 establishes the maximum biofuel content in the mixture with fossil diesel fuel at the national level which must have a percentage of 90% in the mixture (per gallon or liter) and 10% biofuel-biodiesel, while Resolution 40103 establishes parameters and quality requirements for diesel fuel (ACPM), biofuels, and their blends in compression ignition engines. Notably, a recent modification expands support for renewable fuels beyond biodiesel to include HVO.

The Colombian Ministry of Environment and Sustainable Development plays a crucial role in safeguarding national air quality. They oversee general environmental regulations, aiming to control and reduce atmospheric pollution throughout the country. Additionally, they define and manage administrative instruments and mechanisms for preventing and controlling factors that contribute to environmental degradation.

Resolution 762 of 2022 specifically addresses maximum permissible emission limits for pollutants from land mobile sources. This includes, for example, light and medium vehicles with compression ignition engines. These limits are determined through two different test cycles:

- New European Driving Cycle (NEDC)
- United States cycles (FTP)

As of January 1, 2025, light and medium vehicles with compression ignition engines must be evaluated using the World Harmonized Light Vehicle Test Procedure (WLTP). ***Table 5*** provides the maximum permissible emission limits for vehicles evaluated using the NEDC driving cycle. Maximum permissible emission limits for FTP driving cycle can be found in Resolution 762 of 2022.

Table 5. Maximum permissible emission limits for road land mobile sources classified as light and medium vehicles with compression ignition engines in dynamic testing, evaluated using the European Union cycle (NEDC).

Category	Subcategory		CO (g/km)	NOx (g/km)	HC+NOx (g/km)	PM (g/km)
M	**M1**		0.50	0.25	0.30	0.025
N	**N1**	**Class I**	0.50	0.25	0.30	0.025
		Class II	0.63	0.33	0.39	0.040
		Class III	0.74	0.39	0.46	0.060

Category M: Motor vehicle with at least four wheels, designed and built for the transportation of passengers.

Category M1: Vehicle designed and built to transport up to 8 passengers plus the driver.

Category M2: Vehicle designed and built to transport more than 8 passengers plus the driver and whose gross vehicle weight does not exceed 5 tons.

Category M3: Vehicle designed and built to transport more than 8 passengers plus the driver and whose gross vehicle weight exceeds 5 tons.

Category N: Motor vehicle with at least four wheels, designed and built for the transportation of cargo.

Category N1: Vehicle designed and built to transport cargo, with a gross vehicle weight not exceeding 3.5 tons. This category is divided into three classes according to the reference weight.

Class I: For Euro 3 regulations or higher, any compression ignition Category N1 vehicle with a reference weight less than or equal to 1,305 kg,

Class II: For Euro 3 or Euro 4 regulations, any compression ignition Category N1 vehicle with a reference weight greater than 1,305 kg and less than or equal to 1,760 kg.

Class III: For Euro 3 or Euro 4 regulations, any compression ignition Category N1 vehicle with a reference weight greater than 1,305 kg and less than or equal to 1,760 kg.

Category N2: Vehicle designed and built to transport cargo, with a gross vehicle weight greater than 3.5 tons and not exceeding 12 tons.

Category N3: Vehicle designed and built to transport cargo, with a gross vehicle weight greater than 12 tons.

Chapter 2. Methodology.

2.1 Experimental measurements in test cell

2.1.1 Engine bench

The engine test bench is located in the Thermal Machines Laboratory at the Universidad de Antioquia (Medellín, Colombia). The engine under consideration is a Cummins ISF 2.8 L diesel engine with common rail injection, turbocharging, and intercooling, conforming to the Euro 4 emission standard. The engine specifications are detailed in ***Table 6*****Table *6***.

A piezoelectric pressure transducer (6056A, Kistler, Germany), connected to a charge amplifier (5011B, Kistler, Germany), is used to measure in-cylinder pressure. Crankshaft rotational speed and the instantaneous piston position are determined with an angular encoder providing 1024 pulses per revolution (ROD 426, Heidenhain, Germany). The engine torque output is regulated with an eddy current dynamometer brake (e90 Schenck, Germany). Air consumption is obtained directly from the electronic engine control unit, while fuel consumption is determined using an electronic balance (Shimadzu AUW120D ± 0.01 mg) connected to an NI 9870 monitoring module.

CO_2 and NOx emissions are measured downstream the Diesel Oxidation Catalyst (DOC) and muffler by means of a CAPELEC CAP 3010-4G gas analyzer. Furthermore, particle number concentration (>23 nm aerodynamic diameter) is gauged using a Pegasor PPS-M sensor. **Figure *5*** provides a visual representation of the diesel engine test bench setup.

Table 6. Engine specifications.

Type and Configuration	Cummins ISF 2.8, 4 stroke, common rail, split and direct injection, 4 cylinders in line, turbocharged, with intercooler
Exhaust after-treatment	Diesel oxidation catalyst (DOC) and cooled EGR. (At the loads corresponding to the operating points studied, the electronic control unit does not activate the EGR valve, and EGR behavior was not obtained)
Compression ratio	16:1
Displacement (L)	2.8
Bore/Stroke (mm)	94/100
Maximum Power (kW @ rpm)	120 at 3600
Maximum Torque (Nm @ rpm)	360 at 1800

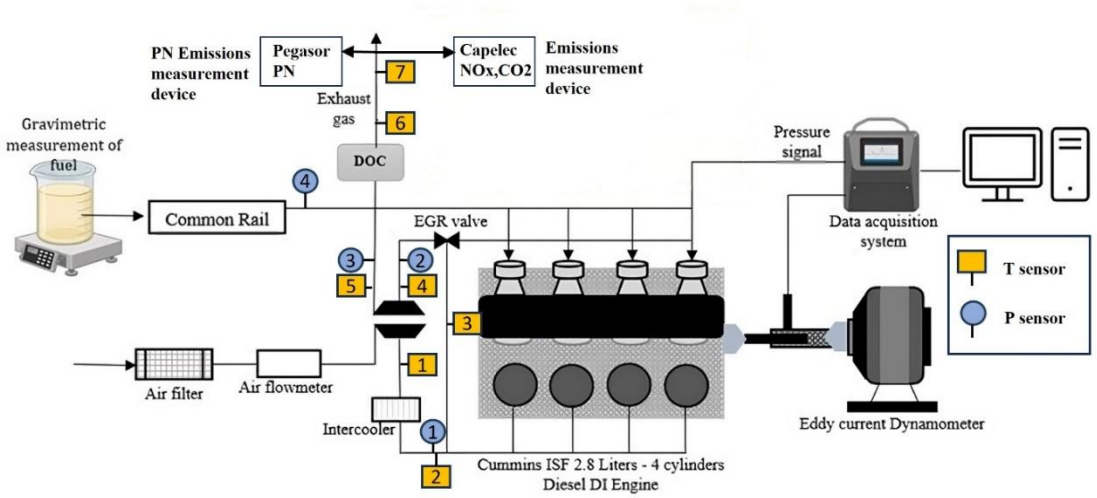

Figure 5. Schematic diagram of the diesel engine test bench.

Figure *5* illustrates the location of emissions measurements taken downstream of the Diesel Oxidation Catalyst (DOC). While this setup offers valuable insights into emissions behavior, it unfortunately precludes evaluation of the DOC's direct impact on emission reduction in this study. This limitation primarily arises from the absence of equipment specifically designed to measure hydrocarbon (HC) and carbon monoxide (CO) emissions, both of which are key targets for DOCs. However, it's important to note that DOCs designed for PM/HC/CO control also exert effects on several unregulated emissions, including aldehydes and polycyclic aromatic hydrocarbons (PAHs).

2.1.2 Calibration of measuring equipment

CAPELEC CAP 3010-4G gas analyzer

The CAPELEC CAP 3010-4G gas analyzer module is designed for technical control centers and engine tuning workshops. It measures CO, CO_2, NOx, hydrocarbons (HC) as propane equivalent, and oxygen emissions. Non-dispersive infrared (NDIR) is used to measure CO, CO_2 and HC; oxygen and NOx are measured using an electrochemical scavenger based on electrolysis. **Table *7*** shows the technical specifications [87], [88].

Table 7. CAPELEC CAP 3010-4G gas analyzer technical specification.

	Gas concentration range	Resolution	Accuracy
CO	0% vol to 15% vol.	0.01% vol if CO 3 digits = 0 0.01% vol if CO 3 digits = 1	0.03% vol or 3% (whichever is greater)
CO_2	0% vol to 20% vol.	0.1% vol.	0.04% vol or 4% (whichever is greater)
HC	0 ppm to 20000 ppm	1 ppm vol	10 ppm vol or 5% (whichever is greater)
O2	0% vol to 25% vol.	0.01% vol.	0.1% vol or 3% (whichever is greater)
NOx	0 ppm to 5000 ppm	1 ppm	-

Lambda (Air fuel ratio)	0 to 9.999	0.001	-
PEF	Real time value	0.001	-

Prior to the measurements, the equipment was checked by determining the CO, CO_2 and NOx concentrations from mixtures of known concentration. Specifically, samples from standard gas cylinders were diluted on-line with nitrogen; ***Figure 6*** and ***Figure 7***, and ***Table 8*** and ***Table 9*** show the results for NOx and CO-CO_2, respectively.

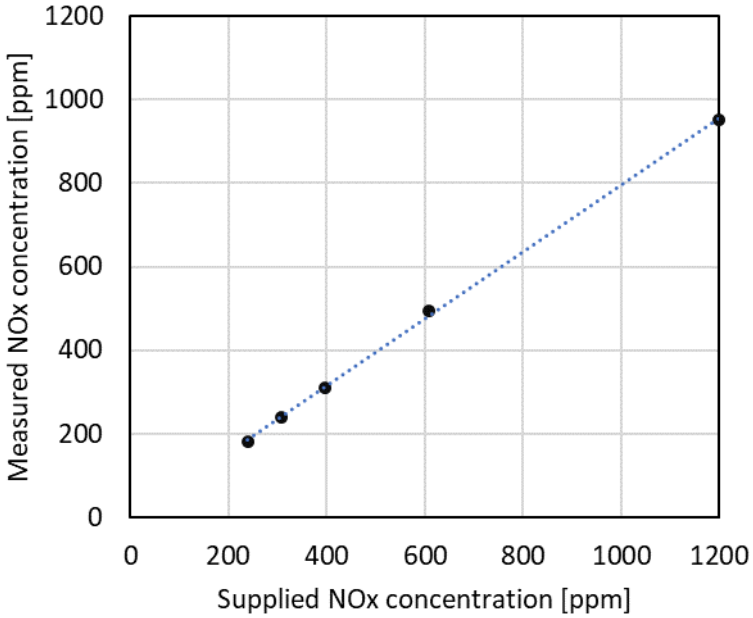

Figure 6. NOx verification.

Table 8. Error in NOx concentration.

Supplied NOx concentration [ppm]	Measured NOx concentration [ppm]	% Error
1200	952	20.67
607	495	18.45
397	310	21.91
307	238	22.45
239	182	23.85

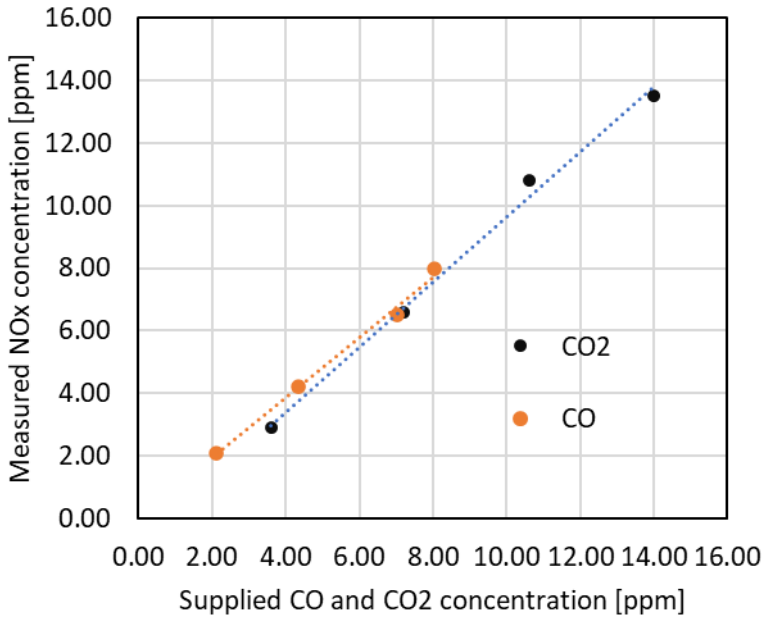

Figure 7. CO2 and CO verification.

Table 9. Error in CO2 and CO concentrations.

Supplied CO_2 concentration [ppm]	Supplied CO concentration [ppm]	Measured CO_2 concentration [ppm]	Measured CO concentration [ppm]	CO_2 % Error	CO % Error
14.00	8.04	13.5	8.00	3.57	0.50
10.60	7.04	10.8	6.50	-1.89	7.70
7.20	4.33	6.6	4.20	8.33	3.00
3.60	2.11	2.9	2.10	19.44	0.70

A moderate error in CO and CO_2 concentration, as well as a generally good linearity in the error percentage between the supplied and measured concentrations for all species was evidenced. However, NOx measurements presented a rather large error and, consequently, a calibration was carried out following a procedure standardized by the equipment supplier. After this, a 0.58% average error was obtained for NOx at 1200 ppm.

Pegasor PPS-M sensor

The Pegasor particle sensor is a continuous, real-time detector for particulate matter (PM). It quantifies the mass and number of particles from the exhaust gases. The particles are first charged by a corona discharge generated by a high-voltage power source, and then detected. The corona discharge causes the ionization of the particles, and an ion trap eliminates the free ions. The sensor provides information about the total surface area, mass, and total number of particles. [89] .

It was not possible to check the accuracy of the default calibration because the laboratory does not have alternative instruments capable of measuring particle mass and/or particle number concentration, which are necessary to make a comparison with the measurements, as suggested in [89]. However, a repeatability test, detailed in the following section, was conducted to assess instrument consistency.

Pressure, temperature, air flow, and fuel sensors were calibrated in previous studies. Details of these procedures can be found in [90], [91].

2.1.3 Repeatability

To ensure the repeatability of the test setup, fuel and air consumption, CO_2, NOx and PN emissions, as well as temperature and pressure, were monitored at several points in the intake and exhaust systems, at a single operating point of 2000 rpm and 50 Nm (2.52 bar BMEP), taken as the baseline operating point. At the beginning of each test, the engine was preconditioned for 15 minutes at idle speed (750 rpm and 0 Nm). A total of 12 tests were conducted over 4 days at different times. Commercial diesel was used in these tests, which contains 11 vol. % biodiesel from palm oil. The results are shown in Table 10.

Table 10. Results of repeatability tests.

Parameter	**Speed [rpm]**	**Torque [Nm]**	**Fuel consumption [mg/s]**	**Air consumption [g/s]**	**Percentage acceleration [%]**	**-**	**-**	**-**
Standard deviation	7.1	0.3	19.0	0.6	0.4			
Coefficient of Variation %	0.4	0.6	2.2	1.1	1.7			
Parameter	**TEMP 1 [°C]**	**TEMP 2 [°C]**	**TEMP 3 [°C]**	**TEMP 4 [°C]**	**TEMP 5 [°C]**	**TEMP 6 [°C]**	**TEMP 7 [°C]**	**TEMP 8 [°C]**
Standard deviation	2.8	0.7	0.5	1.8	1.3	1.5	1.6	4.1
Coefficient of Variation %	7.3	2.2	0.6	0.7	0.6	0.7	0.7	4.4
Parameter	**Rail press [bar]**	**Press 1 [mbar]**	**Press 2 [mbar]**	**Press 3 [mbar]**	**-**	**-**	**-**	**-**
Standard deviation	3.3	4.6	4.3	6.3				
Coefficient of Variation %	0.4	1.8	0.8	7.0				
Parameter	**CO_2 [%V]**	**O_2 [%V]**	**NOx [ppm]**	**MP [mg/m³]**	**N [x 1e3/cm³]**			
Standard deviation	0.1	0.2	25.4	0.4	1671.2			
Coefficient of Variation %	3.0	1.1	3.2	21.2	21.2			

Most variables exhibit good repeatability, with a coefficient of variation (CV) not exceeding 2.2% for speed, torque, percentage of acceleration, and fuel and air consumption. On the other hand, temperature and pressure show a maximum standard deviation of 4.1°C and 6.3 mbar, with CVs

of 7.3% and 7%, respectively. Regarding emissions, CO_2 and NOx show CVs below 3.2%. However, CV for particle number is larger than 20%. Therefore, additional tests were conducted to establish a conditioning process aimed at obtaining better repeatability for PN.

Repeatability tests for PN measurement

To ensure that the PN steady state was reached, the engine was first operated at baseline speed and load conditions for 30 minutes. As shown in ***Figure 8***, steady state was achieved after approximately 15 minutes (900 s). Therefore, this duration was adopted as the time between each test to guarantee PN steady state. This time interval between each test is also recommended in [89], along with two additional recommendations that were implemented in this work:

1. Monitor the temperature in the exhaust duct to prevent condensation and thermophoresis.
2. Verify that all system variables are within the standard deviation limits, including emission measurements.

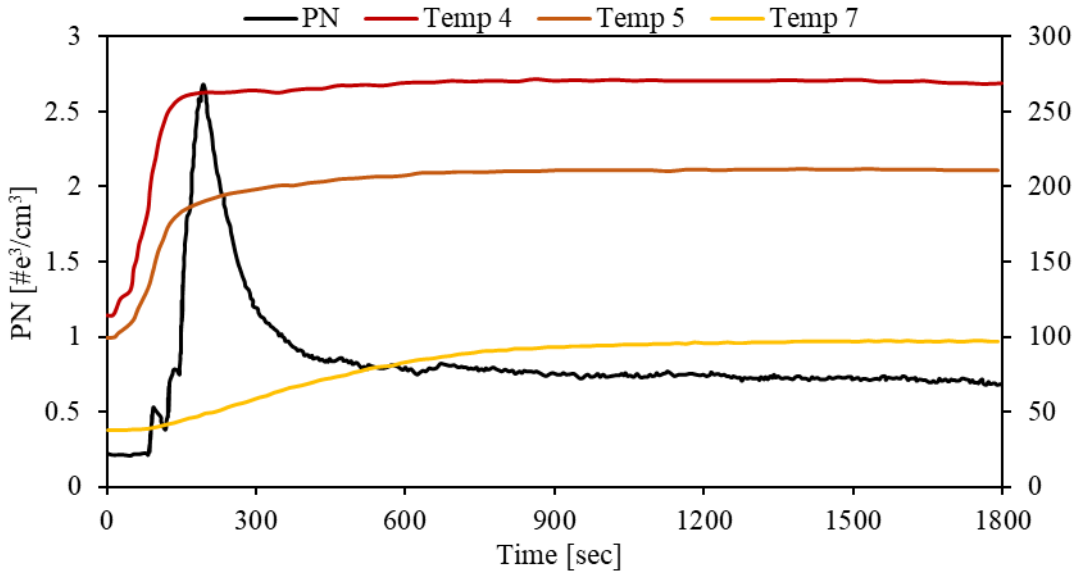

Figure 8. Steady state PN measurements.

As proposed by [92], one of the main contributions to experimental variations lies in engine preconditioning but there is no consensus on the optimum engine operating state for conducting this procedure. The Particle Measurement Program (PMP) [93] indicates that preconditioning does not noticeably impact particulate matter (PM) but has an important effect on PN levels. In the context of preconditioning a diesel engine, running it at higher load points resulted in elevated PN emissions during subsequent tests, which may be attributed to heightened inertial deposition under higher load conditions. However, [94] demonstrated that alternating periods of idle operation with higher power operation led to increased PN emissions.

Considering these findings and the low repeatability obtained in the previous tests, it was decided to evaluate two alternating periods between idle speed and the baseline operating point (2000 rpm, 50 Nm), which corresponds to 14% of the maximum load. At the beginning of each test, all the recommendations suggested in the Pegasor manual were implemented. ***Figure 9*** summarizes the procedure that was followed.

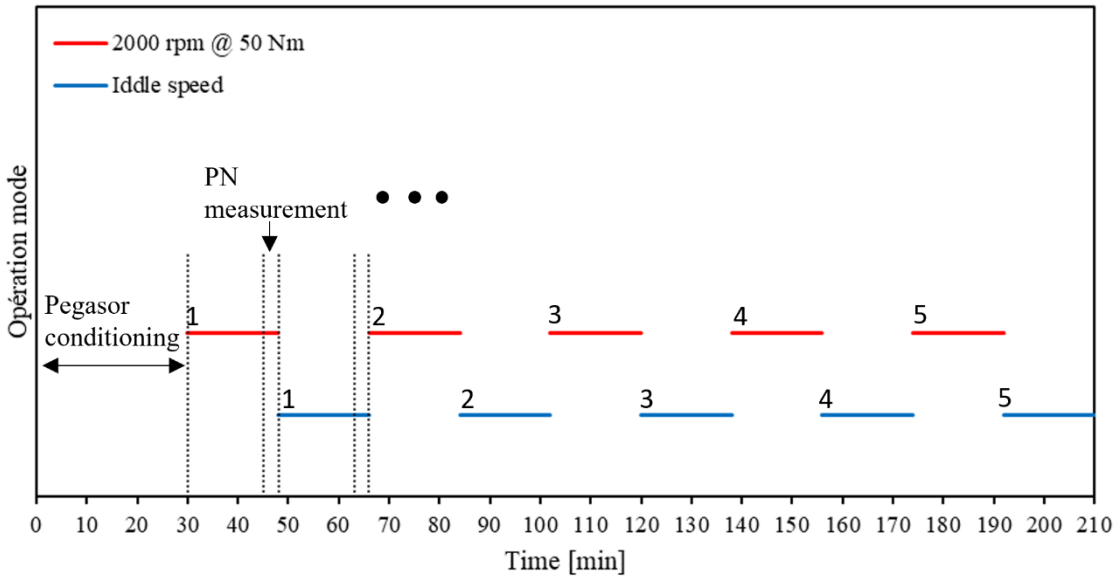

Figure 9. PN measurement procedure.

The results in ***Figure 10*** indicate an approximate 6% reduction in PN during the first two stages of the baseline operating point. However, from the third stage onwards the levels tend to stabilize with an initial increase of 0.5% followed by a subsequent decrease of 0.7%. Similar results were obtained during the second day of testing, leading to the conclusion that proper preconditioning should include two alternating stages between idle and the baseline operating point. The resulting standard deviation (357.83 x 1e3/cm³) is 76% lower than the initial repeatability tests, with a coefficient of variation of 2.56%. This indicates a noticeable improvement in the repeatability of particle number measurements.

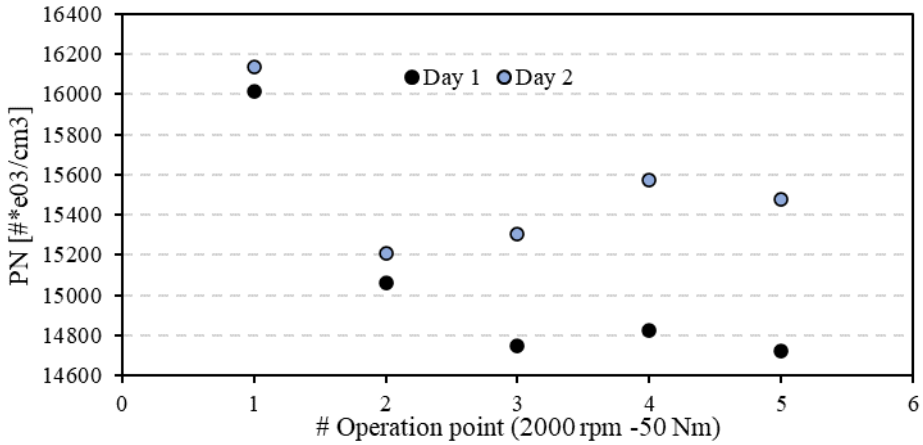

Figure 10. PN measurement results.

2.1.4 Engine maps (emissions and performance)

Emissions, engine combustion parameters, pressure, temperature, and fuel and air consumption were measured at 24 steady-state operating points for B20 (**Figure *11***), and 16 points for ULSD (**Figure *12***). These points were chosen within the speed and load range corresponding to the driving cycles used in this study. The selection was made based on a longitudinal dynamic

analysis, aiming to capture the most representative operating conditions. Additionally, the choice of these points took into consideration test bench limitations, such as the maximum torque regulated by the dynamometer. Due to the limited experimental availability of HVO20, this blend was not included in the experimental tests.

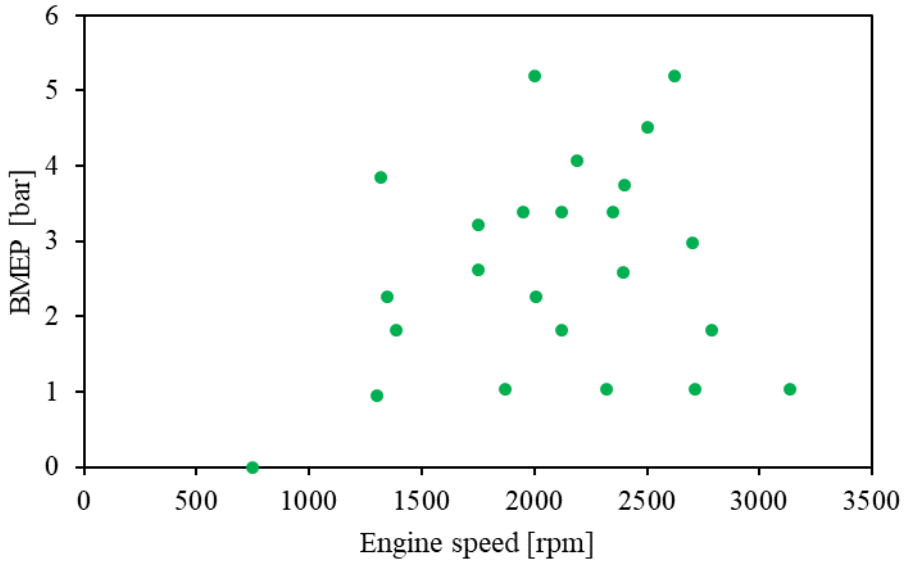

Figure 11. Operation points measured for B20.

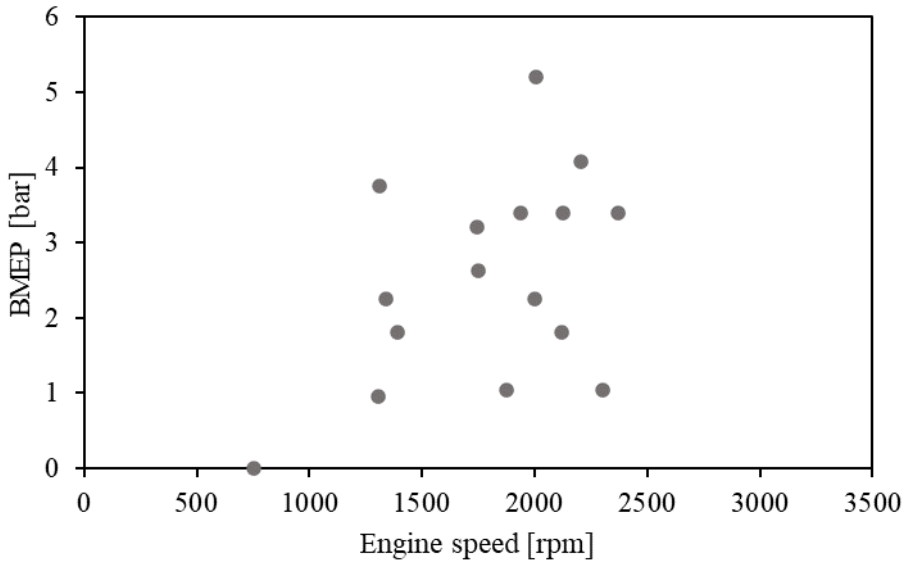

Figure 12. Operation points measured for ULSD.

The difference in the number of points between the two fuels is related to the availability of each fuel. In fact, diesel is commercialized in Colombia as 10 vol. % biodiesel blends, and pure ULSD can only be procured directly from ECOPETROL with many restrictions. In addition, some technical difficulties hindered the collection of data for the last operating points for ULSD.

Data processing of pressure curves was conducted using CARIBE, a thermodynamic diagnosis model developed by the University of Antioquia's GIMEL research group. CARIBE utilizes cylinder pressure data to determine heat release rate and perform exergetic analysis in

compression ignition engines. The analysis workflow involved loading average data and pressure curves, followed by signal treatment (filtering and averaging 100 cycles), referencing, and finally, determining the thermodynamic loss angle for accurate pressure-volume coupling [95].

. The remaining measured parameters were processed using Excel. Each parameter's value was determined by calculating the mean of the data set collected over a 3-minute period.

2.2 Modeling

2.2.1. Engine model

2.2.1.1. Engine sub-blocks

The engine modeling process employs pre-built blocks from the GT Libraries, which represent various engine parts, such as the EngCylinder and EngineCrankTrain, and connection objects, such as the Valve*Conn. These blocks define engine geometry and characteristics using reference objects for more detailed aspects (e.g., combustion and heat transfer). Virtual links interconnect these components, facilitating information exchange. The approach employs a one-dimensional model to simulate flow and heat transfer within engine components. The solver determines engine performance by calculating brake torque for a given speed (speed mode) or solving engine speed for an imposed load (load mode). The chosen mode is specified in the EngineCrankTrain object. In this work, Speed Mode, which is widely applied, is used. This mode allows users to set a constant or reference-dependent speed, and yields quick steady-state results, avoiding the time needed for crankshaft speed stabilization in loaded engines.

A list of the information needed to build an engine model is included below. When the required information was not experimentally accessible, different sources were consulted and, if not available, some parameters were estimated. **Table *11*** summarizes the data for the Cummins ISF 2.8 and indicates the alternatives employed to address the lack of certain information.

Table 11. Data required to build the engine model.

Parameter	Value	Source
CR	17.5:1	[95]
Firing order	1-3-4-2	[96]
Configuration (Line or V)	Line	[96]
Stokes	4	[96]
Bore (mm)	94	[96]
Stroke (mm)	100	[96]
Connecting rod length (mm)	157.5	[95]
Piston TDC clearance height (mm)	3.38	Estimated
Piston inner diameter (mm)	94	This work
Piston and cylinder area ratio	1.36	Estimated
Location	Cylinder center	-
# injectors	4	-
# nozzle holes	7	[97]
Hole diameter (µm)	117	[97]

Injection profile	Depends on operating condition	Provided by [98]
Fuel type*	ULSD, B20, HVO20	-
Valve diameter (mm)	32.66	[95]
Discharge coefficients (CD) out	0.118361	[95]
Lift profile	-	GT model example
Valve diameter (mm)	29	[95]
Discharge coefficients (CD) out	0.133687	[95]
Lift profile	-	GT model example
Efficiency map	-	Estimated from measured data
Efficiency map	-	GT model example

A hyphen (-) in the "Source" column denotes a parameter lacking a reference. Similarly, in the "Value" column, it signifies the absence of a single value, indicating the use of an entire data set.

The most relevant considerations for the engine model are described below:

- No significant reaction takes place in the exhaust system.
- The ControllerDInject object was used to target the engine load (BMEP) operation by adjusting the injected fuel quantity of the main injection.
- Input parameters such as rail pressure, acceleration percentage, and injection times were parameterized as a function of load and engine speed.
- Pilot injection mass were considered from 1 to 2.3 mg/cycle, according to measured data consistency checks.

2.2.1.2. Combustion model

The selection of a combustion model depends on the required outcome. There are predictive, non-predictive, or semi-predictive models. In the predictive models, unlike the non-predictive models which predefine the combustion rates as input data, they are calculated during simulation based on in-cylinder conditions, allowing for the assessment of the impact of different variables on the final burn rate. However, predictive simulations are more computationally costly than non-predictive methods.

Two predictive combustion models were employed in this study to ensure accurate emission and performance results. These models are described below.

Direct-Injection Diesel Multi-Pulse Model ('EngCylCombDIPulse')

This model predicts combustion rates and associated emissions in direct-injection diesel engines with single or multi-pulse injection events. The DI Pulse model tracks fuel injection, evaporation, mixing with surrounding gas, and combustion. Accurate injection profiles are crucial for meaningful results.

The cylinder contents are divided into three thermodynamic zones, each with distinct temperature and composition:

- The main unburned zone, which contains the cylinder mass at intake valve closure (IVC).

- The spray unburned zone, which contains injected fuel and entrained gas.
- The spray burned zone, which houses combustion products.

Calibration of the DI Pulse model is necessary to match the combustion parameters obtained from cylinder pressure analysis, such as heat release rate. Specifically, the model incorporates multiple submodels to simulate pertinent physical processes during injection and combustion, and some of their attributes can be adjusted in the calibration:

- Fuel Injection.
- Entrainment.
- Evaporation.
- Ignition.
- Premixed Combustion.
- Diffusion Combustion.

More details of these parameters can be found in Appendix 1.

The emissions predicted with this model are limited: CO, CO_2 and unburned hydrocarbons (HC) are calculated with a chemical equilibrium model. NOx and particulate matter mass (PM) are predicted using more detailed models like the extended Zeldovich mechanism and the Hiroyasu-Kodota model, respectively.

However, the model currently lacks the capability to directly predict particle number (PN). Fortunately, some studies have observed a reasonable correlation between PM and PN for larger particles (PM > 10 μm) across different engine technologies [99], [100]. Therefore, for this study, PN was estimated by combining the PM results from the Hiroyasu-Kodota model with the PN/PM ratio obtained from dedicated measurement equipment used in the experimental phase. While this approach provides a valuable estimation, it's important to acknowledge its limitations, as the direct relationship between PM and PN may not hold true for all particle sizes and engine conditions.

Direct-Injection Stochastic Reactor Model ('EngCylCombDISRM')

This combustion model predicts the combustion rate and associated emissions for direct injection. The zero-dimensional stochastic reactor model (0D-SRM) concept is based on the transported probability density function (tPDF) method. In the 0D-SRM model, the in-cylinder mass (including injected spray mass and intake flow mass) is divided among hundreds of particles of different composition and temperature, such that in-cylinder thermal and composition stratification can be captured more accurately, which in turn helps to improve emissions predictions.

The model employs detailed chemistry in hundreds of particles to simulate in-cylinder combustion process. Therefore, the required computational time and resources are expected to be higher than in other models. Accurate injection profiles and timing are fundamental for the burn rate prediction, and the model has tunable parameters for calibration using measured data.

The model divides the cylinder content into particles at the cycle start. New particles are introduced during spray injection and intake flow based on profiles. Two GT-Suite implementations ("VCF" and "Flow") account for turbulence effects differently: "VCF" uses mass, velocity, composition, and turbulent frequency, while "Flow" uses mass and composition. Particle properties evolve as per in-cylinder processes. Average cylinder properties are calculated

through mass-weighted averages of particles. Particle mass changes only via exhaust and particle number control. In this work, the "VCF" approach was selected based on superior performance recommended by GT.

The particles interact among themselves using a mixing model. The mixing process determines how fast spray particles will entrain into the air and vice-versa. Two mixing models are implemented: the Euclidean Minimum Spanning Tree (EMST), and the Interaction by Exchange with the Mean (IEM). EMST is, in general, physically more accurate and computationally more expensive than IEM. Several attributes can be used for calibration, some of them being accessible only based on the selected turbulence model. For this study, EMST model was adopted and optimized its performance by calibrating four key parameters:

- Scalar Mixing Multiplier.
- Frequency Decay Constant.
- Minimum Frequency Decay Rate.
- Cutoff Frequency Multiplier.

More details of these parameters can be found in Appendix 1.

2.2.2. Engine model calibration and validation

Direct-Injection Diesel Multi-Pulse Combustion Model (DIPulse)

This section outlines the methodology used to calibrate the DIPulse model (**Figure *13***). The initial step was to analyze the data collected in the experimental stage. Since intake and exhaust pressure traces were not directly measured, the Cylinder Only Pressure Analysis (CPOA) method was chosen as the optimal approach for analysis.

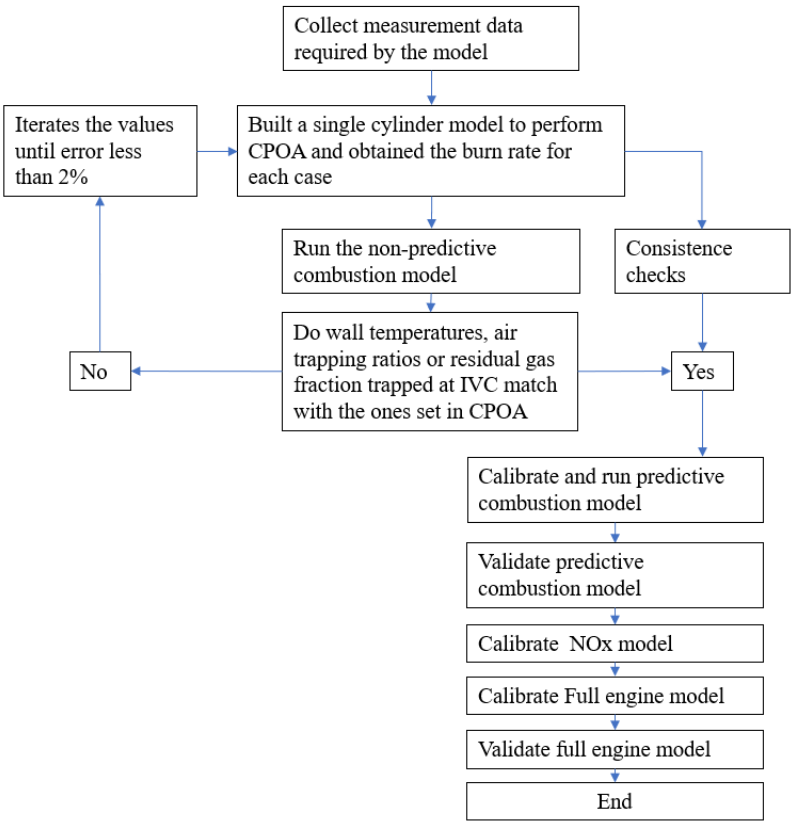

Figure 13. Methodology followed for engine calibration and validation.

Then, a single-cylinder model was created in GT-Power to facilitate the CPOA based on the input data. This model only includes the EngCylinder and EngineCrankTrain and an injector for DI diesel (**Figure *14***). The model runs 2 cycles, essentially repeating the first cycle twice to properly converge on results: thus, valves, ports, and other parts of the engine are not necessary. The simulation methodology followed by this model is [70]:

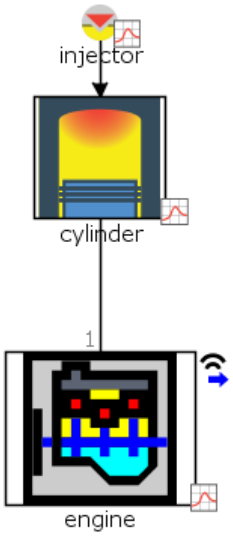

Figure 14. Single cylinder model CPOA.

1. At the beginning of a cycle, a rough calculation of combustion burn rate is done making some assumptions about heat transfer (e.g., Woschni).
2. The resulting burn rate is applied during the forward simulation cycle and the true heat transfer rate is stored.
3. A final burn rate calculation is done with the true heat transfer from the simulation and all results stored.
4. The final burn rate is applied during the forward simulation cycle to provide a comparison of measurement versus simulation.

The input data required are:

- Cylinder Pressure Profile.
- Injection Profile (necessary for DIPulse calibration).
- Volumetric Efficiency.
- Trapping Ratio.
- Residuals Fraction.
- Start of Combustion (injection).
- Wall temperature.

Due to the absence of experimental values of variables such as wall temperature, air trapping ratio and residual gas fraction trapped at IVC (intake valve closure), an iterative process was employed to determine suitable values by using a non-predictive combustion model (**Figure *15***) that allows the imposition of a burn rate profile directly as a function of crank angle, calculated from the

cylinder pressure in the CPAO (Constant Pressure Analysis of an Orifice). The initial values recommended for GT were utilized for unknown quantities.

Furthermore, the model should include additional components such as valves, intake, and exhaust runners. Another template may be used to predict the structural temperatures, such as surface temperatures, which are used in the calculation of in-cylinder heat transfer. Intake and exhaust conditions were imposed using the measured data.

Finally, the accuracy of the measured cylinder pressure was validated through an automated consistency check applied to the input data, which is briefly described below.

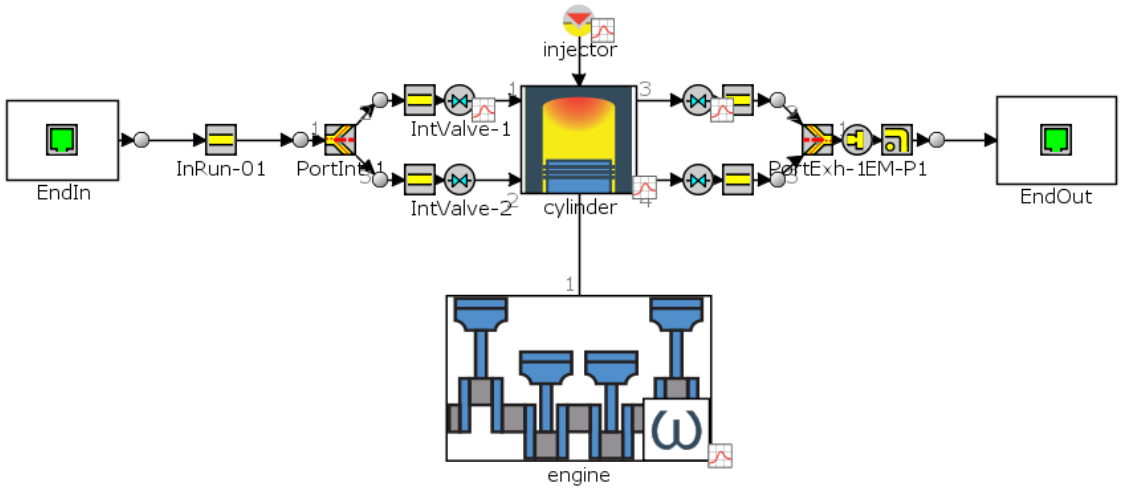

Figure 15. Non predictive model.

Implicit errors in the calculation of burn rate from cylinder pressure stem from the accuracy in pressure measurement, input values, modeling assumptions, and simplifications. These errors, which lead to a "cumulative error", are dealt with by GT-Power by adjusting fuel energy content (LHV) using a multiplier based on combustion efficiency or burned fuel fraction from test data. The LHV multiplier reflects the cumulative error level but does not pinpoint its source. Even when the multiplier is close to 1.0, verifying input data quality is recommended. Specifically, there are several consistency checks that are performed automatically and reported in the Pressure Analysis result tables as part of the pressure analysis calculations; these automatic checks are labeled "Error #". Most result quantities referenced below can be found in the Cylinder Pressure Analysis result tables or as a cylinder RLT [70].

- Reasonable IMEP.
- Cumulative Burn During Compression.
- Compression Slope.
- Fraction of Fuel Injected Late.
- Large LHV change required.
- Combustion efficiency or burned fuel fraction comparison to target.

A detailed description of these errors can be found in Appendix 1.

After the successful consistency checks, the predictive combustion model was integrated into the single-cylinder model. 21 and 13 operating points for B20 and ULSD, respectively, were selected across the engine map. The Optimization tool provided by Gamma Technology was utilized to determine the final set of multipliers that offered the best possible match. This best match may be

defined in terms of measured and predicted burn rate, cylinder pressure, IMEP, emissions, etc. GT recommends determining a singular set of values for the four primary DIPulse attributes that result in the lowest value of the EngCylinder RLT "Improved Burn Rate RMS Error (measured vs predicted)", averaged across all cases. The Improved Burn Rate Root Mean Square Error (RMS Error) is the error between both the predictive and measured combustion burn rate over time, during the 0.1% and 90% burn angle and is also weighted by the LHV multiplier of the predictive analysis. This value describes the quality of fit between the predicted and the measured burn rate curve, thus simplifying the automated optimization of the predictive combustion model. A big value represents a high deviation between the two curves.

This selection leads to the optimal alignment between measured and predicted burn rates. The optimization process adhered to recommended limits, as specified in **Table *12*** [70]:

Table 12. DI-Pulse multipliers range.

Parameter	Minimum	Maximum
Entrainment Rate Multiplier	0.95	2.80
Ignition Delay Multiplier	0.30	1.70
Premixed Combustion Rate Multiplier	0.05	2.50
Diffusion Combustion Rate Multiplier	0.40	1.40

Two approaches were employed for selecting the multipliers: 1) Single-set or sweep optimization including 13 and 21 operating points for ULSD and B20 respectively; and 2) Independent optimization for ULSD and B20 with 13 and 21 operation points, respectively.

After completing the calibration of the combustion model, a validation process was conducted by comparing the measured data with the simulated results. These parameters, directly associated with the combustion process, are: BMEP, IMEP, CA50, Cylinder peak pressure, and CO_2 and NOx emissions.

After the calibration of the combustion burn rate multipliers, NOx emissions calibration was done. The formation of NOx has been modeled using extended Zeldovich mechanism. Gamma Technologies suggested to calibrate the two most influential parameters (see **Table *13***) defined in the NOx emission template for DIPulse model, the objective of this optimization being to minimize the error between the predicted and measured NOx concentration.

Table 13. Recommended NOx calibration limits.

Attribute	Minimum	Maximum
NOx calibration multiplier	0.10	2.00
N_2 oxidation activation energy multiplier	0.30	1.10

The last step involves calibrating the full engine model (***Figure 16***) using the CPOA results. Building upon the successful single-cylinder model calibration, the same combustion parameters were directly transferred to the complete engine model. However, ensuring realistic operating conditions necessitated further calibration of the intake and exhaust systems to match the desired inlet and outlet conditions at the cylinder.

Due to the simplified geometry of the full engine model compared to the real engine, specific adjustments were required. These adjustments involved modifying the diameters and applying multipliers to heat transfer and pressure drop coefficients related to friction. These modifications aimed to compensate for the simplified geometry and achieve a more accurate representation of the actual engine's behavior.

This process was conducted with the guidance and recommendations from the technical support team of Gamma Technologies. Throughout this procedure, it is essential to compare the calculated and the measured engine parameters, such as, BMEP, IMEP, FMEP, CA50, Cylinder peak pressure, Air, and fuel flow, BSFC, Volumetric efficiency, Intake and exhaust manifold temperature and pressure (time averaged), Cylinder pressure and combustion rate, and CO_2 and NOx emissions.

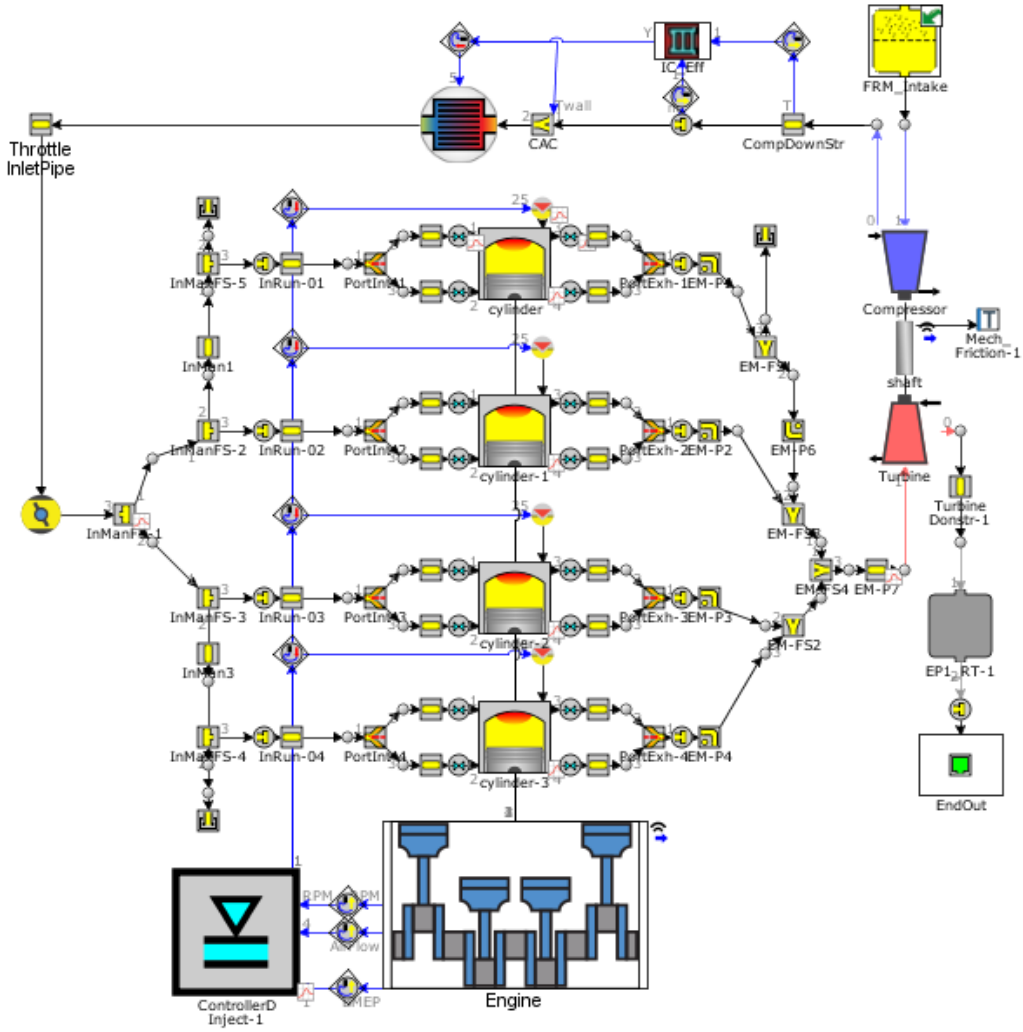

Figure 16. Full engine model.

The approach to calibrate the engine involves the steps depicted below (**Figure *17***), that apply to any model calibration exercise [72].

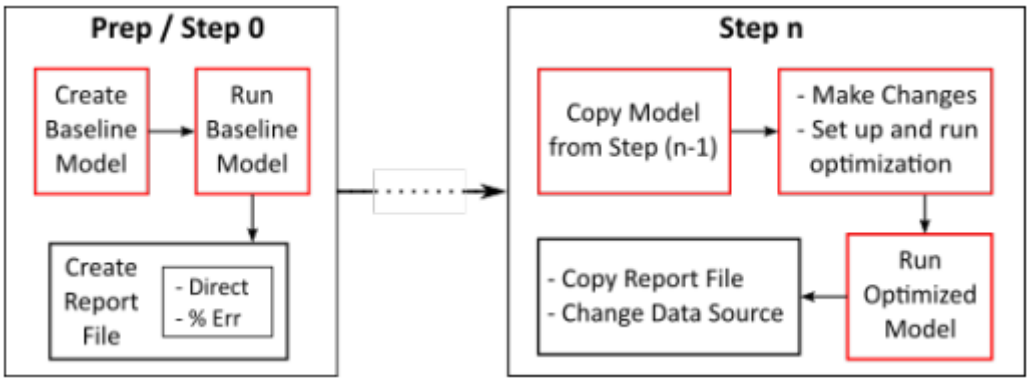

Figure 17. General approach to calibrate an engine model.

A combustion engine is a multivariable system. Choosing to adjust one input data may change the prediction in a desirable way, but if wrong input is chosen an additional error will be introduced that most likely will leads to increased problems at other operating conditions. The source of the discrepancy between the predicted and measured data can be isolated and the problem can be addressed if these steps are followed [70]:

1. Match the intake manifold pressure. This calibrates flow loss between the inlet and the measurement location. This should be done at the highest engine speed only (calibrate within 2%) and comparing over the entire range of speeds.

2. Calibrate the VE at the highest speed to calibrate only pressure losses (match within 5%) and calibrate at all engine speeds.

3. Calibrate Back Pressure only at the highest speed.

4. Match the cylinder pressure: pressure profile during compression, pressure profile during combustion, and pressure during expansion using the heat transfer convection multiplier.

5. Match the exhaust temperatures: heat transfer input in exhaust ports, wall temperature solver in exhaust.

6. Calibrate the FMEP.

To ensure accurate results and validate the model, an evaluation based on linear regression was performed. This involved placing the measured values on the *y*-axis and the predicted values on the *x*-axis; the coefficient of determination, r^2, was the statistic utilized; additionally, RMSD provided valuable insights into model evaluation [101]. This analysis also incorporated all the operational points that were excluded from the calibration process. Targets for model accuracy for different parameters are shown in **Table *14***, based on GT recommendations and other studies [70], [102], [103].

Table 14. Model accuracy targets.

Parameter	Targets
IMEP	5%
CA50	+-2 CAD
Peak Cylinder Pressure	5%
Air flow Rate	5%
Fuel consumption mg/cycle	5%
NOx concentration	20%
CO_2 concentration	10%

The final model was used to generate a map of emissions and performance parameters required by the vehicle model. The operating points (Figure 17) were determined following some GT recommendations, such as [104]:

- The engine Mechanical Output map should extend from a minimum speed at (or preferably 20% below) idle speed to a maximum speed at "redline" speed or slightly higher.
- For all quantities, maps should include {speed, load, Q} data points at 1) the maximum BMEP, and 2) zero BMEP, and at both the minimum and maximum speeds.
- Points should be reasonably well distributed within the domain determined by these guidelines.

In this study, a calibration process for the HVO20 blend could not be performed due to lack of experimental data. As a result, the constants derived from the ULSD and B20 were utilized to simulate this blend and generate a complete engine map, taking into consideration their corresponding properties for the fuel object.

Direct-Injection Diesel Stochastic Reactor Model

Due to the higher computational time cost associated with reaction chemistry, it was not possible to implement a methodology similar to that of the DIPulse model, since the optimization would take too much time with the available computational resources (more than a week per case study). Therefore, certain assumptions were made. Initially, the kinetic mechanism and the most suitable surrogate for ULSD and B20 fuels were determined. This was based on the results of several tests described below.

As discussed in Chapter 1, no mechanisms for diesel+biodiesel blends surrogates that have been validated under engine conditions are available. Furthermore, it is desired that these surrogates allow for the estimation of a wide range of regulated and unregulated emissions, but some of these species are present in the reactions of the ULSD mechanism and not in the biodiesel mechanism, and vice versa. Therefore, it was necessary to generate a combined mechanism that could simulate all the relevant fuels, including HVO. For this purpose, the Mechanism Merge tool of Chemkin® was used, which provides a robust and accurate method to combine mechanisms from similar or different sources, as well as direct comparison of data provided by different sources for thermodynamic and transport properties of species, along with reaction rate data.

Before proceeding with mechanism merging, preliminary tests were conducted to preselect the mechanisms. Specifically, mechanisms that allowed for simulation without encountering errors or warnings, and which also provided results considered reasonable were selected. The surrogates

proposed by the authors of the ULSD and B100 mechanisms, summarized in Tables 3 and 4, were employed. Furthermore, due to the lack of some experimental data for B100, B20 data was used as basis. The methodology employed was:

1. A simplified, single-cylinder CPOA analysis allowed to verify data consistency when using different mechanisms and surrogates as fuel. Trapped mass conditions were determined following the same methodology described earlier.
2. Subsequently, the predictive combustion model was integrated into the single-cylinder model (DISRM), and the Measured + Predicted (M+P) Analysis mode compared the predicted results with experimental data obtained at the base operating point (2000 rpm and 50 Nm). A single set of calibration constants was used in all the cases.

Following the pre-selection process, mechanism merging was carried out and evaluated following the same methodology. Additionally, some compositions were proposed for the selected surrogates according to the properties of fuels used in this study (***Table 2***). Based on the results obtained from consistency checks, combustion model predictions, ignition timing, and simulation time, the most suitable mechanism and surrogate for ULSD and B20 were determined.

A thorough optimization of the calibration constants was not performed. Instead, a manual adjustment was conducted to reduce the error in the compared combustion and emissions parameters. A set of constants was derived for both ULSD and B20 fuels.

High computational demands precluded the development of a complete 4-cylinder model with DISRM combustion model. Running a single test simulation at an operating point with this model took over a day, and emission maps required around 90 points per fuel. To overcome these limitations, emissions maps were constructed using a single-cylinder model. As mentioned earlier, this model requires specific input parameters, which were obtained from simulations of the full engine model with DI-Pulse. This integrated approach enabled the capture of the essential features of combustion with chemical kinetics while remaining computationally feasible and allowed to observe unregulated emissions as well.

2.2.3. Vehicle model

A vehicle model was developed in GT-Suite (**Figure *18***) to simulate several driving cycles, enabling the determination of emission factors, fuel consumption and performance parameters. The vehicle under investigation is a light-duty vehicle Foton Tunlad, equipped with a 2.8-liter Cummins engine. The vehicle modeling process requires detailed information for all relevant components, e.g., friction force, dynamic ratio of wheels, equivalent mass of the vehicle, gear ratio from the gearbox, final drive ratio (**Table *15***).

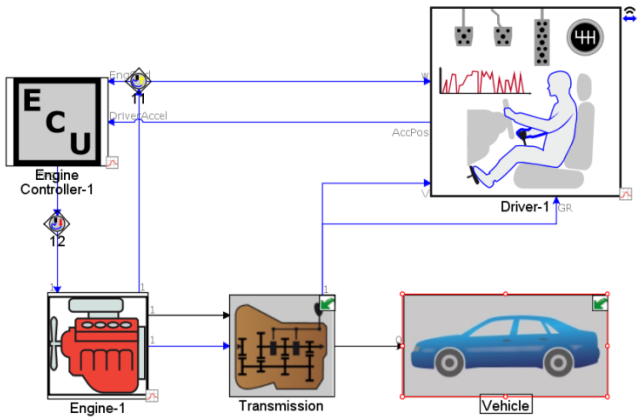

Figure 18. A schematic of the vehicle simulation model in GT-Suite.

Table 15. Parameters of the simulated vehicle.

Friction force coefficients [$Fr=A+BV+CV^2$]	A=217 N B= 0 N.h/km C=0.0576 N.h^2/km^2
Wheelbase [m]	3.1
Gear Ratios	1st----4.016 2nd----2.318 3rd----1.401 4th----1 5th----0.778
Final drive ratio	3.91

Vehicle was simulated under a dynamic approach. In this mode, the engine, driveline, and vehicle states react to mechanical power inputs from sources such as engines or electric motors, and power losses to factors such as aerodynamics, rolling resistance, brakes, component friction and generators. The control of power supply from the engine rests with the user or driver. However, the states of the driveline are not directly controlled. Instead, the resulting acceleration and speed depend on the supplied power, vehicle and driveline properties, and cannot be predetermined. However, controllers can be utilized to follow a specific speed schedule. This mode closely replicates the real-world behavior of a vehicle and driveline, influenced by controlled inputs from the driver, engine, and powertrain control systems.

The other relevant assumption is the engine Map-based model, which is defined using primary and secondary maps. The primary maps include Mechanical Output and Engine Friction maps, representing brake torque and friction torque based on rpm and accelerator position. However, well-defined accelerator position limits are necessary. Secondary maps, on the other hand, such as fuel consumption and emission maps, are based on rpm and load. Because gaps are often present in engine map data, GT-Suite allows for using scattered Q (rpm, BMEP) data and interpolates the intermediate points, even considering load normalization.

The essential templates for the modeling are listed below (detailed description can be found in Appendix 1).

- EngineMap - Advanced Map-Based Engine Model.

- Lumped 1D Discrete Ratio Transmission Model.
- ICEController – Map - Based Internal Combustion Engine Simple Controller for Idle and Fuel Cut (Compound).
- VehDriverAdvanced – Advanced Driver for Open and Closed Loop Maneuvers.
- VehicleBody – Vehicle Representation for Longitudinal Vehicle Dynamics.

The three driving cycles described in section 1.3.11 were simulated. A gear-shifting strategy based on the Brazilian standard NBR 6601 was used to follow the cycles [105]. The shift was determined by the imposed-speed thresholds shown in **Table *16***.

Table 16. Speed thresholds for the gear-shifting strategies.

Gear shifting	NBR 6601 Strategy
1st – 2nd	25 km/h
2nd – 3rd	40 km/h
3rd – 4th	65 km/h
4th – 5th	72 km/h

The validation data for the vehicle model comes from chassis dynamometer tests of a Euro IV Foton FHR vehicle equipped with a Cummins ISF 2.8 engine and a DOC aftertreatment system. It's important to note that these experimental tests were not conducted as part of this research project, but rather obtained from a different study case.

Despite this, the data remains suitable for validation due to several reasons:

- Shared Engine Model: Both vehicles utilize the same core component - the Cummins ISF 2.8 engine. This engine dictates power generation and emissions. Since engine behavior significantly impacts vehicle performance and emissions, data from the identical engine provides valuable validation insights.
- Similar Aftertreatment System: Both vehicles share the DOC aftertreatment system, crucial for reducing emissions.
- Representative Vehicle Class: While not identical, the Foton FHR belongs to a similar vehicle class. This suggests similar driving patterns and operating conditions, making the test data relevant for validating overall vehicle model performance.
- Limited Availability: Obtaining data from the exact simulated model might have been impractical due to limited availability or access, a common development challenge. Utilizing data from a readily available, representative vehicle with the same core components allows for validation progress and model refinement based on the gained insights.

By considering these factors, utilizing the external experimental data offers a reasonable approach for initial validation of the vehicle model. Future validation efforts should aim to obtain validation data from a vehicle model closer in design to the one being simulated. This will further enhance model accuracy and reliability.

Tests were carried out following WLTC cycle for Class 1 vehicles, applicable to the vehicle category with a power-to-mass (PMR) ratio ≤ 22. Before the test, one cycle was carried out for the preconditioning of the engine and aftertreatment system.

The chassis dynamometer (MD-150 Mustang) consists of a double roller with a diameter of 218 mm (8.575 in) and 149.14 kW nominal power, which simulates the rolling and aerodynamic resistances. The engine control strategy was not modified from the commercial one of the Foton vehicle. The air-fuel ratio and the inlet air mass flowrate were measured with Mexa 730 HORIBA

and MAF Toyota sensors, and fuel consumption was calculated from both. Particle mass and number, NOx and CO_2 were measured at the tailpipe downstream of the DOC with a ParSYNC® PLUS analyzer from 3DATX.

Chapter 3. Results and Analysis

3.1 Calibration of the Predictive Combustion Models (DI-pulse)

Figure *19* shows the results of consistency checks after the iterative process described in Chapter 2. Adjustments were required in the compression ratio, varying from 17.5 to 16, based on recommendations from GT support. Although the geometric compression ratio of an engine is constant for each condition, its value can change with load and speed due to tolerances that affect the engine components. In particular, the cumulative burn during compression was the most frequent error at the beginning, which is the error flagged with a wrong compression ratio. Injection timings for both pre and main injection were also adjusted, using the measured energization signal in the injector as reference with a set value of 400 µs for the injection delay. Since the fuel mass injected for the individual pre and main injections could not be measured, an iterative process was performed using the total injected mass, with initial values for pre and main injections at different energization times and rail pressures taken from the results of [98].

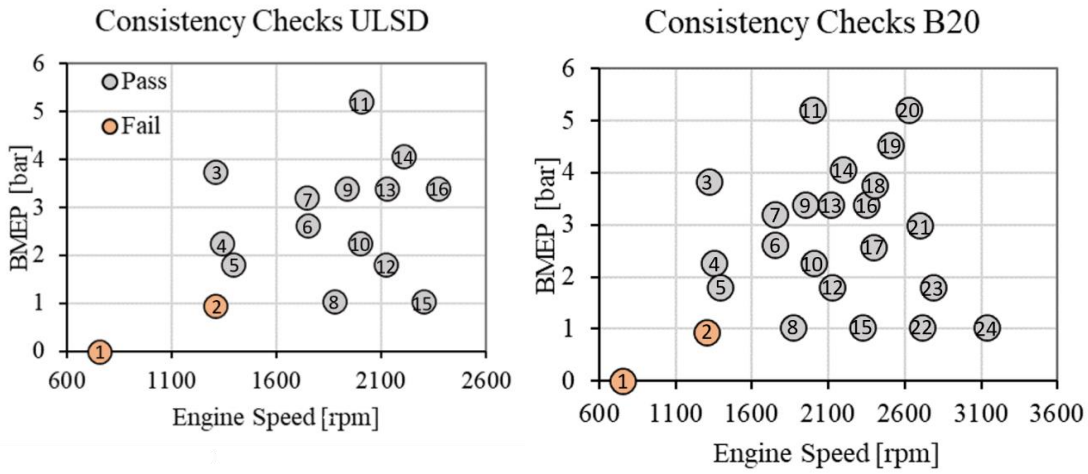

Figure 19. Results of consistency checks.

Both fuels passed the consistency checks in most operating conditions but failed at the same points: idle, and 1300 rpm and 0.95 bar. The errors found at these conditions, namely, the cumulative burn during compression and the need for a large LHV change multiplier, may be due to the instability of engine operation at low torques and speeds [103]. However, the errors were close to the thresholds used in every check by GT POWER, and both conditions were integrated in the calibration process to include the low speed and low load region. These results helped to verify the quality of the data, and therefore ensure a successful calibration process. Below are the results of the calibrated model.

Figure *20*-24 display the errors obtained for combustion parameters using the optimized DI pulse multipliers for single and independent approaches, and the corresponding accuracy limits, for rpm – BMEP of each case, see Figure 19.

As mentioned before, the single set was generated through sweep optimization, merging the 13 and 21 operating points for ULSD and B20, respectively. Conversely, the independent set was

obtained utilizing independently the 13 operating points for ULSD and the 21 operating points for B20.

Most of the cases for B20 and ULSD are within the IMEP accuracy limits (see **Figure *20*** and **Figure *21***). Cases 1, 2, and 8 present the highest error for both fuels, and lower errors were obtained in operation points with higher speeds. No significant differences were observed between the single and independent approach.

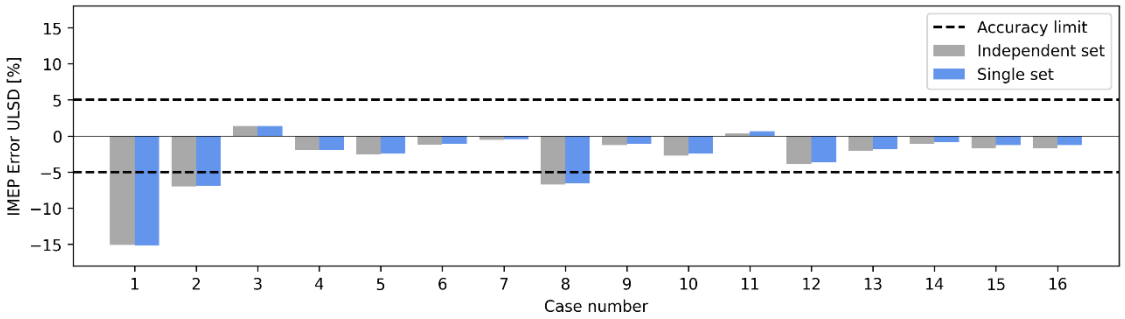

Figure 20. IMEP error, ULSD-DI-pulse model.

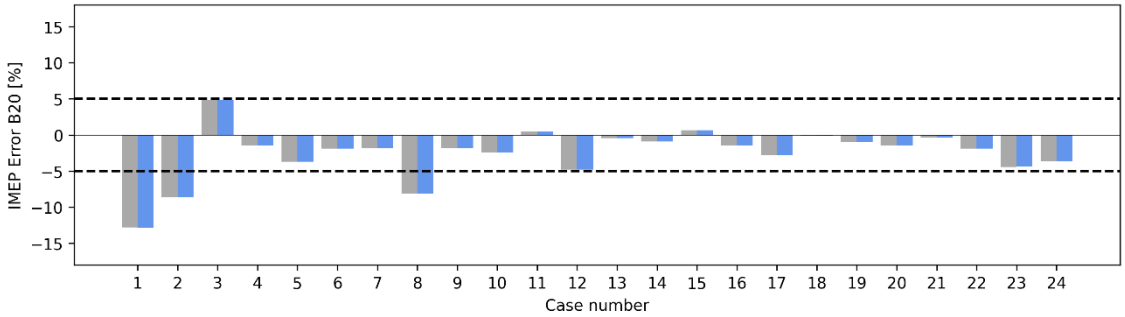

Figure 21. IMEP error, B20-DI-pulse model.

A slight improvement in CA50 error was obtained for the independent set in ULSD (Figure 21). Only one case is outside the accuracy limits in the CA50 for both fuels (**Figure *22*-Figure *23***). That particular case, differently from other operating points, presents two additional post-injection events, suggesting that the effect of multiple pulses in the injector object 'InjMultiProfileConn' may not be well captured due to model simplifications.

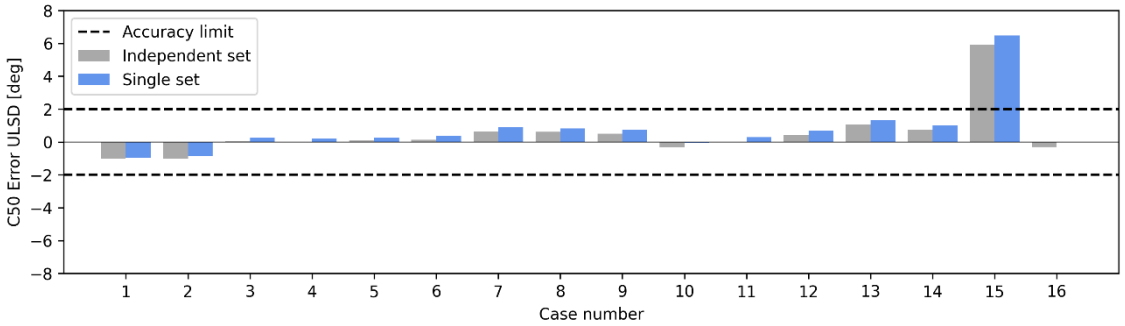

Figure 22. CA50 error, ULSD fuel-DI-pulse model.

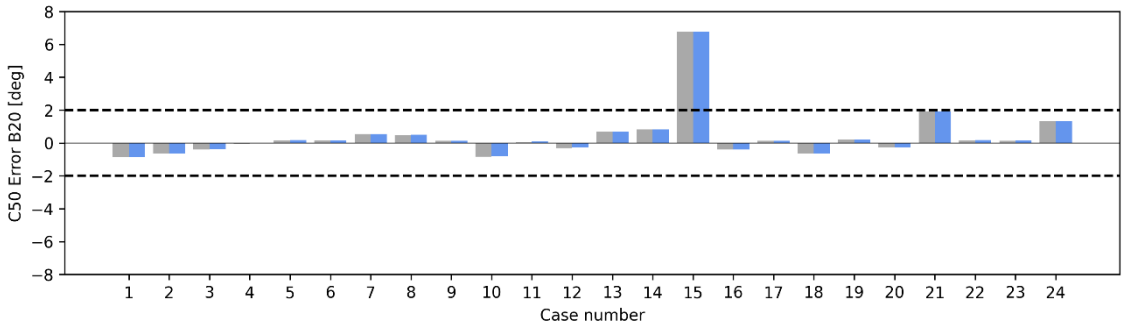

Figure 23. CA50 error, B20 fuel-DI-pulse model.

Good agreement of maximum in-cylinder pressure with experimental results was observed, with all cases within the accuracy limits (see **Figure *24*** and **Figure *25***). Lower errors were found for independent optimization in ULSD, and almost identical results for B20 using the two approaches.

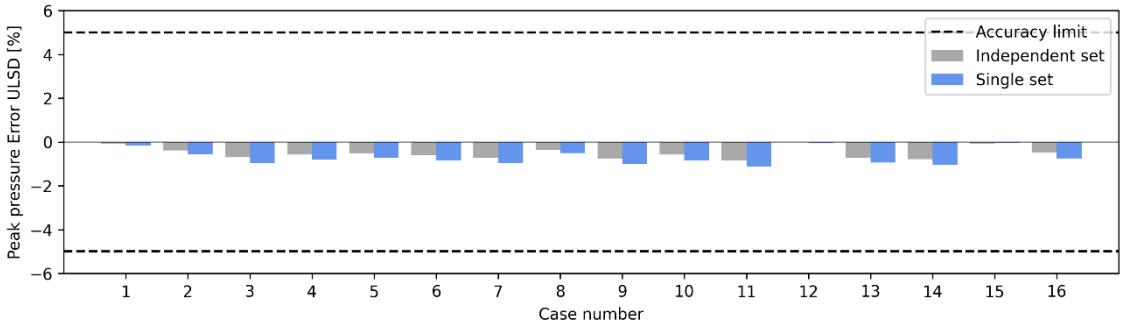

Figure 24. Peak pressure error, ULSD fuel-DI-pulse model.

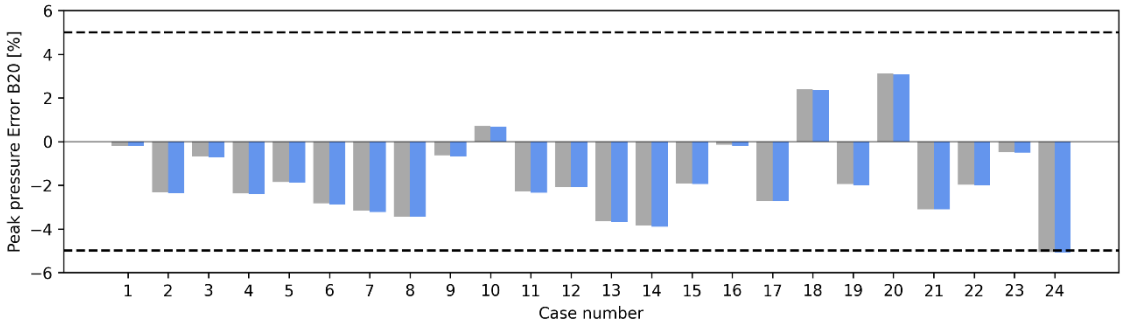

Figure 25. Peak pressure error, B20 fuel-DI-pulse model.

Higher deviations in CO2 emissions (see Figure 26-**Figure *27***) were observed at both high and low engine speeds. This aligns with the increased error in combustion parameters like C50 and IMEP simulated under similar conditions. However, it is important to note that most of these deviations remained within acceptable limits. Additionally, both independent and single-objective optimization approaches yielded comparable outcomes.

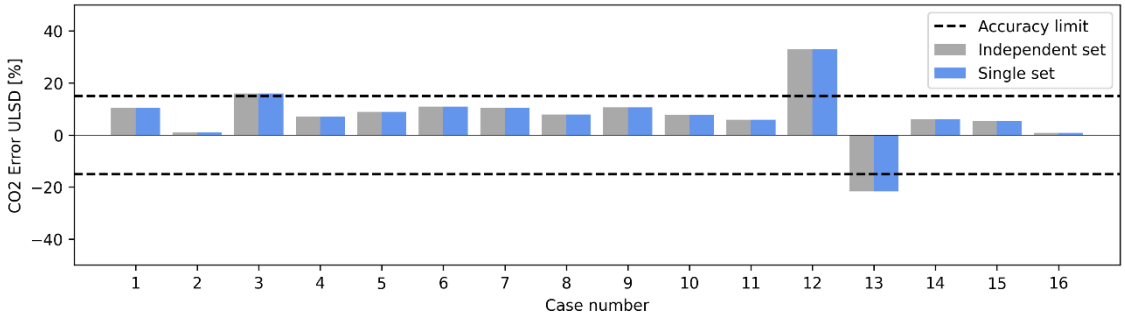

Figure 26. CO2 error, ULSD fuel-DI-pulse model.

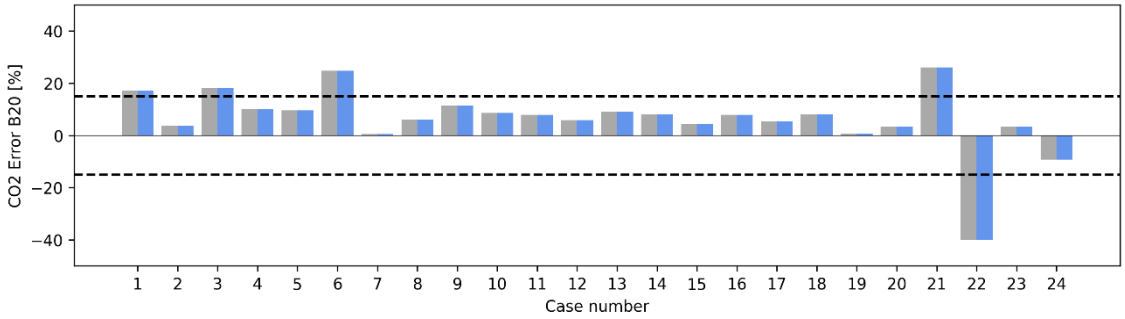

Figure 27. CO2 error, B20 fuel-DI-pulse model.

Comparison of the validation results using multipliers obtained from the independent set and single-set optimization, indicated that the tendency of the errors was very similar in most of the parameters, with a slight improvement in CA50 and peak pressure for ULSD in single-case. No clear effect of the speed or load on error was found in most parameters, except for IMEP and CO_2. Therefore, a single approach was selected for the other simulations.

Figure *28* and **Figure *29*** shows the results for NOx emissions. Although the combustion parameters appear to be well predicted, unexpected and higher errors were obtained for NOx emissions. Although these values show lower accuracy than recent works [102], [106], most of the predicted results met the accuracy target, and the B20 vs. ULSD trend was well captured, as is discussed in the following sections.

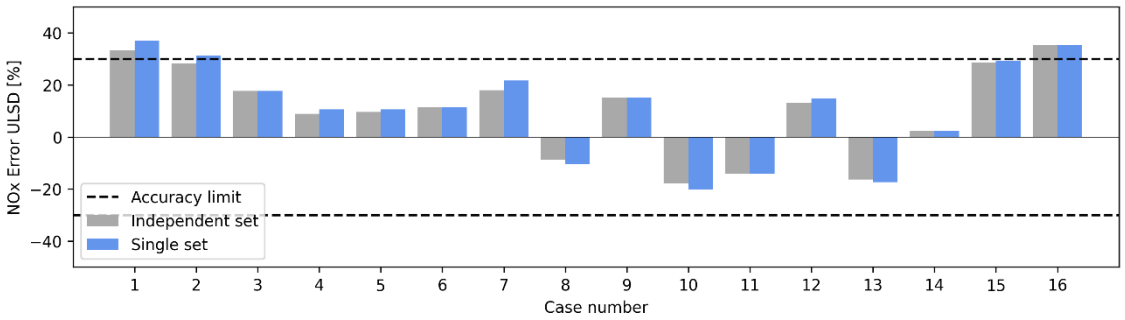

Figure 28. NOx error, ULSD fuel-DI-pulse model.

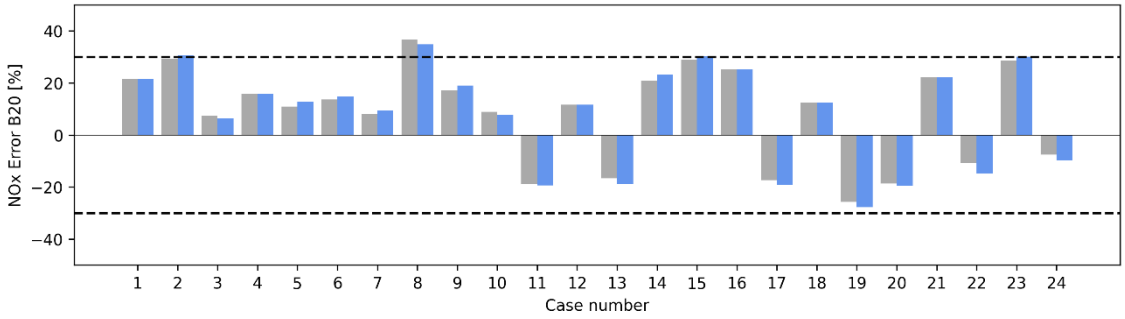

Figure 29. NOx error, B20 fuel- DI-pulse model.

As mentioned before, after completing the calibration of the DI-Pulse combustion, NOx emissions, and the full engine model, a validation process was conducted by comparing the measured data with the simulated results.

3.2 Engine model validation

Figure *30* to **Figure *32*** compare predicted and measured data for both ULSD and B20 fuels. All calibration and validation points are included in the plots. Good agreement was obtained between experimental and predicted combustion and performance parameters (IMEP, CA50, peak cylinder pressure, fuel consumption) (Figure 29), most of the cases within accuracy targets (**Table *14***) and $R^2 > 0.94$ for ULSD and $R^2 > 0.88$ for B20 (see **Table *17***). The larger errors observed for B20 can be attributed to model simplifications. For instance, the injection profiles used were obtained for pure diesel [98], and fuel spray and atomization processes, which depend on fuel properties such as density, viscosity, latent heat of vaporization, surface tension and vapor pressure [107], may not be well represented for the B20 blend.

To address these limitations and improve the accuracy of B20 simulations, some approaches could be explored, for instance: develop B20-specific injection profiles to account for B20's unique density, viscosity, and vapor pressure by acquiring or creating dedicated injection profiles. Enhance fuel property modeling to ensure the model accurately captures the thermodynamic and physical properties of B20 compared to pure diesel.

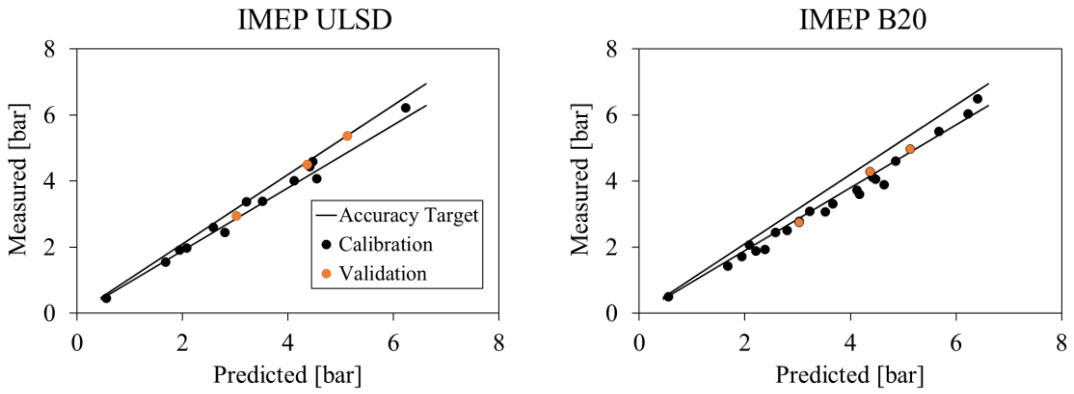

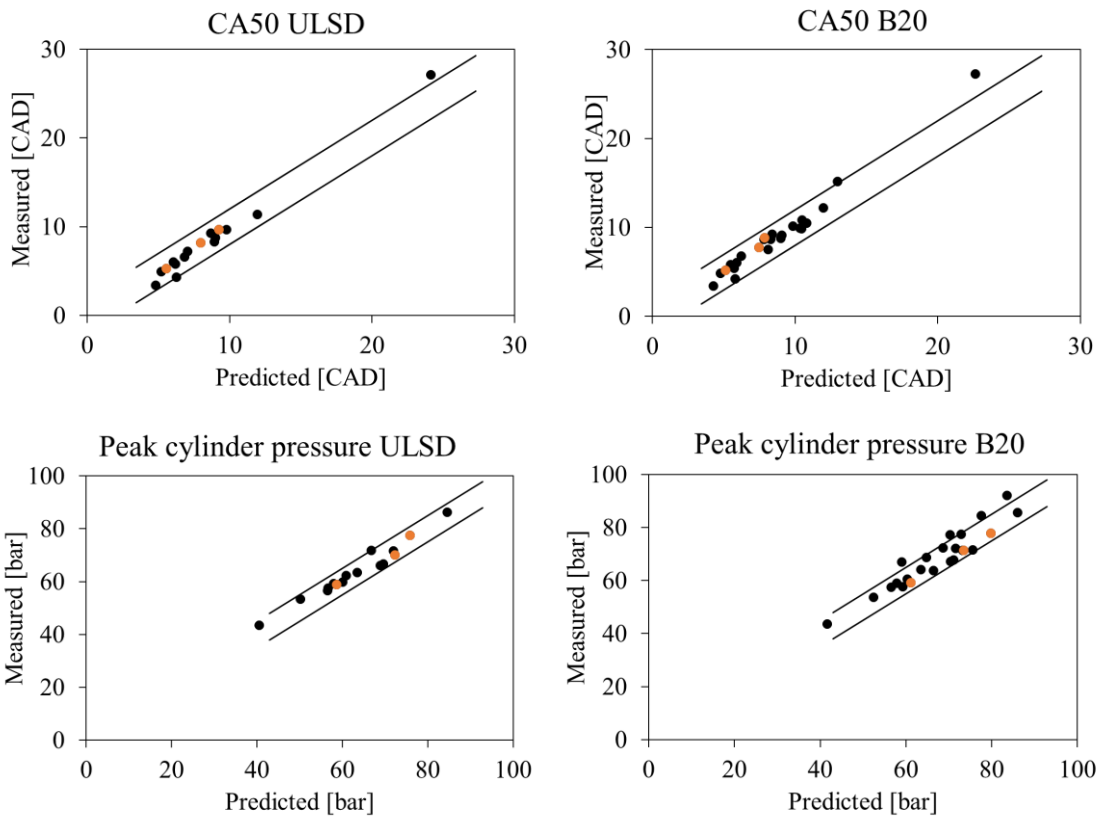

Figure 30. Engine model validation: combustion parameters.

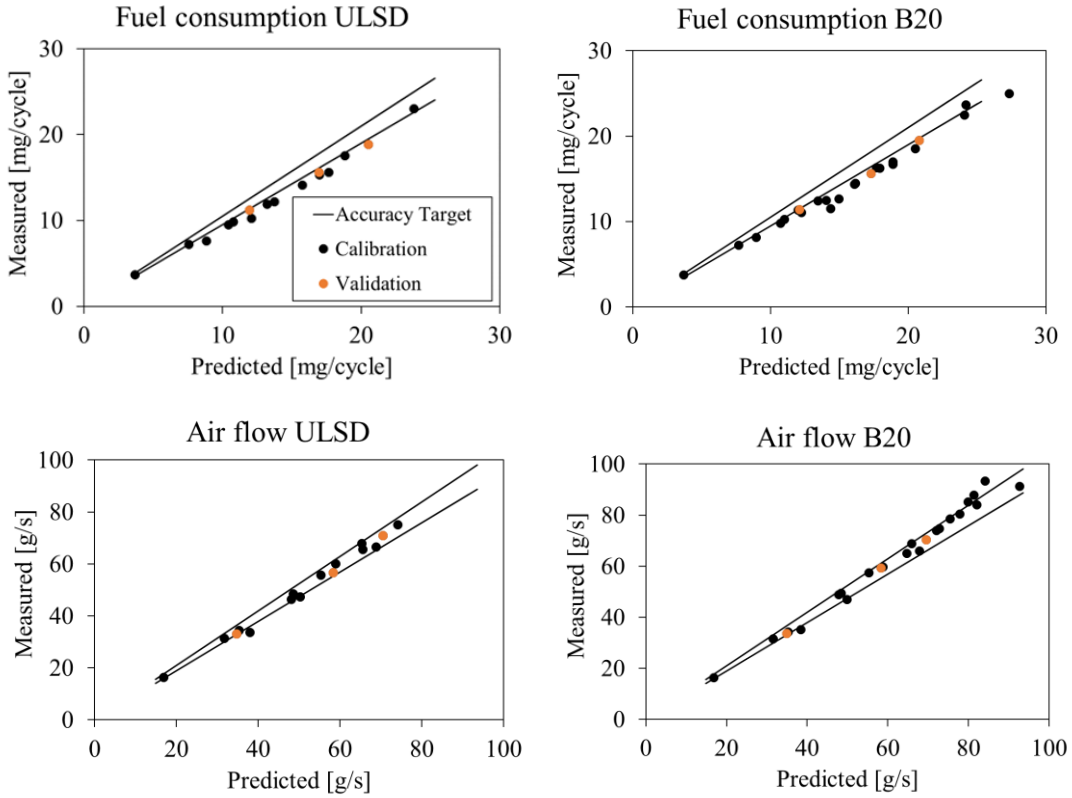

Figure 31. Engine model validation: performance parameters.

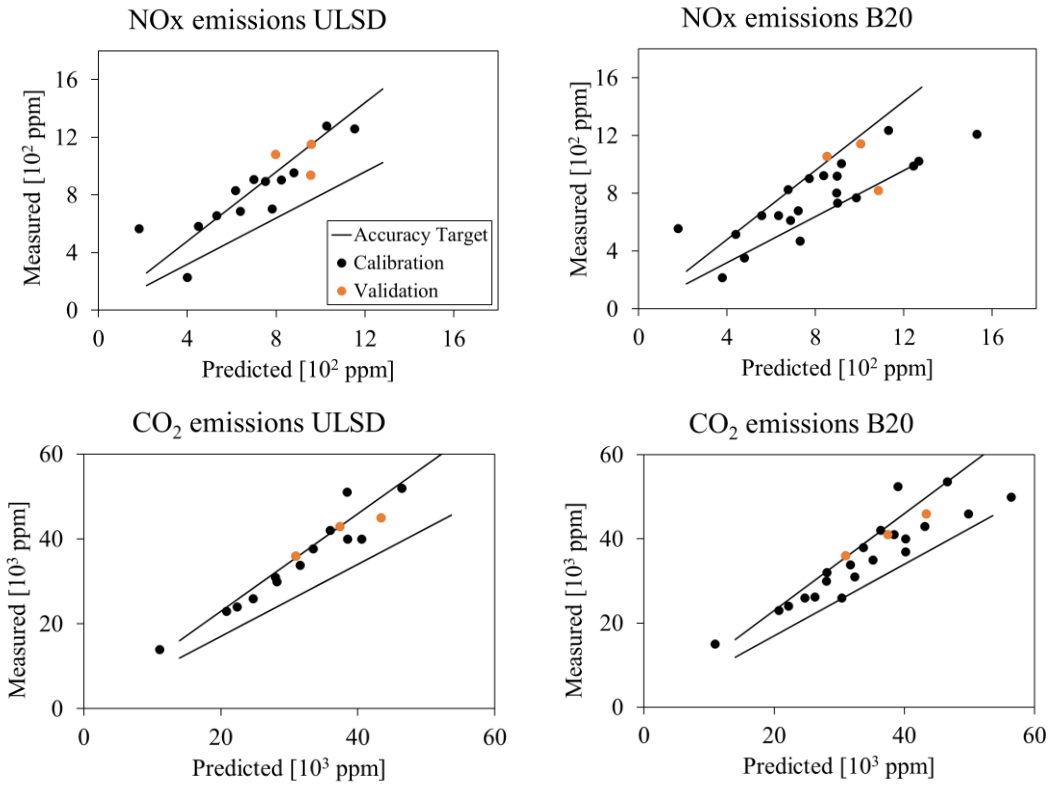

Figure 32. Engine model validation: emissions.

Table 17. Correlation (R) and Determination (R2) coefficients for all compared parameters.

	ULSD		B20	
Parameter	R	R^2	R	R^2
IMEP	0.99	0.99	0.99	0.98
CA50	0.99	0.99	0.99	0.97
Peak Cylinder Pressure	0.98	0.96	0.94	0.88
Air flow Rate	1.00	0.99	0.99	0.99
Fuel consumption mg/cycle	1.00	0.99	0.99	0.99
NOx emissions Concentration	0.87	0.75	0.81	0.65
CO_2 emissions Concentration	0.96	0.92	0.91	0.83

A good correlation for CO_2 emissions was found, with R^2 values of 0.92 and 0.83 for ULSD and B20, respectively (Table 15). Moreover, most model results were within the error targets or very close to the upper limit, suggesting that chemical equilibrium is a good approach for in-cylinder combustion models; in fact, other studies have also shown good correlation between measured and predicted CO_2 using this approach [108], [109]. Although lower R^2 values were obtained for NOx emissions (0.75 and 0.65 for ULSD and B20, respectively), which are somewhat lower than recent works [102], [106], most of the predicted results met the accuracy target, and the B20 vs. ULSD trend was well captured.

As previously discussed, refining the model to incorporate B20's unique fuel properties and improve injection and spray modeling could potentially enhance the accuracy of combustion

predictions, subsequently impacting calculated NOx emissions. Additionally, this study only explored two optimization parameters for the NOx model based on GT recommendations (Table 13). However, the NOx model includes four additional parameters with the potential to influence accuracy:

- N_2 Oxidation rate multiplier.
- N oxidation rate multiplier.
- N oxidation activation energy multiplier.
- OH reduction rate multiplier.

Including these parameters in the optimization process could potentially lead to more reliable results by allowing the model to better capture the specific behavior of B20 combustion and NOx formation.

Finally, good agreement was also found for in-cylinder pressure and burn rate versus crank angle for the operation conditions used to validate the model, **Figure *33***.

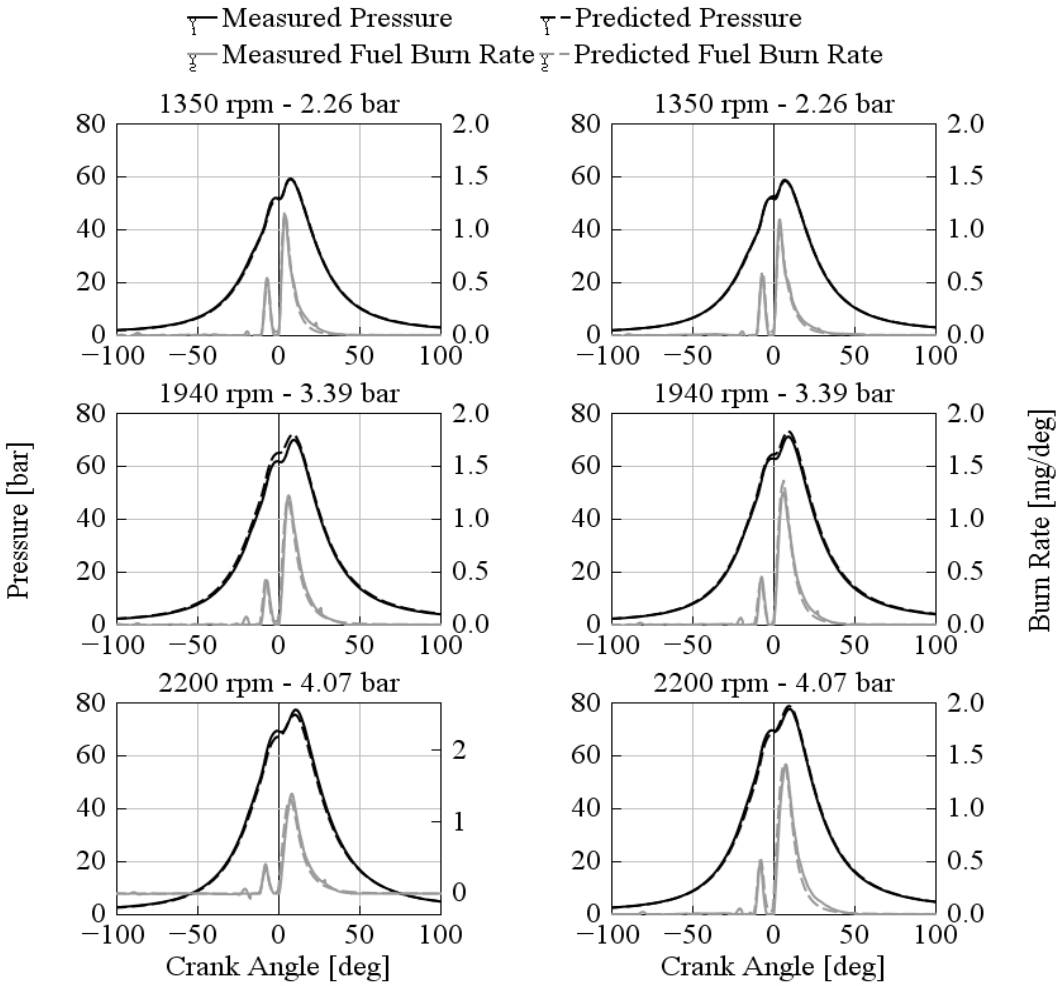

Figure 33. Engine model validation: In-cylinder pressure and burn rate (a) ULSD – (b) B20.

Engine simulation model with DI-pulse demonstrated several strengths and weaknesses based on its performance with ULSD and B20 fuels. On the positive side, the model achieved excellent correlations for CO_2 emissions for ULSD and B20. Additionally, most model performance and combustion results fell within the defined error targets.

However, there are areas for improvement, particularly regarding NOx prediction accuracy for B20. This could be addressed by refining the model to account for B20's unique properties like density and viscosity and exploring the optimization of all available parameters within the NOx model.

Despite the mentioned limitations, the engine model with DI-Pulse was considered valid, therefore a calibration and validation process were conducted for the second combustion model (DISRM). The following section shows the results of this process. It is worth mentioning that all simulations were performed under the same operation conditions as the DI-Pulse model.

3.3 Calibration of the Predictive Combustion Model (DISRM)

This section describes first the method and data used to obtain representative combustion mechanisms and surrogates to simulate the studied fuels.

In order to obtain a valid comparison between the mechanism and surrogates, all simulations were conducted using the same model constants, which were the default values provided by GT (see **Table *18***).

Table 18. DISRM multipliers.

Constant	Value
Scalar Mixing Multiplier	2.0
Frequency Decay Constant	1.5
Minimum Frequency Decay Rate	0.8
Cutoff Frequency Multiplier	2.0

3.3.1 ULSD mechanism selection

As mentioned before, mechanisms were selected that enable simulation without encountering errors or warnings. The chosen mechanisms were then subjected to a data consistency analysis using the CPOA tool. Subsequently, the 2000 rpm and 50 Nm operating mode was simulated. At this stage, the ULSD and B100 surrogates proposed by the same authors were employed for each mechanism to be evaluated (Table 3 and Table 4). Results of the tests conducted to determine the mechanisms of ULSD combustion are summarized in **Table *19***.

Mechanisms 4 and 5 were discarded due to errors in the consistency checks. In addition, mechanism 5 failed to predict ignition. Mechanisms 1 and 3 had the lowest errors for the IMEP, -1.99% and -2.27%, respectively. However, mechanism 2 provided better results for CA50 and peak pressure, with errors of -1.69 deg and 2.1 bar. Moreover, mechanism 2 had lower errors in predicting NOx and CO_2 emissions. When considering simulation time, mechanism 3 almost doubled (62 min) the other options due to the higher number of species and reactions.

Table 19. Results of preliminary testing to select USLD mechanism.

#	Mechanism	Consistency checks passed/total	Simulation results @ 2000 rpm -2.26 bar	Simulation time [min]
1	(Hernández et al., 2014) [60]	16/16	IMEP during Combustion error: -1.99 % Improved Burn rate RMS error: 0.013 CA50 Error: -1.8 deg Peak Pressure Error: 2.88 bar NOx error: - CO_2 error: 10.99%	27.55
2	(Wang et al., 2015) [61]	14/16	IMEP during Combustion error: -2.27 % Improved Burn rate RMS error: 0.010 CA50 Error: -1.69 deg Peak Pressure Error: 2.10 bar NOx error: -5.4% CO_2 error: 12.3%	31.00
3	(Ren et al., 2017) [62]	14/16	IMEP during Combustion error: -1.93 % Improved Burn rate RMS error: 0.013 CA50 Error: -2.5 deg Peak Pressure Error: 4.68 bar NOx error: 8.06 CO_2 error: 13.11%	62.37
4	(Yu et al., 2018) [63]	0/16	-	12.54
5	(Bai et al., 2020)) [64]	-	Error	-

Figure *34* displays the predicted in-cylinder pressure for each tested mechanism. Mechanisms 1 and 2 slightly underpredicted both pressure peaks but closely matched the peak position, whereas mechanism 3 did not predict accurately the second, higher peak of pressure, and mechanism 4 predicted poor combustion in the main fuel injection event, resulting in a higher error in the second peak pressure. Mechanism 2 accurately predicted the heat release by pilot injection (see **Figure *35***), mechanisms 1 and 3 exhibiting delayed ignition and mechanism 4 showing early ignition. In addition, mechanisms 1 and 2 are more effective in capturing the heat release during the main injection.

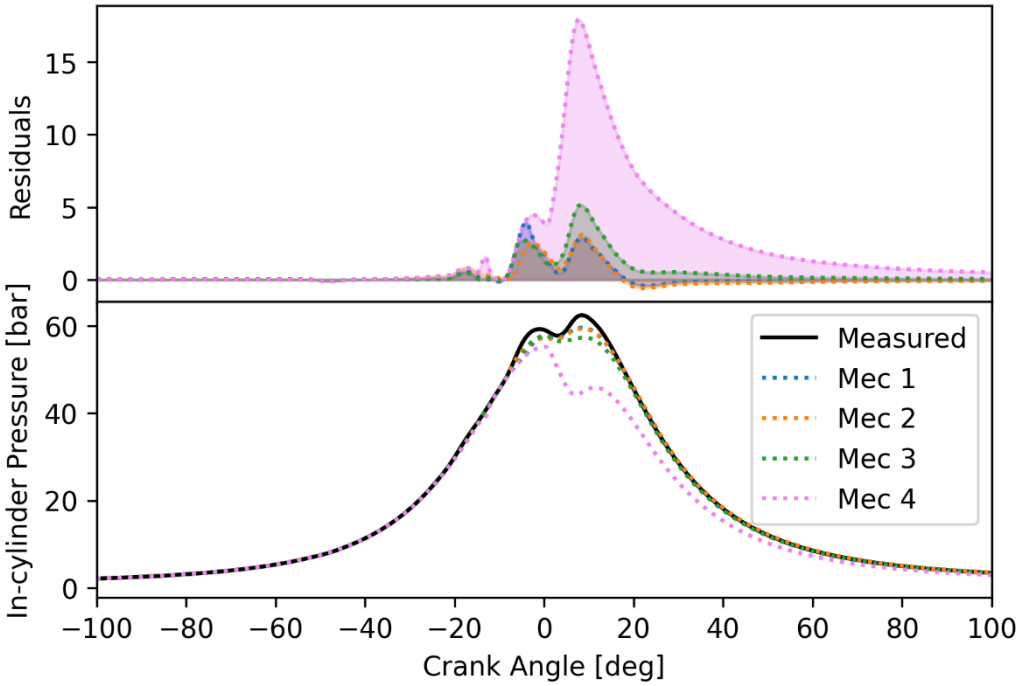

Figure 34. Simulated in-cylinder pressure for each reaction mechanism ULSD. Residuals equals to difference between measured and predicted profiles.

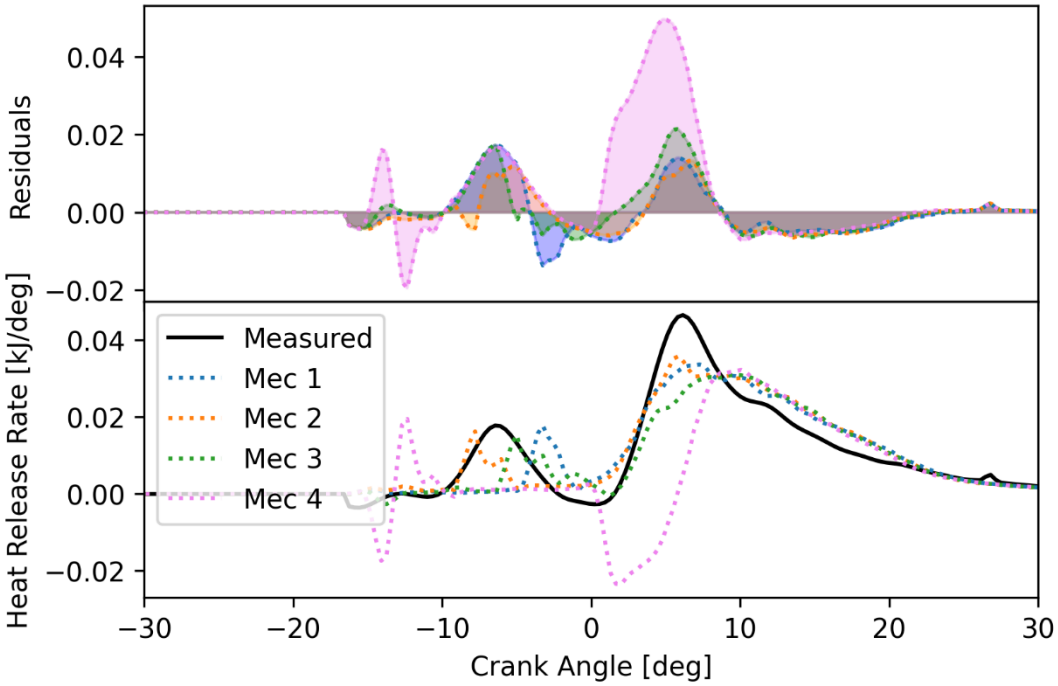

Figure 35. Simulated heat release rate for each reaction mechanism ULSD. Residuals equals to difference between measured and predicted profiles.

Mechanism 2 was selected for further simulations due to its performance in terms of lower errors in simulated parameters and emissions, coupled with a reduced simulation time compared to other options.

3.3.2 Biodiesel mechanism selection

Since experimental data for B100 was not available, B20 data was used as the basis for comparison with the predicted results. Therefore, most of the results presented here are intended for qualitative analysis and have provided useful combustion parameters insights with reasonable simulation time.

A BD mechanism was selected using the same procedure as ULSD. The results are displayed in **Table *20***. Mechanism 4 was excluded from the analysis as it failed to simulate ignition. All the tested mechanisms had a small number of approved consistency checks, what was to be expected, due to significant differences between B100 and B20 conditions during simulations. Mechanism 2 presented a better simulation time and similar errors than mechanism 1. Higher differences in IMEP, peak pressure, as well as on burn rate error were found in mechanism 3.

Table 20. Results of preliminary testing to select a biodiesel mechanism.

#	Mechanism	Consistency checks passed/total	Simulation results @2000 rpm -2.26 bar	Simulation time [min]
1	(Luo et al., 2012) [65]	5/24	IMEP during Combustion error: -1.8 % Improved Burn rate RMS error: 0.011 CA50 Error: -1.21 deg Peak Pressure Error: 1.49 bar	37.29
2	(Brakora & Reitz, 2010) [66]	5/24	IMEP during Combustion error: -5.44 % Improved Burn rate RMS error: 0.012 CA50 Error: -1.48 deg Peak Pressure Error: 2.67 bar	9.51
3	(Zhang et al., 2020) [67]	4/24	IMEP during Combustion error: -5.38 % Improved Burn rate RMS error: 0.014 CA50 error: -2.29 deg Peak Pressure error: 4.18 bar	45.02
4	(Bai et al., 2021) [68]	-	Error	-

Figure *36* and **Figure *37*** compare the measured B20, and the predicted in-cylinder pressures and the heat release rate (HRR) for B100, respectively. Mechanisms 1 and 2 resulted in almost identical in-cylinder pressures, except for a minor difference in the second pressure peak, whereas mechanism 3 showcased higher differences, with lower pressures for both peaks. The simulated HRR results for mechanisms 1 and 2 indicate similar ignition delays, but there were significant

differences in the heat released during the pilot injection events. On the other hand, mechanism 3 did not produce any heat release during the pilot injection event.

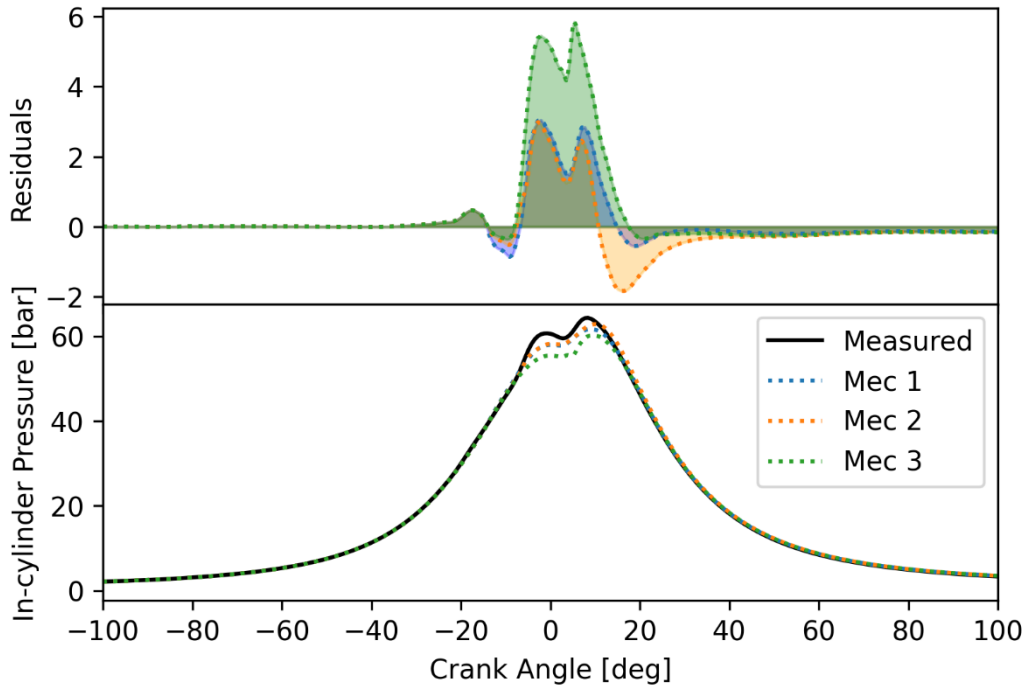

Figure 36. Simulated in-cylinder pressure for each reaction mechanism B20. Residuals equals to difference between measured and predicted profiles.

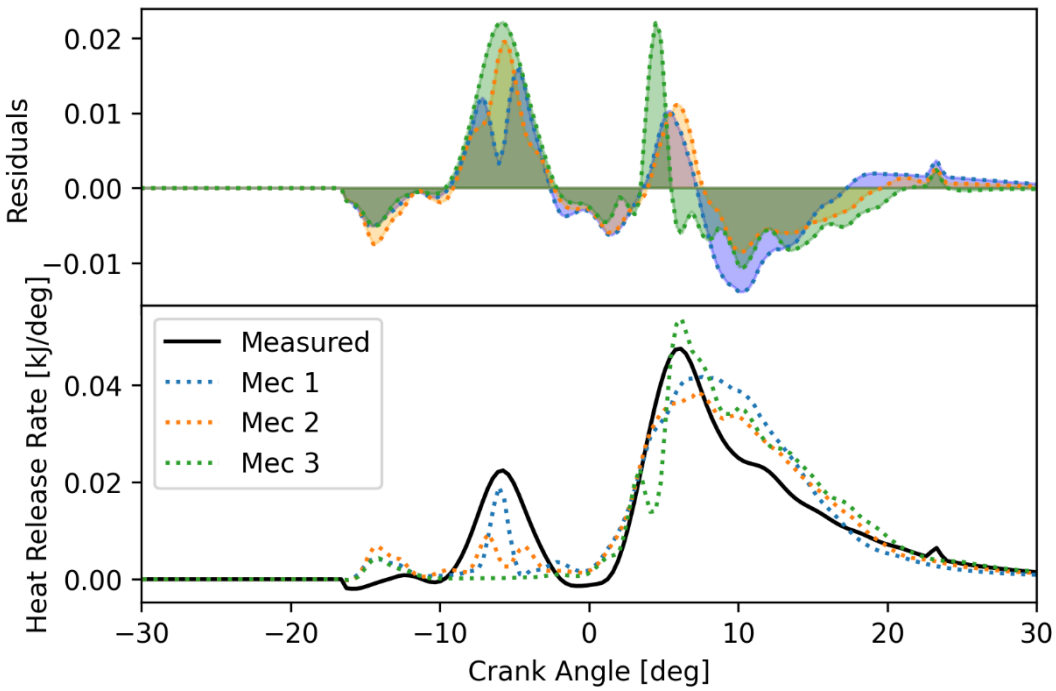

Figure 37. Simulated heat release rate for each reaction mechanism B100. Residuals equals to difference between measured and predicted profiles.

Mechanism 3 was not considered due to the non-standard behavior in the simulated heat release rate (HRR) and the high computational cost. Mechanisms 1 and 2 had comparable results, but mechanism 1 showed slightly better prediction accuracy, and was chosen for further testing.

Following the pre-selection of mechanisms for ULSD and BD discussed previously, the study implemented the merging of these mechanisms into a single, comprehensive one. The performance of this merged mechanism was evaluated using the same methodology employed for the individual mechanisms. Additionally, new compositions for the selected surrogate fuels were proposed based on the specific properties of the fuels used in this study. Finally, by considering consistency checks, combustion model predictions, and simulation time, the most suitable surrogates for ULSD, B20, and HVO20 were determined.

3.3.3 Selection ULSD surrogate.

The selection of a suitable surrogate fuel for ULSD simulation is a critical step in ensuring the accuracy and reliability of results. The surrogate must mimic the properties and behavior of ULSD, considering its chemical composition, combustion characteristics, and emissions. Three surrogates were tested based on *n*-heptane and toluene mixtures to represent the paraffinic and aromatic components, respectively, of diesel fuel (see Table 21).

Table 21. ULSD surrogates.

Surrogate ULSD	1 (Wang et al., 2015) [61]	2 (This work)	3. (Wang et al., 2015) [61]
wt.% *n*-Heptane	82.2	71.7	65.5
wt.% Toluene	17.8	28.3	34.5

Figure 38 depicts the errors between the physicochemical properties of each surrogate fuel and the corresponding real fuel. These surrogate property estimations were derived from the approaches presented in [63].

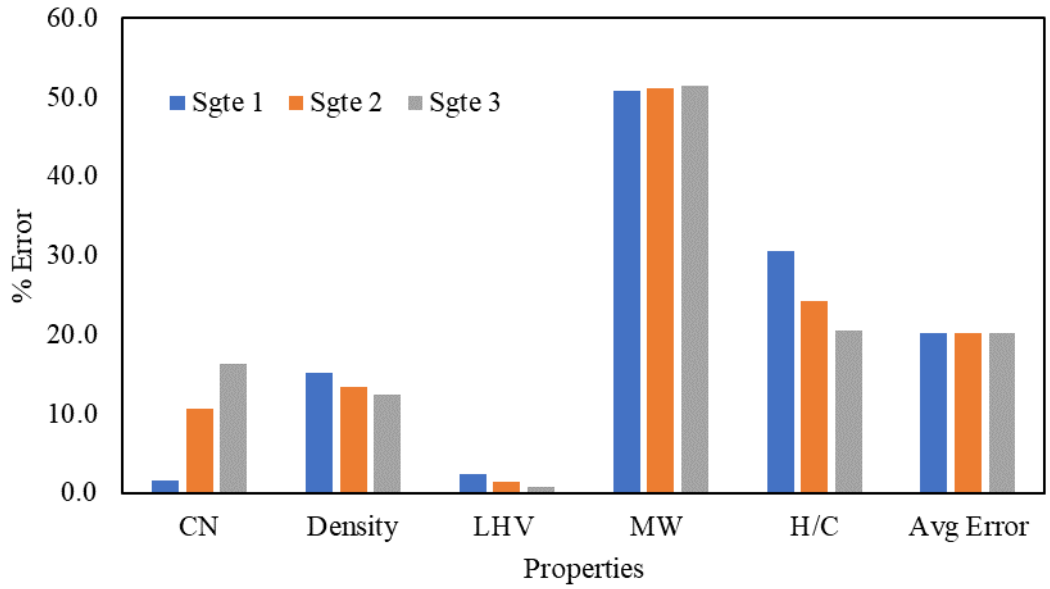

Figure 38. Chemical and physical properties error for tested ULSD surrogates.

All three surrogate mixtures have densities and lower heating values that closely match those of ULSD, but there are large errors in the molecular weight and hydrogen-carbon ratio. Surrogate 1 better represents the cetane number, surrogates and 3 showing a larger error. However, when considering all the properties collectively, the average error for all three surrogates is very similar. This suggests that while individual properties may exhibit variations, the overall representation of ULSD by these surrogates remains consistent.

All surrogates passed the same number of consistency checks (see ***Table 22***). Failed cases correspond to the same conditions as DI-Pulse combustion model. Surrogate 1 exhibited a lower error in the parameters evaluated and significantly improved NOx emissions prediction, respect to surrogates 2 and 3, while Surrogate 3 resulted in higher errors. Although all quantities are within the accuracy limits, some slight differences can be observed in combustion behavior, as shown in **Figure *39*** and ***Figure 40***.

Table 22. Consistency checks and simulated results for ULSD surrogates.

Surrogate ULSD	Consistency checks ULSD. passed/total	Simulation results simulation @2000 rpm -2.26 bar	Simulation time [min]
1	14/16	IMEP during Combustion error: -1.96 % Improved Burn rate RMS error: 0.011 CA50 Error: -1.53 deg Peak Pressure error: 1.92 bar NOx error: -5.87 CO_2 error: 11.9%	69.71

2	14/16	IMEP during Combustion error: -2.27 % Improved Burn rate RMS error: 0.010 CA50 Error: -1.69 deg Peak Pressure error: 2.10 bar NOx error: -9.88% CO_2 error: 12.3%	70.20
3	14/16	IMEP during Combustion error: -2.30 % Improved Burn rate RMS error: 0.011 CA50 Error: -1.77 deg Peak Pressure Error: 2.4 bar NOx error: -8.93 % CO_2 error: 10.64 %	69.86

Figure *39* shows the measured and simulated HRR for the tested surrogates using the merged mechanism. Surrogate 1, with a lower toluene content, displayed an improved agreement in predicting ignition delay because of the better fitting to the cetane number (CN), which can explain the lower errors in NOx emissions. However, it overpredicts the maximum heat release during the pilot injection event and underpredicts the main injection event. Surrogates 2 and 3, characterized by increased toluene content, demonstrated advanced ignitions compared to Surrogate 1. Indeed, larger contents of toluene, an aromatic compound, are known to enhance ignition [110].

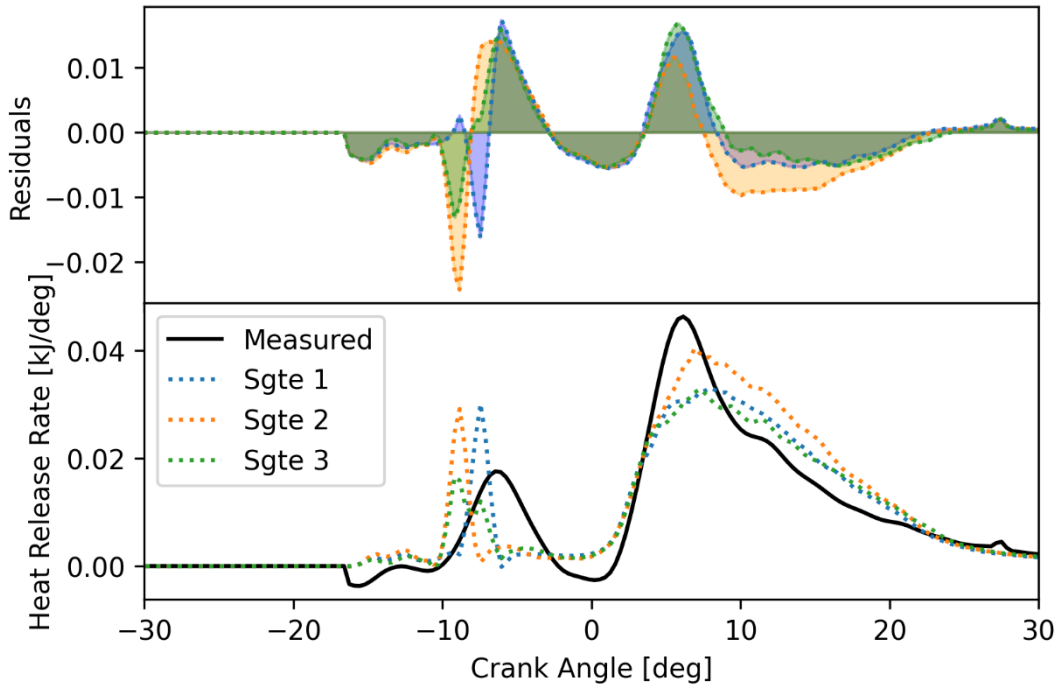

Figure 39. Simulated heat release rate for each ULSD surrogate. Residuals equals to difference between measured and predicted profiles.

All three surrogates, despite their different compositions, demonstrated remarkable consistency in predicting cylinder pressure throughout the combustion process (see

Figure *40*), indicating that they effectively capture the fundamental combustion characteristics associated with fuels. The very small difference in maximum pressure between predictions and measurements (2 bar) supports the reliability of the results under the simulated conditions.

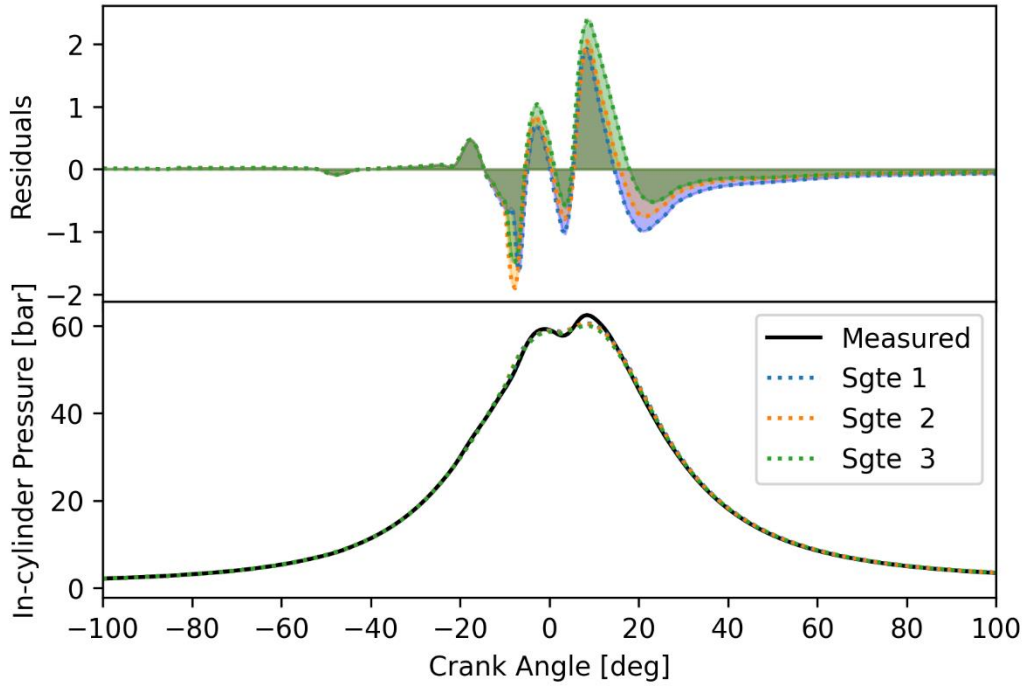

Figure 40. Simulated in-cylinder pressure for each ULSD surrogate. Residuals equals to difference between measured and predicted profiles.

While all surrogate fuels exhibited good agreement between predicted and experimental data, meeting the established accuracy criteria, surrogate 1 displayed the lowest error for NOx emissions. This potentially relates to its more accurate ignition time, which closely matched the experimental observations (**Figure *39***). Consequently, surrogate 1 was chosen for further simulations.

3.3.4 Biodiesel surrogate selection

B20 fuel is created in GT-Suite by defining pure ULSD and biodiesel surrogates and specifying the percentage of each one in the mixture. In this case, the mixture contains 20 vol.% biodiesel. Consequently, the biodiesel surrogates presented below correspond to B100, while B20 is represented by the results obtained by combining the selected ULSD and B100 surrogates.

The biodiesel (B100) surrogates evaluated (see Table 23) are a mixture of methyl decanoate (MD), methyl-9-decanoate (MD9D) and *n*-heptane, which allows flexibility in matching the physical and combustion properties of biodiesel from different feedstocks [65]. Out of the six surrogates initially considered, some were discarded due to their significant similarities in chemical and physical properties. In particular, as surrogates 3 and 4 had errors are similar to those of 1 and 2,

respectively, and surrogate 6 was similar to surrogate 1 (see **Figure *41***), surrogates 3, 4 and 6 were abandoned.

Table 23. B100 surrogates.

Surrogate B100 (wt. %)	1 (Luo et al., 2012) [65]	2 This work	3 (Brakora & Reitz, 2010) [66]	4 (Luo et al., 2012) [65]	5 Singapore Nat. U - 2014	6 Wisconsin U. – 2013 [111]
Methyl decanoate	32.63	27.60	32.00	27.69	47.93	31.98
Methyl 9 decanoate	32.27	24.70	32.90	24.59	42.23	32.92
n-Heptane	35.10	47.70	35.10	47.72	9.84	35.10

Figure 41. Chemical and physical properties error for tested BD surrogates.

All surrogates presented high errors (27.3-31.9%) in cetane number and molecular weight (43.5-59.4%), possible due to the range of fatty acid methyl esters (FAMEs) with varying chain lengths and branching present in biodiesel, MD and MD9D representing only a subset of these esters. In addition, Cetane Number is not only dependent on the presence of esters but also on the distribution of different FAMEs, each with its own ignition characteristics. Despite the challenges in replicating the Cetane Number, it is worth noting that the surrogates exhibited a good match in terms of density, lower heating value, and hydrogen-to-carbon (H/C) ratio, with errors below 11%. Thus, the surrogates should be suitable for capturing the physical properties of biodiesel that are important for modeling combustion and energy content.

The B20 surrogates studied exhibited errors in IMEP, CA50, peak pressure, and NOx and CO_2 emissions within the acceptable limits of accuracy (see **Table *24***), thus performing well in modeling these critical combustion parameters.

Some differences arise, particularly in NOx emissions, from B20 with respect to conventional diesel (USLD). These divergences point to variations in combustion characteristics and emissions formation between B20 and USLD. In fact, NOx emissions are highly sensitive to combustion conditions, and even slight differences in ignition timing or combustion behavior can significantly impact NOx formation [112]. Surrogate 2 appears to offer slightly improved prediction capabilities in some parameters (see **Table *24***).

Table 24. Consistency checks and simulated results for B20 surrogates.

Surrogate B20	Consistency checks B20 passed/total	Simulation results @ 2000 rpm -2.26 bar	Simulation time [min]
1	21/24	IMEP during Combustion error: -2.07 % Improved Burn rate RMS error: 0.014 CA50 Error: -1.61 deg Peak Pressure Error: 2.38 bar NOx error: -17.47 CO2 error: 3.97%	69.51
2	21/24	IMEP during Combustion error: -1.92 % Improved Burn rate RMS error: 0.014 CA50 Error: -1.78 deg Peak Pressure Error: 2.65 bar NOx error: -14.83% CO2 error: 3.52 %	69.30
5	21/24	IMEP during Combustion error: -2.99 % Improved Burn rate RMS error: 0.014 CA50 Error: -1.85 deg Peak Pressure Error: 2.4 bar NOx error: -16.7 % CO2 error: 5.76 %	70.10

Figure 42 and **Figure *43*** display the experimental and simulated heat release rate and in-cylinder pressure, respectively, for the B20 blend using the three selected surrogates. Significant differences in the heat release rate are observed, the discrepancy being more pronounced during the injection pilot event. This indicates that the surrogates cannot replicate exactly the combustion behavior of the B20 blend, particularly during the early stages of combustion. Surrogate 2 displayed a closer agreement with the experimental ignition timing, which is consistent with its better value of the cetane number. In contrast, Surrogates 1 and 5 exhibited advanced ignitions.

During the controlled combustion phase, no significant differences were observed between the surrogates, suggesting that they all effectively represent this part of the combustion process. However, discrepancies emerged in the post-peak behavior of the heat release rate: the rate of decrease in the heat release rate was lower in the simulated cases compared to the experimental data.

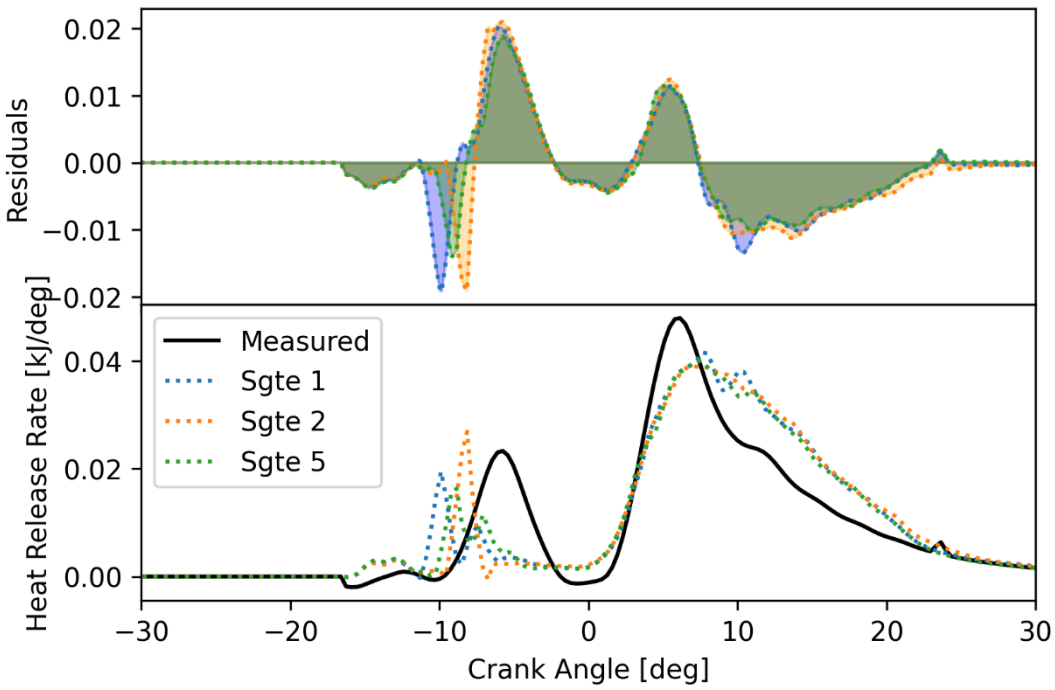

Figure 42. Simulated heat release rate for B20 surrogates. Residuals equals to difference between measured and predicted.

Differently from HRR, no significant differences were found for predicted pressure traces. Although the surrogates may exhibit different ignition characteristics during the ignition pilot event, as it was already mentioned, their similar behavior during the controlled combustion phase makes them match closely in terms of combustion duration, and maximum heat release, and, therefore, result in similar in-cylinder pressure profiles during this phase. Simulated maximum pressure was within 2 bar of the experimental value.

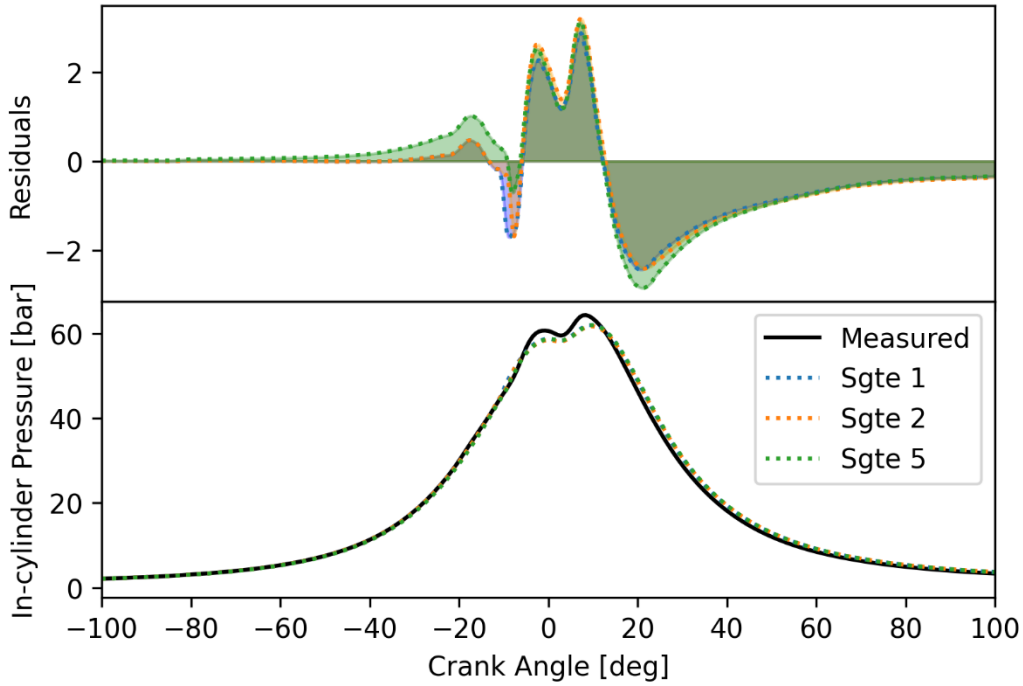

Figure 43. Simulated in-cylinder pressure for each B100 surrogate. Residuals equals to difference between measured and predicted.

The results demonstrate that all tested B20 surrogates effectively captured the fuel overall combustion behavior, with all compared quantities within the specified accuracy targets. The selection of the surrogate was based on the smallest differences that resulted in improved accuracy for emissions and combustion parameters. Therefore, surrogate 2 was chosen for the subsequent simulations.

Table *25* presents the details of the merged mechanism and the final selected surrogates. Since pure HVO was represented by n-heptane, the same surrogates were considered for HVO20 as for ULSD, with adjustments made for aromatic compounds.

Table 25. Merged mechanism and surrogates for ULSD, B20, HVO20.

Merged mechanisms: ULSD: (Wang et al., 2015) [61] BD: (Luo et al., 2012) [65]	624 reactions 142 species		
Surrogates % mass			
Species	**ULSD**	**B20**	**HVO20**
Methyl decanoate	-	5.9	-
Metil-9-decenoato:	-	5.3	-
n-Heptane	82.2	74.8	85.6
Toluene	17.8	14.0	14.4

After selecting the mechanisms and surrogates for ULSD and B20, the model was calibrated. However, the higher computational cost associated with the reaction chemistry in the DISRM model prevented the implementation of a calibration methodology similar to that of the DI-Pulse model. In fact, optimization would have exceeded the available computational resources. Therefore, certain considerations were made. The adjustment of the DISRM model calibration constants was performed manually, aiming to minimize the error in the compared combustion and emissions parameters. This resulted in a set of constants for ULSD and B20. The model validation was conducted following the same DI-pulse methodology.

Figure *44*-47 present the deviation (error %) with respect to the measured values for combustion parameters and emissions, along with the accuracy limits. Case number corresponds to the operation conditions illustrated in Figure 19.

Figure *44* and **Figure *45*** shows the IMEP error of all the operating points for ULSD and B20, respectively. With the exception of case 1, the maximum absolute error is less than 8%. Figure 46 and Figure 47 shows the CA50 error for ULSD and B20, respectively; both the computed and measured values of CA50 were derived from the computed and measured pressure traces, respectively. Only one case (case 15) falls outside the limits for both fuels. Generally, the computed error is relatively small, and it performs reasonably well over all operating points. On the other hand, ***Figure 48*** and ***Figure 49*** show the error in maximum pressure, with the absolute maximum pressure error within 5 bar for ULSD and 7.6 bar for B20; the rest of the cases fall within the accuracy limits.

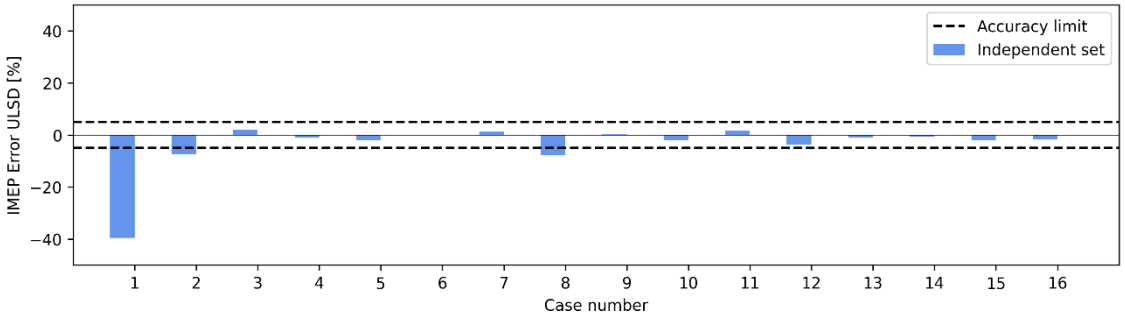

Figure 44. IMEP error, ULSD fuel-DISRM.

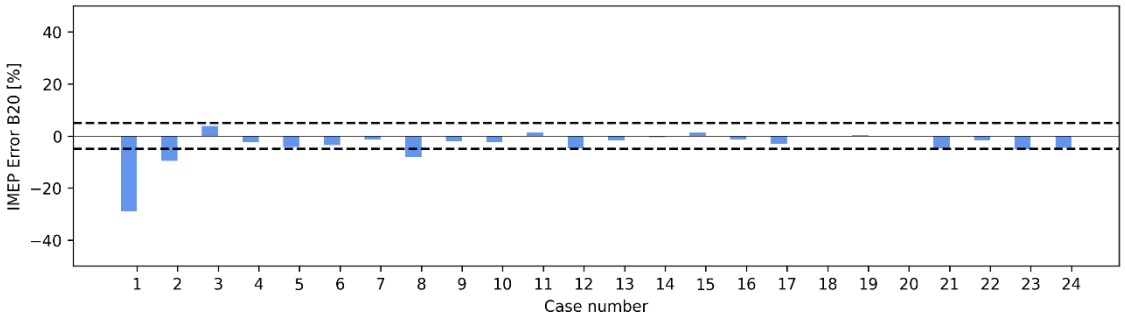

Figure 45. IMEP error, B20 fuel-DISRM.

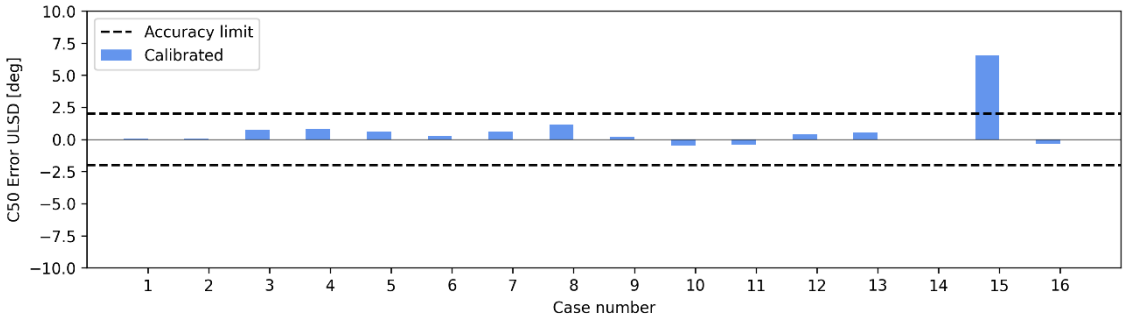

Figure 46. CA50 error, ULSD fuel - DISRM.

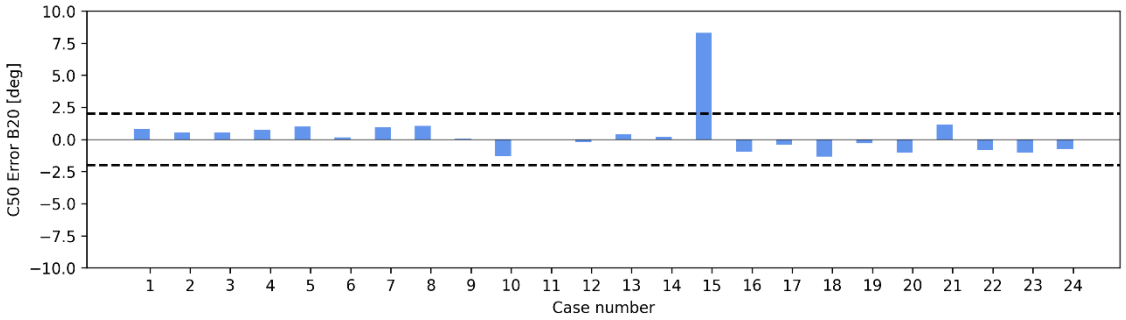

Figure 47. CA50 error, B20 fuel - DISRM.

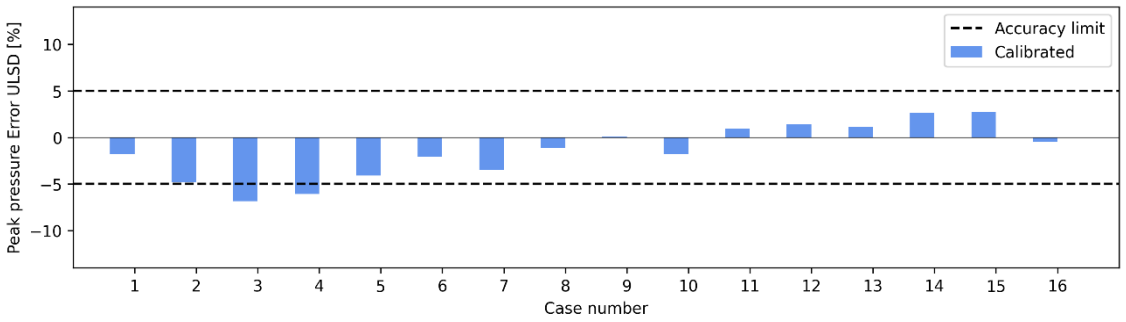

Figure 48. Peak pressure error, ULSD fuel - DISRM.

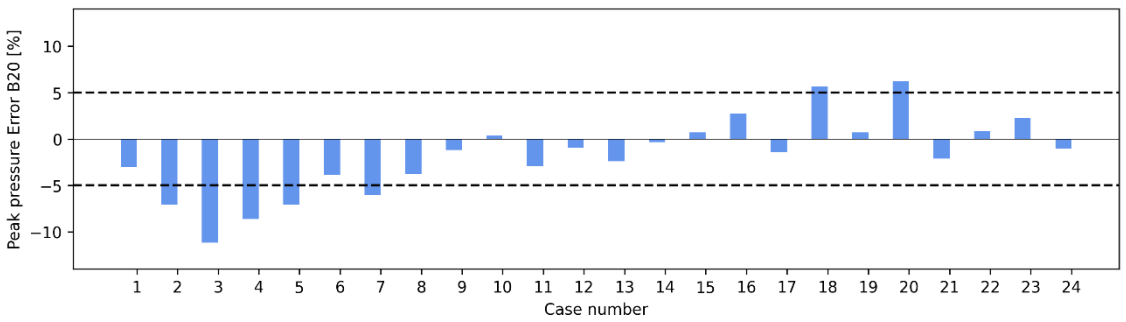

Figure 49. Peak pressure error, B20 fuel - DISRM.

Figure 50 and ***Figure 51*** shows the difference between computed and measured CO_2 emissions for ULSD and B20, respectively. The maximum absolute error was less than 38% for ULSD, with only three cases exceeding the accuracy limit. B20, on the other hand, exhibited higher discrepancies, with six cases exceeding the limit and a maximum error of 33.8%.

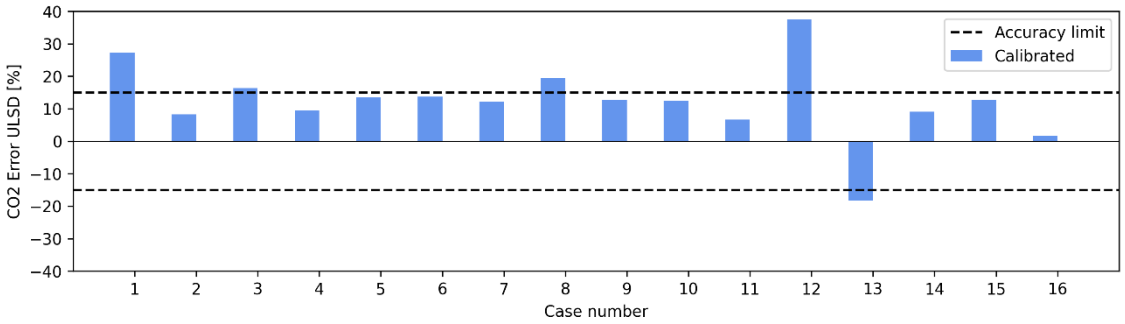

Figure 50. CO2 error, ULSD fuel - DISRM.

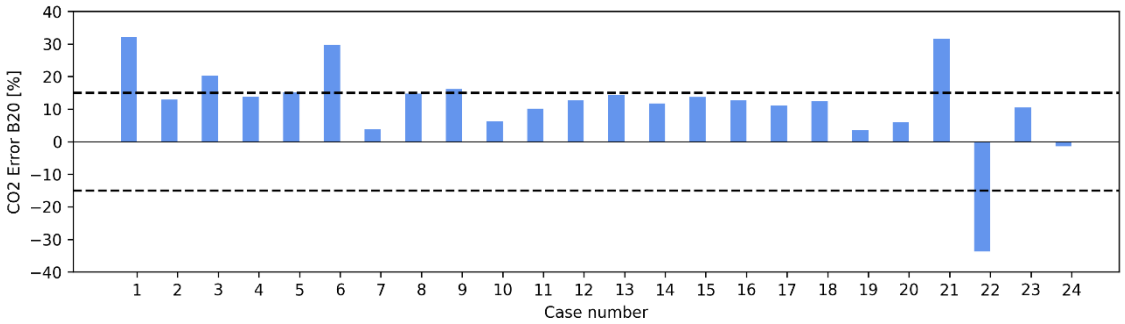

Figure 51.CO2 error, B20 fuel - DISRM.

Although most of the cases fall within the NOx emissions accuracy limits, there is a significant increase in the number of cases of both fuels exceeding those limits (Figure 52 and Figure 53). It is worth noting that better results were achieved in medium speeds (1200 to 2500 rpm) and loads from 1 to 4 bar, predicting NOx emissions in conditions outside of this range being challenging.

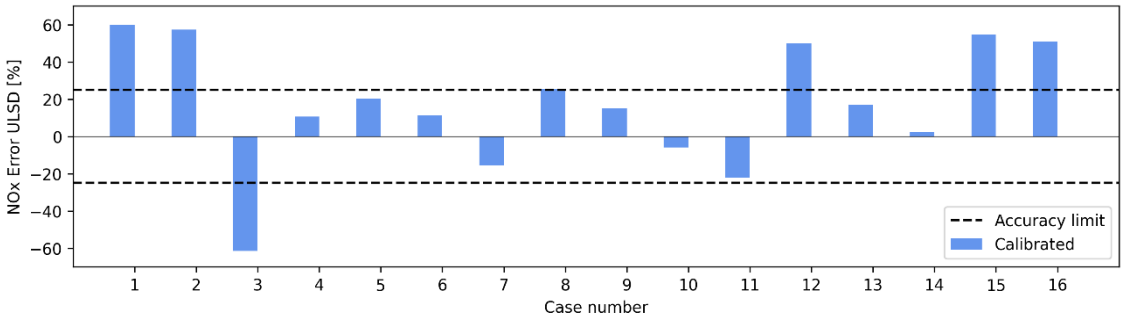

Figure 52. NOx error, ULSD fuel - DISRM.

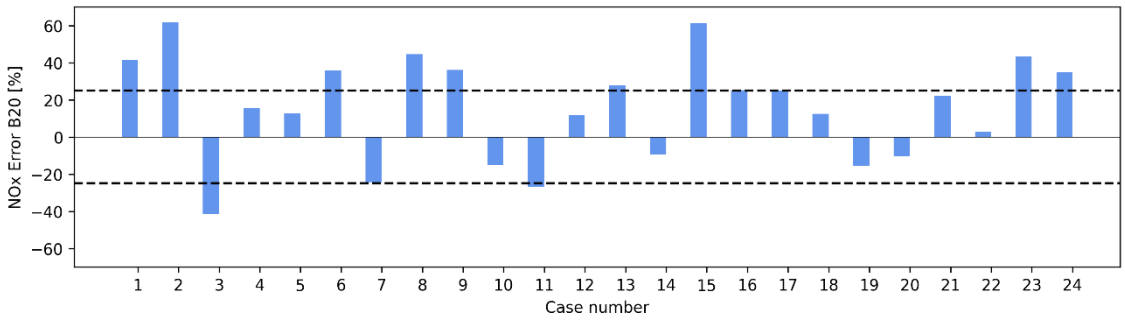

Figure 53. NOx error, B20 fuel - DISRM.

DISRM shows similar errors to the DI pulse model (see ***Figure 20*** - ***Figure 25***) in IMEP, CA50 and peak pressure, with most cases within accuracy limits, suggesting a robust capability in combustion prediction for DISRM calibrated combustion models. However, higher discrepancies in CO_2 and NOx emissions for B20 presented in this model highlight the challenges associated with modeling biodiesel blends. The complexities introduced by the presence of biodiesel components, with different ignition properties and combustion behavior, may make accurate predictions more demanding.

Due to the high computational requirements, the construction of the emissions map with the DISRM model was done from the simplified single-cylinder engine model under CPOA approach, which considers only the closed cycle (between the closing of the intake valve and the opening of the exhaust valve). However, it required certain additional input parameters such as air flow, volumetric efficiency, and cylinder wall temperature, which were taken from the results of the full engine model simulated with DI-Pulse. The simplified one-cylinder model with DISRM was used to obtain unregulated emissions.

3.4 Engine simulation results with biodiesel/diesel and HVO/diesel blends

This section presents the simulated results for ULSD, B20, and HV20 fuels, comparing several performance parameters and emissions. Performance parameters and regulated emissions were taken from the DI pulse model due to the better accuracy in NOx and CO_2 prediction shown in the model validation process. In addition, HC, CO and PN were included in this discussion, while unregulated emissions (PAH, Carbonyls, Benzene, Toluene) were computed from DISRM results, because unregulated species only can be predicted from the DISRM model.

3.4.1 Engine performance

Figure *54* (a) shows the simulated brake thermal efficiency (BTE) for ULSD as a function of engine speed and load. **Figure *54*** (b) and (c) illustrate the impact of biodiesel and HVO blends, respectively, expressed as a percentage change compared to ULSD. Positive values indicate an increase in BTE due to the addition of biodiesel or HVO, while negative values represent a decrease. An increase in engine load resulted in improved BTE. Higher loads typically allow the engine to operate closer to peak thermal efficiency, and also result in higher air-to-fuel ratios which can lead to more complete combustion. On the other hand, high speeds and low loads can lead to decreased BTE due to increased frictional losses, poor combustion due to short residence time and lower volumetric efficiency (***Figure 54***). B20 and HVO20 presented a slight increase for BTE, up to 4.3%, and 1% respectively. In biodiesel blends, this is attributed to the shorter ignition delays and higher oxygen contend leading to improved combustion efficiency [113], whereas, as discussed in [45], HVO offers a slightly higher thermal efficiency because of the higher cetane number, and, therefore, shorter ignition delay.

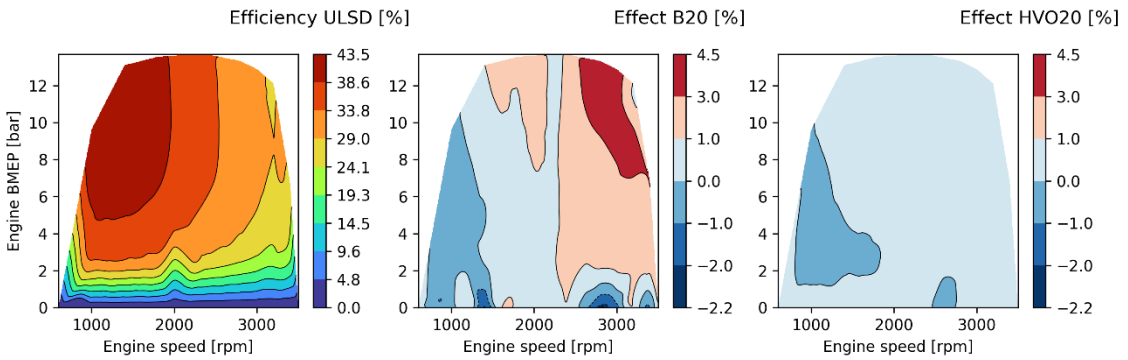

(a) (b) (c)

Figure 54. Simulated Brake Thermal Efficiency (a) ULSD, (b) B20 effect, (c) HVO20 effect.

Figure *55* shows the simulated brake specific fuel consumption (BSFC). A high correlation with BTE is observed: lower BSFC are located at the same speed and load conditions as the higher BTE. Higher speeds and lower loads resulted in higher BSFC, a trend previously reported in literature [38], [45]. B20 and HVO20 caused a slight increase and decrease of BSFC due to their higher and lower energy density, respectively.

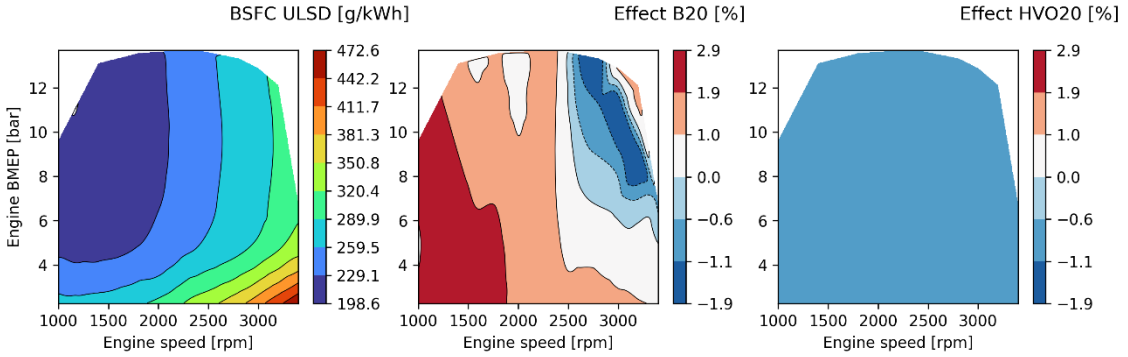

(a) (b) (c)

Figure 55. Simulated Brake Specific Fuel Consumption (a) ULSD, (b) B20 effect, (c) HVO20 effect.

Figure *56* shows the simulated volumetric efficiency (VE). No significant differences were found between the three fuels. As engine speed increases, the time available for the intake and exhaust processes decreases, reducing volumetric efficiency. Increasing the load generally enhances volumetric efficiency because the higher air demands are met by the engine by drawing in larger volumes of air. However, higher loads also result in higher temperatures, which decreases the density of the fresh charge in the cylinder, having a negative impact on VE [27].

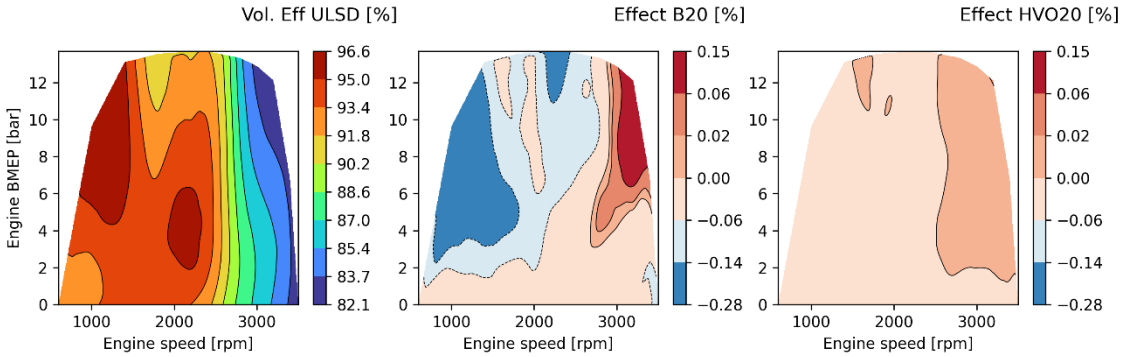

(a) (b) (c)

Figure 56. Simulated Volumetric Efficiency (a) ULSD, (b) B20 effect, (c) HVO20 effect.

Figure *57* displays the simulated mechanical efficiency (ηm). While the friction model used in this study is too simplistic to capture the specific effects of biodiesel and HVO on mechanical efficiency, existing literature suggests these effects can be attributed to their contrasting lubricity properties [45], [114].

Biodiesel generally exhibits better lubricity compared to conventional diesel, due to its inherent oxygen content. This translates to reduced friction between engine components like piston rings and cylinder walls, potentially leading to improved mechanical efficiency. Conversely, HVO fuels typically possess very low lubricity due to the absence of sulfur and oxygen compounds. This characteristic can contribute to decreased mechanical efficiency in some cases.

However, the dominant factor influencing ηm in this simulation appears to be engine speed and load. As expected, ηm decreases at higher speeds due to increased frictional losses within the engine. In contrast, higher loads often lead to improved combustion efficiency, resulting in a greater portion of the generated energy contributing directly to useful work and consequently, higher mechanical efficiency.

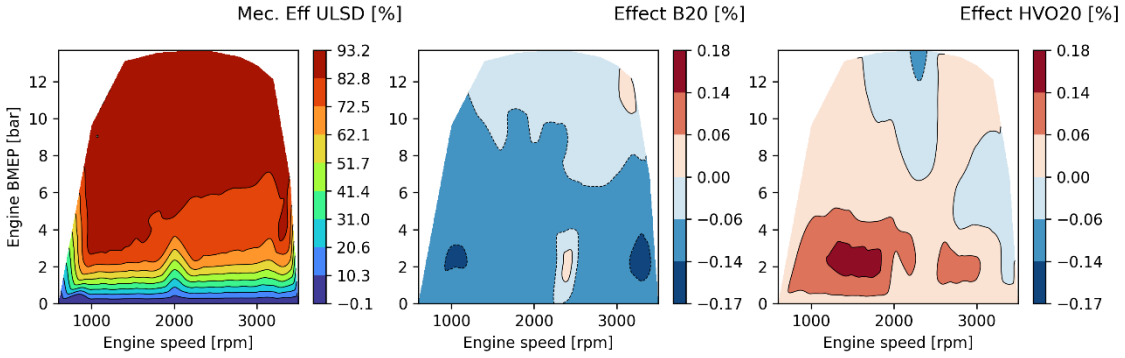

(a) (b) (c)

Figure 57. Simulated Mechanical efficiency (a) ULSD, (b) B20 effect, (c) HVO20 effect.

3.4.2 Regulated emissions

CO_2 emissions

Figure *58* shows the simulated CO_2 emission maps for ULSD as a function of engine speed and load and the impact of BD and HVO blends, expressed as a percentage change compared to ULSD. Higher engine speeds and loads lead to increased CO_2 emissions due to the higher fuel consumption required to produce the necessary power output. While the combustion process may be more efficient due to improved air-fuel ratio, the overall fuel consumption increases, leading to higher CO_2 emissions [115], [116]. B20 leads to a slight maximum increase of 1.35% at speeds lower than 1500 rpm and loads between 4 and 10 bar. Such increase in CO_2 has been attributed to a higher oxygen content, which enhances the oxidation of CO to CO_2 [117]. At higher speeds, there is a reduction in CO_2 emissions of up to 2.11%. This decrease might be correlated with the slight improvement in BTE and slight reduction in BSFC observed with B20 under these conditions (**Figure *54*** and **Figure *55***).

A small reduction in CO_2 emissions of up to 1.35% is observed with HVO20, which has been ascribed to the lower fuel consumption due to the higher LHV of HVO [45]. Additionally, the lower carbon content of HVO (resulting in a higher H/C ratio), which is a consequence of the lighter hydrocarbon compounds in HVO compared to conventional diesel, further contributes to the reduction in CO_2 emissions. The trends of HVO's effect on CO_2 emissions are not clearly discernible due to the map scaling.

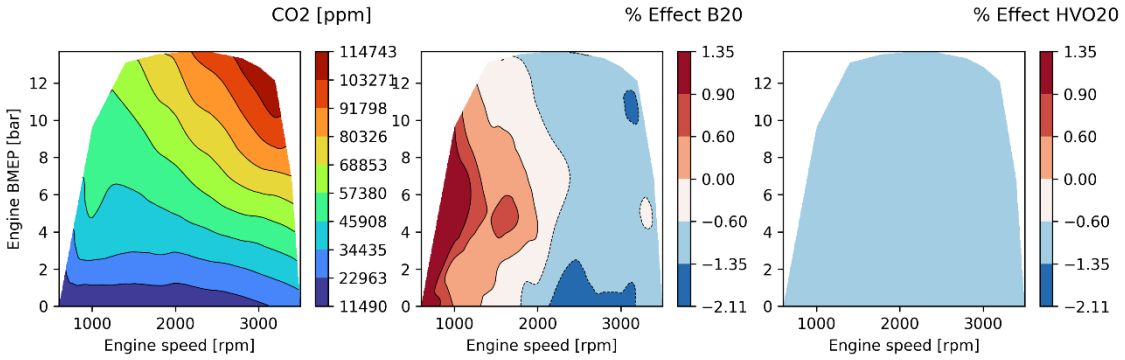

(a) (b) (c)

Figure 58. Simulated CO2 emissions (a) ULSD, (b) B20 effect, (c) HVO20 effect.

NOx emissions

Figure *59* shows the simulated NOx emission map for ULSD. An increase in emissions occurs at mid-range engine speeds (around 2000 rpm) combined with high loads. Under these conditions, the combination of high temperatures with residence times long enough to allow the nitrogen oxidation reactions to proceed favors the formation of these pollutants [118], [119].

NOx emissions increase by 1-20% for B20 for almost all operating conditions (Figure 57 (b)). However, a slight decrease of 1-3.7 % is evidenced at loads below 2 bar and speeds up to 2000 rpm. The increase in NOx with the use of B20 has been attributed to the increased in-cylinder temperatures during combustion and the higher oxygen content in biodiesel molecules [118],

[115]. On the other hand, in HVO NOx tends to decrease up to 3.7% at speeds lower than 2000 rpm and increase up to 1% at speeds higher than 2000 rpm (Figure 57 (c)), in agreement with [45] who reported that the effect of HVO on NOx emissions depends on the engine speed and load. Furthermore, although the higher cetane number of HVO decreases the ignition delay and can promote the formation of NOx by anticipating the increases in pressure and temperature, the absence of oxygen and aromatics in such fuel decreases the emission of NOx, due to the reduction of the adiabatic flame temperature, resulting in lower local combustion temperatures. However, it is valuable to mention that the absence of EGR may limit the observed HVO benefits on NOx reduction [120], and further investigation with EGR is recommended for more conclusive results.

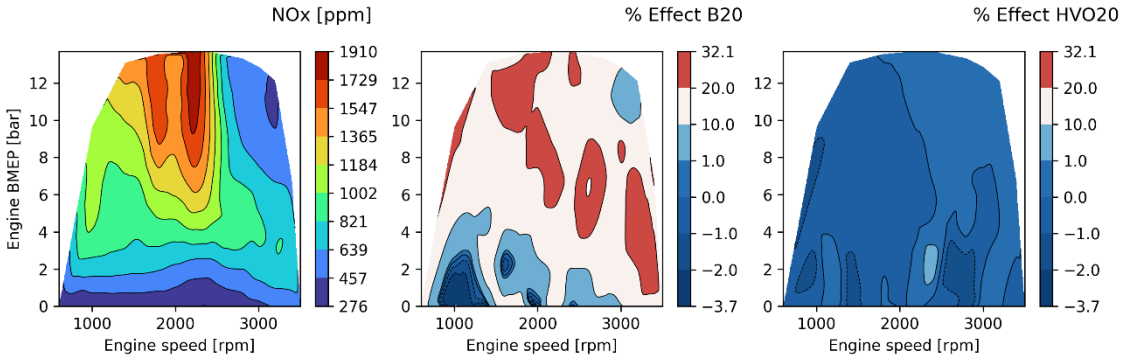

(a) (b) (c)

Figure 59. Simulated NOx emissions (a) ULSD, (b) B20 effect, (c) HVO20 effect.

CO and HC emissions

Figure *60* and Figure 61 show the simulated HC and CO emission maps, respectively, for ULSD. Higher HC and CO emissions were observed at higher speeds and loads due to higher fuel requirements and less efficient combustion [121]. B20 had a significant impact on HC emissions, reducing them by 31.6% at all speeds and loads below 6 bar, and by up to 70.2% in regions between 8 to 14 bar of load. Similarly, HVO20 contributed to reduced HC emissions across most operating conditions, achieving reductions of up to 8.4%. Regarding CO emissions, B20 demonstrated a marginal decrease (up to 5.44%) at high speeds and loads but showed an increase of up to 3.52% at lower speeds and moderate loads. Conversely, HVO led to a reduction in CO emissions of up to 2% across various operational conditions, with the maximum reduction of 5.44% observed at speeds exceeding 2500 rpm. The reduction of HC and CO with BD and HVO has been reported in the literature [45], [114], and is a consequence of shorter ignition delay [122] which results in higher temperatures favoring the oxidation of CO and HC species. In addition, higher oxygen content in BD enhances the combustion process.

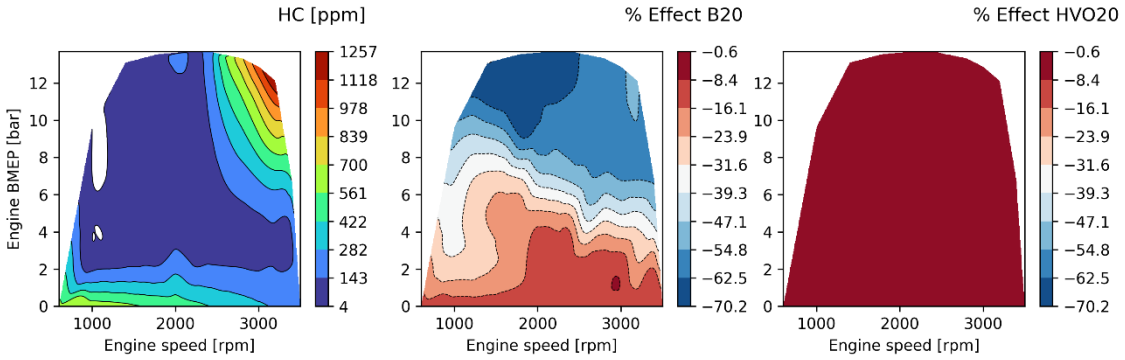

(a) (b) (c)

Figure 60. Simulated HC emissions (a) ULSD, (b) B20 effect, (c) HVO20 effect.

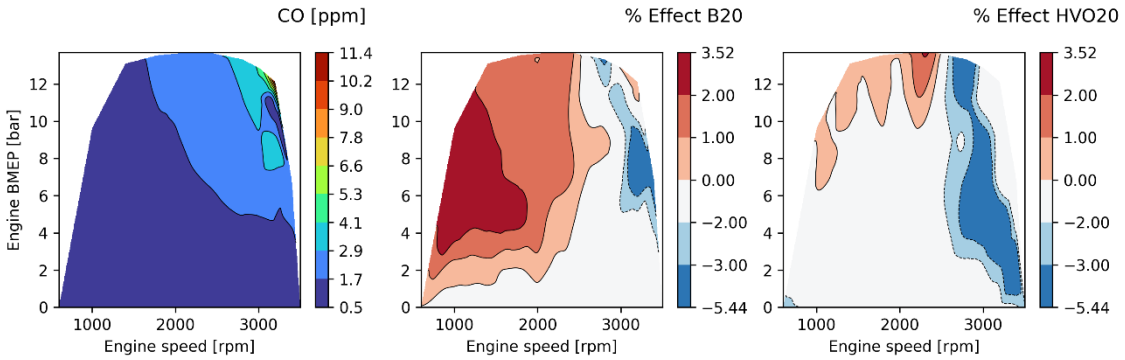

(a) (b) (c)

Figure 61. Simulated CO emissions (a) ULSD, (b) B20 effect, (c) HVO20 effect.

3.4.3 Unregulated emissions

PAH emissions

The merged mechanism describes the PAH formation process up to pyrene (A4), including naphthalene (A2) and phenanthrene (A3). **Figure *62*** to Figure 64 shows the simulated PAH emissions maps for ULSD, and the effect of BD and HVO on these emissions. A3 and A4 follow similar trends to CO emissions. Higher engine speeds lead to an increase in A3 and A4 emissions, possibly due to incomplete combustion at lower residence times; a similar effect of speed on A3 and A4 emissions was reported in [123]. Increasing loads, on the other hand, may increase A3 and A4 emissions due to increased fuel demand. A2 showed opposite trends, with higher concentrations at low speeds and loads. The decrease in A2 emissions at high loads would be the result of the higher decomposition rate of these species due to a high in-cylinder temperature[124]. Higher concentrations of A4 with respect to A2 and A3 were found, accounting for 98% of total PAH in most of the operation range. According to [125], A2 is the most abundant PAH during the engine combustion process, accounting for 26–84% of PAHs on gas phase. The unexpected dominance of A4 might suggest an "accumulation" effect, potentially due to the absence of a soot nucleation model or other gas-phase reactions converting A4 into larger species. Despite these discrepancies, further refinement of the merged mechanism and engine model is advisable.

Although the simulated PAH distribution was not the expected, the effects of BD on PAH emissions were generally consistent with other studies [43], [126], [127]. Biodiesel reduced A4 emissions by up to 60% for almost all speed and load combinations, whereas A3 and A2 are reduced by up to 100%. The lower PAH emissions with biodiesel has been attributed to oxygen enrichment and lower content of PAH precursors in biodiesel, which enhances fuel combustion and reduces PAH formation [43], [126], [127]. HVO use decreases PAH up to 50% in a wide operation range, with reductions up to 55% reported in literature [59]. The use of HVO decreased PAH by up to 50% over a wide operating range. Some researchers [128], [129] suggested that PAH emissions are greatly influenced by the PAH content in the fuel, which is reduced by the addition of HVO. As A4 comprised 98% of the total PAHs simulated, the PAH distribution maps for ULSD and the effects of BD20 and HVO20 displayed a similar trend.

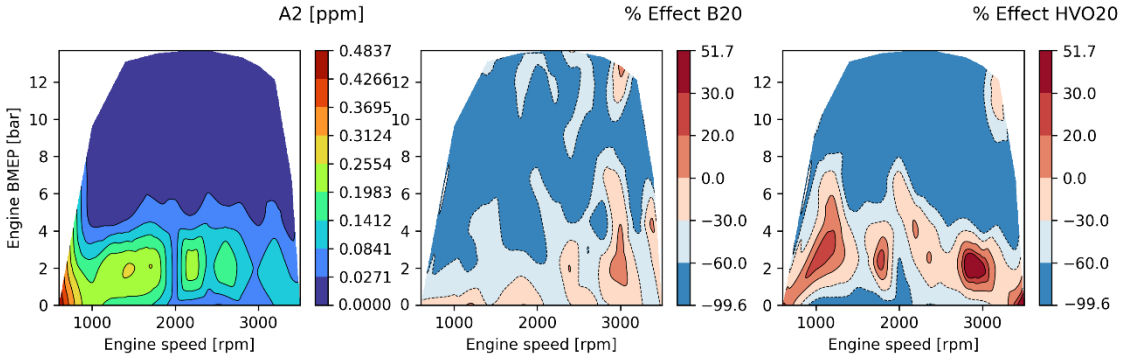

(a) (b) (c)

Figure 62. Simulated naphthalene (A2) emissions (a) ULSD, (b) B20 effect, (c) HVO20 effect.

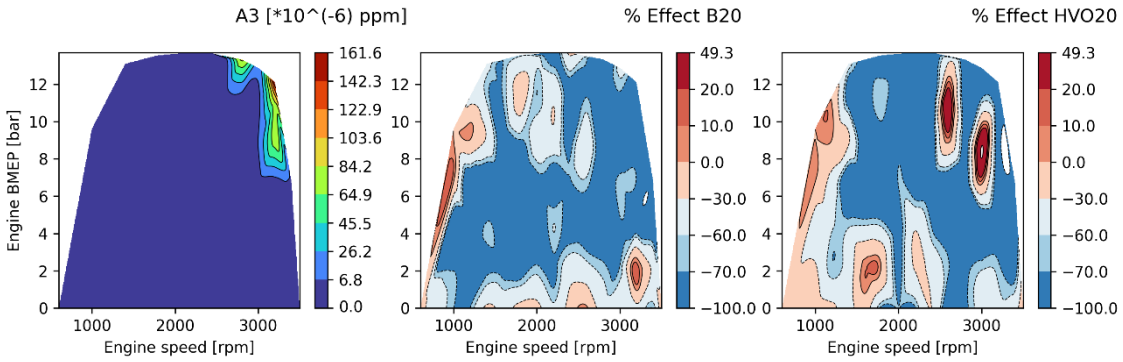

(a) (b) (c)

Figure 63. Simulated phenanthrene (A3) emissions (a) ULSD, (b) B20 effect, (c) HVO20 effect.

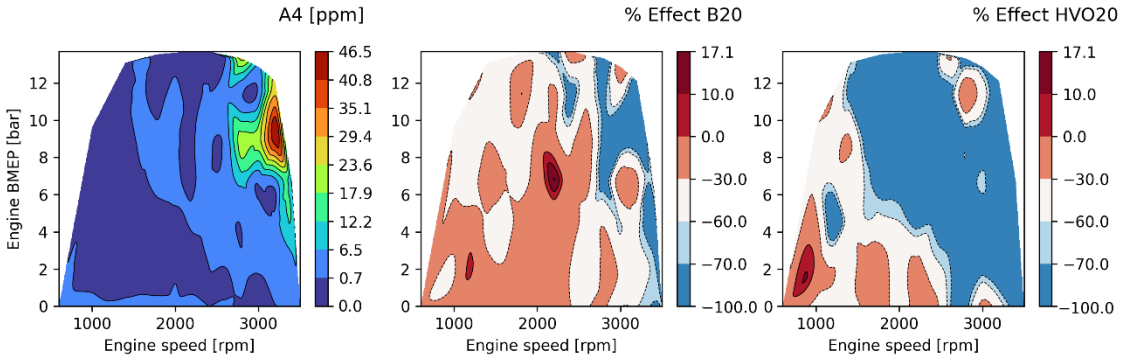

(a) (b) (c)

Figure 64. Simulated pyrene (A4) emissions (a) ULSD, (b) B20 effect, (c) HVO20 effect.

Aromatic Hydrocarbons (Benzene-Toluene BT)

Benzene emissions tend to increase at lower loads and speeds in ULSD, with the highest concentrations at idle speed (**Figure *65*** (a)), a trend already reported in literature [130]. An increase in Toluene is also observed, but the highest concentrations were reached at speeds between 2000 and 2500 rpm (**Figure *66*** (a)). The overall decrease in BT (Benzene, Toluene) emissions with increasing engine load has been attributed to the oxidation of BT emissions at higher temperatures [131].

B20 (**Figure *65*** (b)) and HVO20 (**Figure *65*** (c)) reduced benzene emissions by up to 50% across the entire speed range and for loads below 6 bar, and by 50 to 100% for the rest of the operating range. The positive impact of BD and HVO on benzene reduction tends to amplify with increasing load, mirroring the behavior observed for HC emissions. However, specific conditions of speed and load also led to increases of up to 31.7% for both blends. Conversely, toluene emissions decreased with the use of B20 and HVO20, with reductions of up to 50% noted for loads up to 8 bar (**Figure *66*** (b) and (c)). Despite these favorable reductions, a clear trend in the effect of BD and HVO was not distinctly evident.

There is no consensus for benzene variation with Biodiesel [130]: several authors have reported an increase up to 23% and others a decrease up to 71% [6]. According to [131], there are two factors that explain this behavior on benzene emissions, when adding biodiesel: a reduction in exhaust temperature slows down the oxidation of benzene, while oxygen enrichment in the fuel drives the oxidation of benzene precursors. The influence of exhaust temperature could override the influence of oxygen enrichment, leading to an increase in benzene emissions with increasing biodiesel use. However, toluene emissions have been reported to decrease when increasing biodiesel use, suggesting that oxygen enrichment is more dominant for the reduction of these two pollutants [6]. There are no reports on the effect of HVO on BT emissions. However, the improved combustion characteristics and the absence of aromatic compounds in HVO may be two key factors promoting the reduction of these emissions.

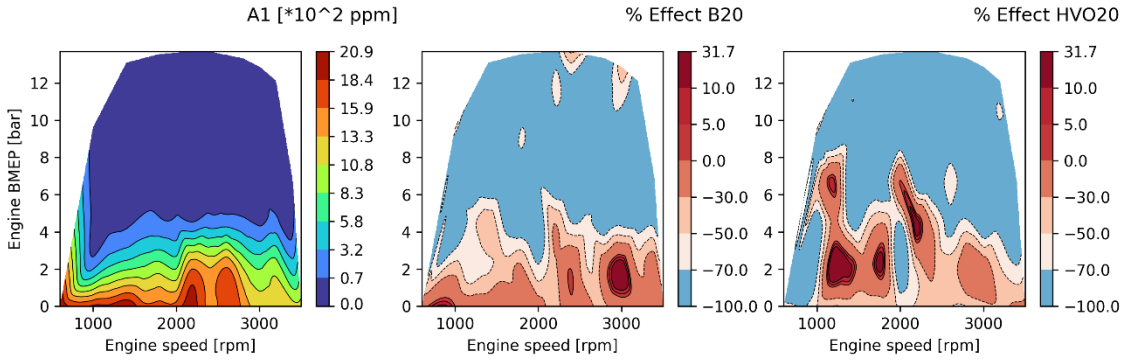

(a) (b) (c)

Figure 65. Simulated Benzene emissions (a) ULSD, (b) B20 effect, (c) HVO20 effect.

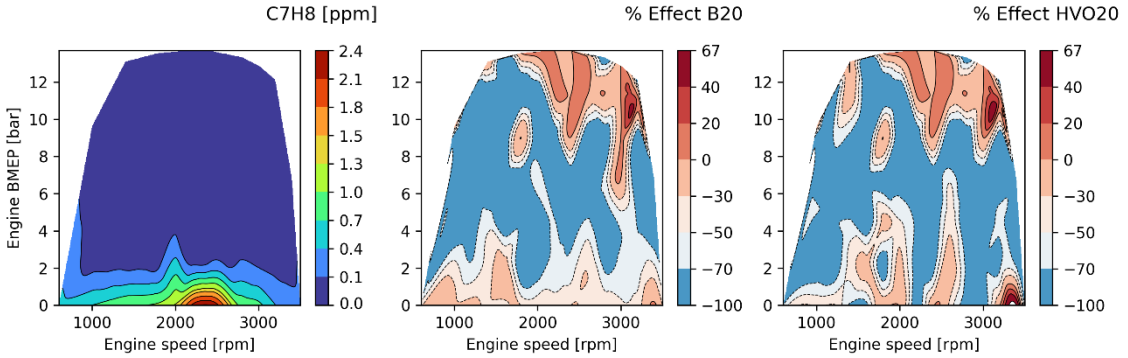

(a) (b) (c)

Figure 66. Simulated Toluene emissions (a) ULSD, (b) B20 effect, (c) HV20 effect.

Carbonyl emissions (Formaldehyde)

Figure *67* shows the simulated formaldehyde emission maps for ULSD, and the effect of BD and HVO additions on these emissions. With ULSD, formaldehyde emissions tend to decrease with increasing load, and a slight increase is observed from idle speed to 2000 rpm followed by a decrease from 2000 to 3500 rpm. This trend has been attributed to the high in-cylinder temperature at higher speeds and loads leading to a reduction in formaldehyde emissions [131].

BD leads to an increase in formaldehyde emissions by up to 30% at certain speed regions and loads below 1 bar, by 30 to 159.8% at speeds from 2000 to 3500 rpm and loads from 6 to 13 bar. Additionally, formaldehyde emissions also decrease by up to 30% at speeds lower than 2700 rpm and loads from 1 to 5 bar. According to [6] several authors reported a general trend of increase in the emissions of these species with the use of biodiesel and its blends. Higher acetaldehyde emissions resulted from synergistic effects of fuel oxygen content and short-chain hydrocarbons (i.e., methyl esters) that helps forming short-chain carbonyl compounds [131]. However, other authors reported that biodiesels either help reduce carbonyl emissions or no significant differences between test fuels were found [6]. These conflicting results may be due to variations in the chemical composition of biodiesels, the test engine and experimental methods used, and engine operating conditions [6]. Regarding HVO effect on these emissions, most of the speeds and load combinations lead to reduction by 30 to 100%, possibly because the lack of aromatics in HVO

fuel reduces intermediate compounds during combustion [59]. Thus, formaldehyde emissions were significantly reduced with HVO.

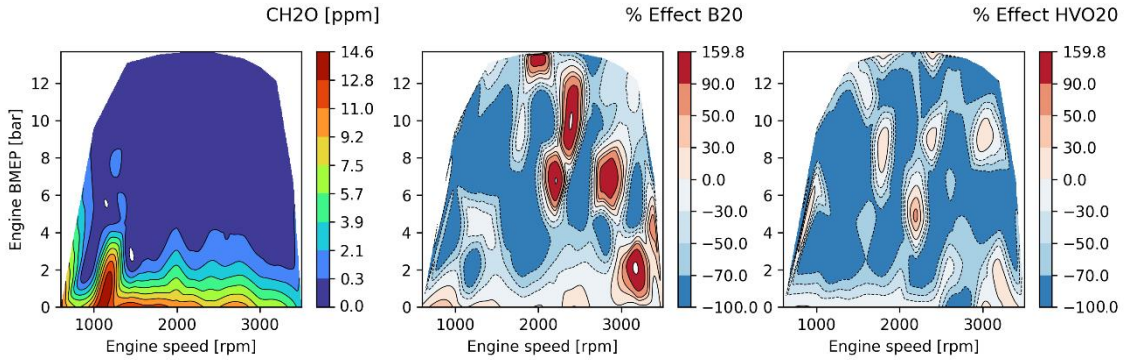

(a) (b) (c)

Figure 67. Simulated formaldehyde emissions (a) ULSD, (b) B20 effect, (c) HV20 effect.

PN emissions

Figure *68* shows the simulated particulate number (PN) emission maps for ULSD, and the effect of adding BD and HVO on these emissions. PN emissions showed similar trends to A3 and A4 emissions, which are precursors of soot formation [43], [132]. The increase in PN at higher loads and speeds may be influenced by fuel demand and reduced residence time in the combustion chamber, which can result in incomplete combustion.

B20 resulted in the lowest PN emission, with a decrease of 5 to 37% at most speed and load conditions and up to 47% in certain points, in agreement with the reported 41.9% reduction using B20 fuel [126]. Several factors have been attributed to the lower PN emission from B20, including the oxygen enrichment and reduced carbon content of biodiesel, which accelerate the oxidation of primary particles. Additionally, the higher cetane number of biodiesel compared to diesel shortens the ignition delay and elongates the duration of mixing-controlled combustion, favoring soot oxidation. The absence of aromatics in biodiesel is also a key factor for the lower PN emission [6], [7], [10], [133]. HVO20 showed a slight reduction up to 5%, but there is no definitive conclusion of the HVO effect on PN emissions in literature, [134] [135] reporting slight increase and decrease of PN, depending on the operation mode.

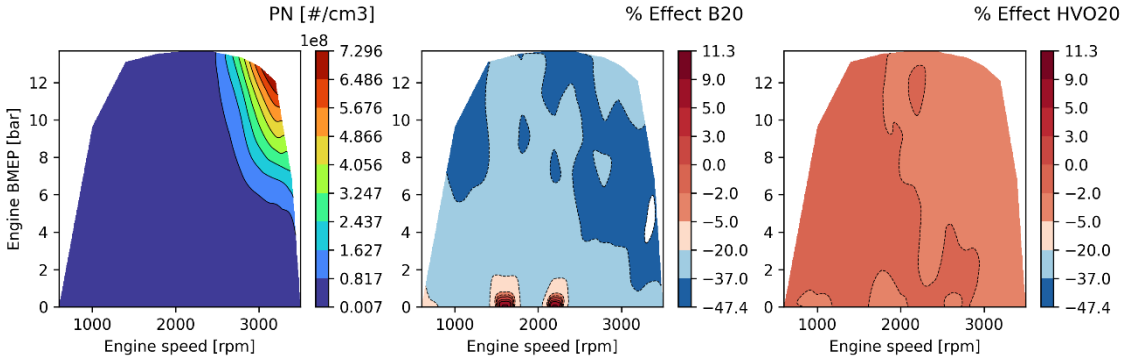

(a) (b) (c)

Figure 68. Simulated PN emissions (a) ULSD, (b) B20 effect, (c) HVO20 effect.

In general, a reasonable correlation was observed between simulated and literature trends in emissions and performance parameters. The effects of speed and load on these parameters were well-predicted. Furthermore, the addition of BD and HVO to diesel led to the expected reduction or increase in most of the variables evaluated. Thus, simulated engine maps were used in the vehicle model to assess the impact of the BD and HVO under global and local driving cycles. The following section shows the vehicle simulation results.

3.5 Vehicle model

3.5.1 Model Validation

Figure *69* displays the target and actual vehicle speeds for each simulated driving cycle when fueled with ULSD. Nearly identical results were observed for B20 and ULSD. The model successfully replicated all driving cycles, with no discernible differences between target and actual speeds. To quantify the model's accuracy in following the driving cycles, the correlation coefficients (R) and coefficients of determination (R^2) (refer to **Table *26***) were estimated. The coefficients for all driving cycles and fuel types demonstrate excellent agreement between target and actual speeds, with all values exceeding 0.999.

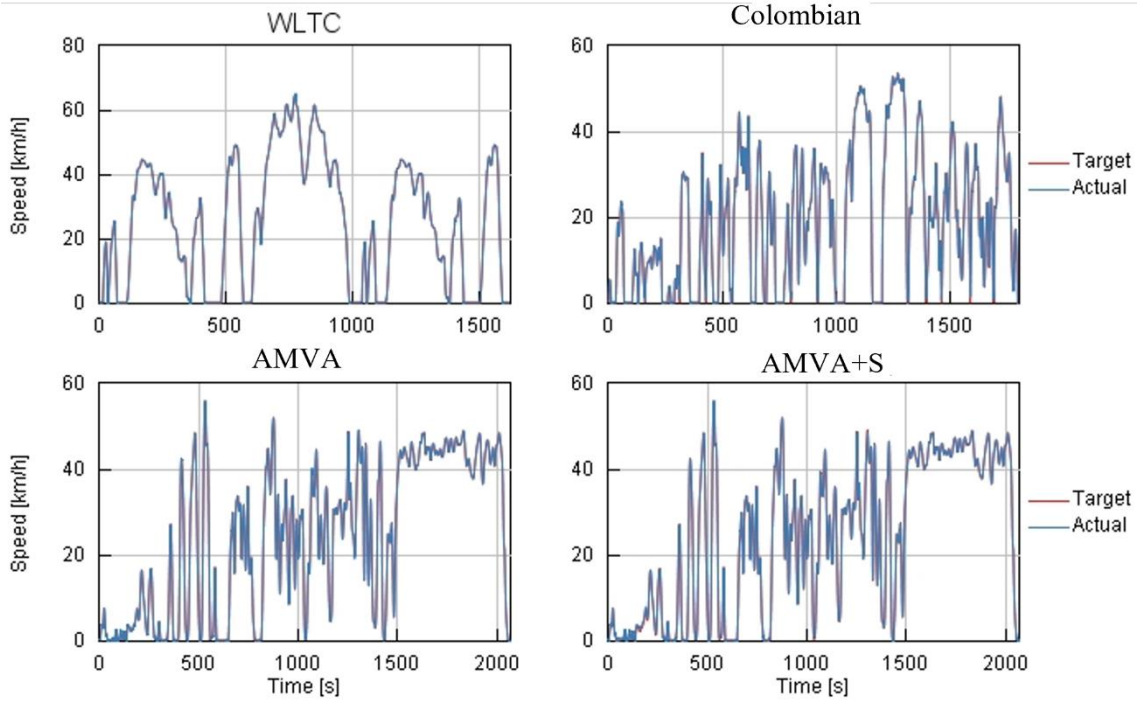

Figure 69. Target and actual vehicle speeds for each simulated driving cycle. ULSD as fuel. AMVA+S stands for the Andean cycle with slope.

Table 26. Correlation (R) and Determination (R2) coefficients for all driving cycles with both fuels, ULSD and B20.

	ULSD		B20		HVO20	
	R	R^2	R	R^2	R	R^2
WLTC	0,9998	0,9996	0,9998	0,9996	0,9998	0,9996
Andean 1	0,9992	0,9983	0,9992	0,9983	0,9992	0,9983
Andean 2	0,9995	0,9991	0,9995	0,9991	0,9995	0,9991
Andean 2 with slope	0,9995	0,9990	0,9995	0,9990	0,9995	0,9990

Figure *70* and **Figure *71*** compare experimental and simulated emission factors and fuel consumption for NOx and CO_2 using the WLTC Class 1 cycle and NBR gear-shifting strategy. The results of the DISRM-based vehicle model are also included in order to assess the accuracy of NOx and CO_2 emissions predicted by this combustion model. The DI-pulse-based vehicle model shows good agreement with experimental NOx values, with errors below 11% for all tested fuels. The simulated and experimental NOx emission factors for B20 showed a slight increase, of 0.1% and 1.3%, respectively. HVO20 also led to an increase in experimental and predicted NOx emissions, 4.8% and 1.2%, respectively. These results agree with literature, which shows that BD generally increases NOx emissions from 0.4% to 8%, depending on the feedstock source, biodiesel content and driving conditions [9], [10], [7], while NOx emissions with HVO depend on the engine speed and load [44]. The DISRM-based vehicle model leads to higher errors in NOx emissions, up to 26%.

B20 leads to different trends for experimental and simulated CO_2 emission factors for both combustion models, namely, a 28% increase found experimentally while slight reductions of 0.3% and 1.8% for DI-Pulse and DISRM, respectively. The simulated CO_2 emission factor showed similar results to other experimental studies [9], [10], [136], with marginal differences between 1% and 4%, and even considered identical in [7].

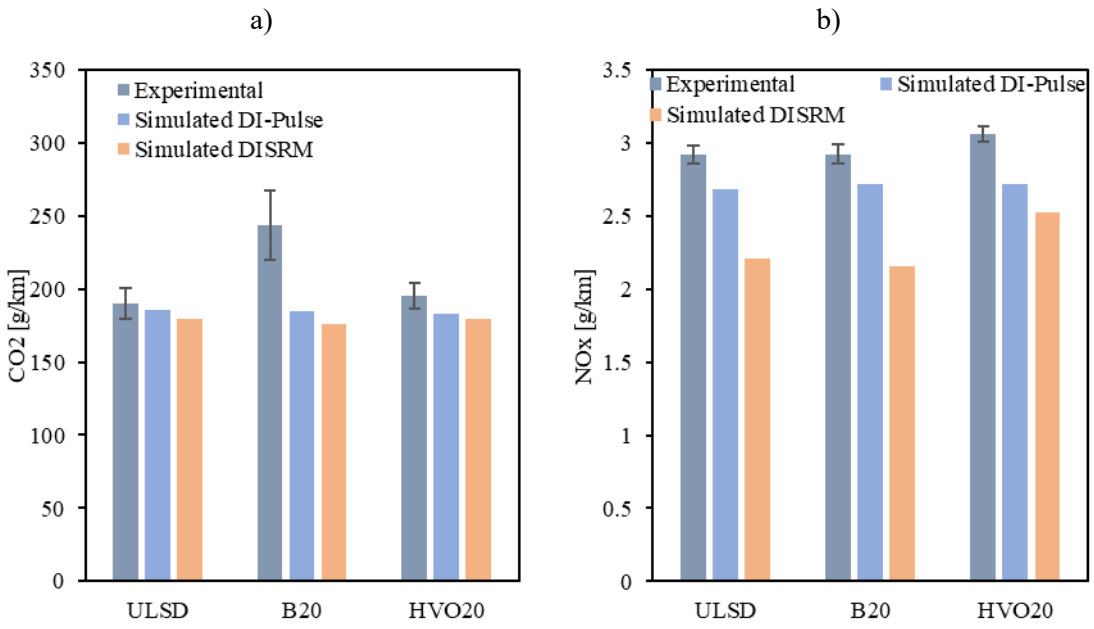

c)

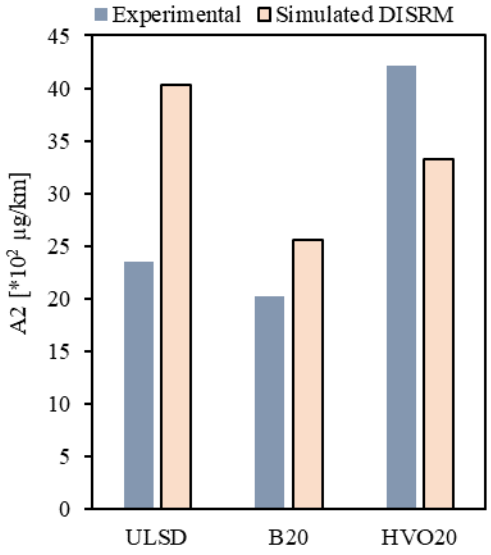
Experimental
Simulated DISRM
A2 [*10² µg/km]
45
40
35
30
25
20
15
10
5
0
ULSD
B20
HVO20

d)

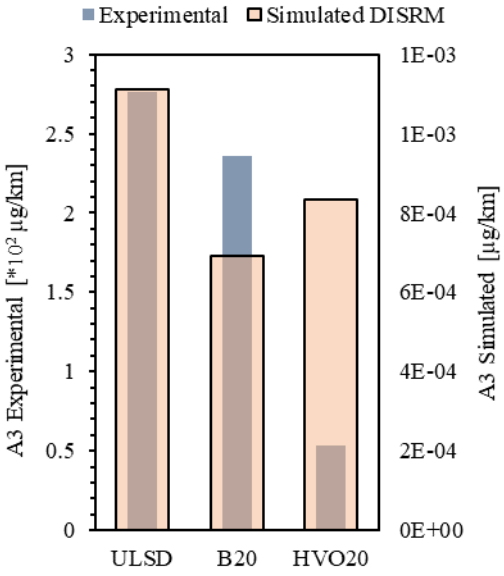
Experimental
Simulated DISRM
A3 Experimental [*10² µg/km]
A3 Simulated [µg/km]
3
2.5
2
1.5
1
0.5
0
1E-03
1E-03
8E-04
6E-04
4E-04
2E-04
0E+00
ULSD
B20
HVO20

e)

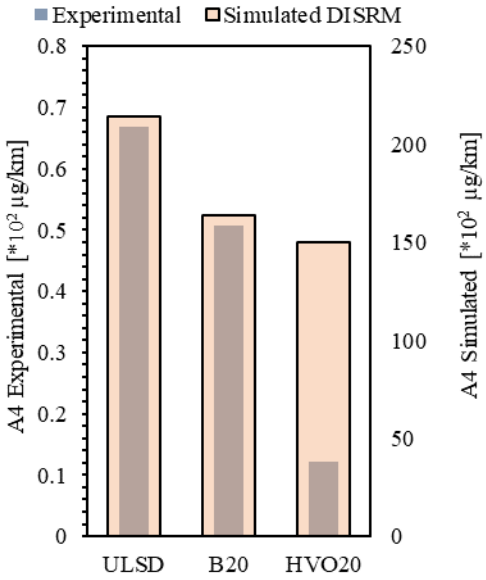
Experimental
Simulated DISRM
A4 Experimental [*10² µg/km]
A4 Simulated [*10² µg/km]
0.8
0.7
0.6
0.5
0.4
0.3
0.2
0.1
0
250
200
150
100
50
0
ULSD
B20
HVO20

f)

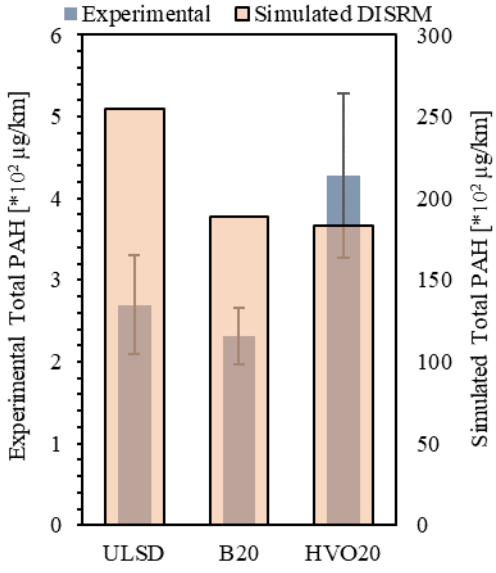
Experimental
Simulated DISRM
Experimental Total PAH [*10² µg/km]
Simulated Total PAH [*10² µg/km]
6
5
4
3
2
1
0
300
250
200
150
100
50
0
ULSD
B20
HVO20

g)

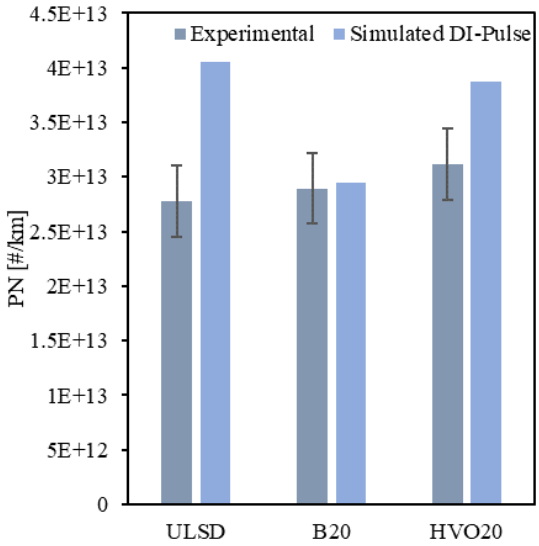

Figure 70. Experimental and simulated emission factors for WLTC Class 1 cycle. Error bars correspond to the standard deviation. a) CO_2, b) NOx, c) A2, d) A3, e) A4, f) Total PAHs, g) PN

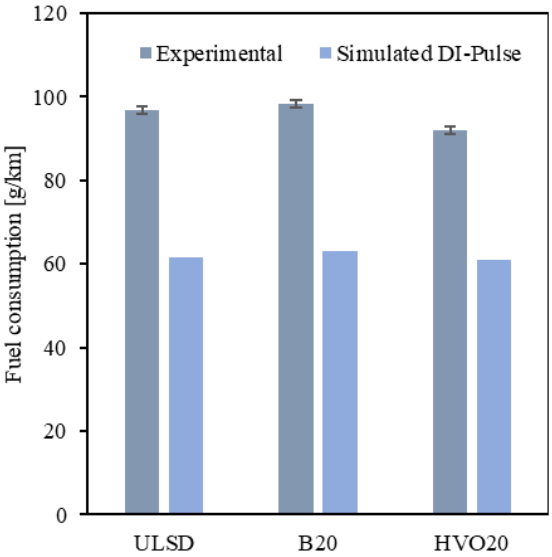

Figure 71. Experimental and simulated fuel consumption for WLTC Class 1 cycle. Error bars correspond to the standard deviation.

Larger differences were found between experimental and simulated PAH emissions. This is not surprising, as the predicted emissions are for in-cylinder conditions at exhaust valve opening, the model not considering the effect of DOC or events and reactions in the exhaust system occurring after the gases have left the cylinder, which may strongly affect PAH emissions [137]. To accurately model PAH emissions, more sophisticated models are needed that consider the entire emissions pathway, including post-combustion effects and exhaust system phenomena to better represent experimental data. Moreover, as mentioned before, unexpected higher simulated concentrations of A4 with respect to A2 and A3 were found, accounting for 98% of total PAH, while measured A2 corresponds to the 77, 76 and 96% for ULSD, B20 and HVO20, respectively, of the total PAH, in agreement with [125] who found A2 to be the most abundant PAH during the engine combustion process (accounting for 26–84% of PAHs). However, despite the larger

differences in magnitude, the model showed reasonable agreement with the BD effect exhibited in the experiments, decreasing PAH emissions compared to ULSD. On the other hand, experimental tests showed an increase in A2 and a decrease of A3 and A4 emissions with the use of HVO20 compared to ULSD, in agreement with [138], who showed that total PAH emissions for HVO30 blend were slightly higher than diesel-biodiesel blends, especially the lighter PAHs. In contrast, emissions of the heaviest PAHs were generally lower than those of other tested fuels. Simulated A2 emissions in HVO were lower than in ULSD, which suggests that HVO20 effect on light PAHs is not properly captured but trends to reduce heaviest PAHs seems reasonable.

Significant differences were found for experimental and simulated fuel consumption with error up to 37%. However, simulated trends agree with experiments, with a slight increase and decrease for B20 and HVO20, respectively, consistent with their energy density.

Regarding PN emissions, B20 and HVO20 lead to increase PN by 4.3 and 12.3%, respectively, with respect to ULSD in experiments, while simulated emissions factors decrease by 27.2 and 4.6%, respectively. The large experimental uncertainty range does not allow to draw a conclusion on the effect on PN, but other studies have reported PN reductions with BD up to 41.9% [126]. On the other hand, there is no clear conclusion of the HVO effect on PN emissions: [134] and [135] reported slight increase and decrease of PN, depending on the operation mode.

In conclusion, vehicle models showed good accuracy for NOx and CO_2 emissions, but higher discrepancies were found in unregulated emissions, PN and fuel consumption. However, the effects of BD and HVO were well captured in most of the compared quantities, showing reasonable agreement with measured data and reported literature.

3.5.2 Vehicle model results

Figure *72* shows the combinations of engine speed and load required by the vehicle model to follow each driving cycle (DC). It can be seen that local DCs have a more scattered distribution of operating conditions (OC) and require, in general, higher loads than the WLTC; this dispersion in operating conditions within the local DCs can be attributed to their stop-and-go nature. Variability in engine operating conditions has important implications for emissions, as previously discussed. WLTC and AMVA driving cycles exhibit significant similarities in their operating conditions. Both cycles display a concentration of operating points in the mid-range of engine speed and lower loads, suggesting that WLTC and AMVA cycles may lead to comparable emissions factors. In contrast to the WLTC and AMVA, the Colombian cycle shows a more uniform distribution of operating points throughout the covered engine speeds. Lastly, the AMVA cycle with slope (AMVA+S) exhibits a high number of operating points concentrated at high loads, which is a direct consequence of the road grade inclusion.

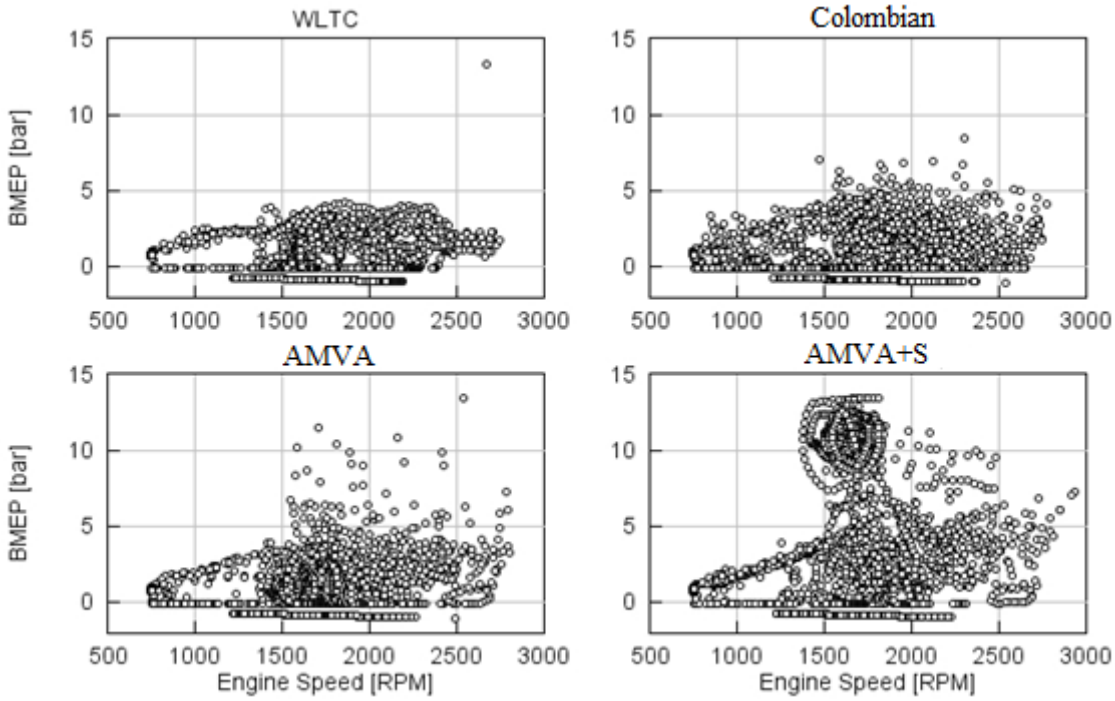

Figure 72. Operating points (OP) required by the vehicle model to follow each driving cycle.

3.5.2.1 Regulated emissions and fuel consumption

Figure 73-80 compare the simulated fuel consumption and emission factors of regulated and unregulated emissions using NBR gear strategy for all fuels and driving cycles. A slight increase in fuel consumption, lower than 3% in all cases, was found with the use of B20 while HVO showed a slightly better fuel economy decreasing up to 1%. National driving cycles lead to higher fuel consumption, with an average increase (considering all fuels) of 7.8%, 36.3% and 156.3% for AMVA, Colombian and AMVA+S DC, respectively, compared to the WLTC. As shown in Figure 69, national driving cycles include many more stop-and-go phases than the WLTC. These frequent stops and accelerations can lead to higher fuel consumption because the engine operates less efficiently during idling conditions (see Figure 54). Moreover, the inclusion of road grade has a higher impact on fuel consumption as it imposes a higher load on the engine, and more fuel is demanded to overcome the forces and maintain the speed [139].

In order to examine the statistical significance of the obtained results, multifactor ANOVA analysis was performed. The ANOVA analysis investigated three real-world factors, namely, Gear strategy, driving cycle and fuel type. P-values less than 0.05 indicate a statistically significant effect on the compared quantity, with respect to the use of ULSD, at the 95.0% confidence level. The comparisons for B20 and HVO20 were done separately to the baseline (ULSD)

It was found that DC ($p = 0.0000$) and B20 ($p = 0.0001$) are statistically significant for fuel consumption, while HVO ($p = 0.537$) is not.

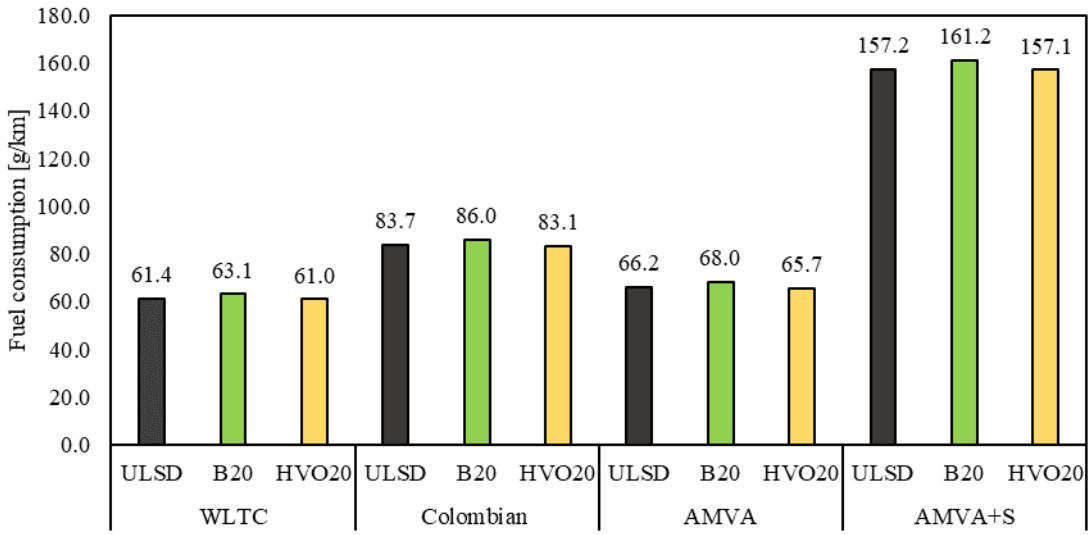

Figure 73. Simulated fuel consumption and comparison between fuels under the studied driving cycles.

There was no significant effect of B20 and HVO20 on CO_2 emissions (**Figure *74***), with differences in CO_2 emissions of less than 1.3 % for all driving cycles. This was confirmed by ANOVA analysis ($p = 0.0710$) and ($p = 0.41$) for B20 and HVO20, respectively, which showed that fuel type was not statistically significant. Since there is a good correlation between CO_2 emissions and fuel consumption, similar trends were observed for local driving cycles compared to the WLTC, with an average increase of 8.2%, 36.9% and 165.2% for AMVA, Colombian and AMVA+S driving cycles, respectively. The gap between local driving cycles and standard driving cycles is consistent with other reports, with CO_2 emissions 3-41% higher for local DC, and even three times higher when road grade is included. [16], [140]. CO emissions (**Figure *75***) showed a similar trend to CO_2 and fuel consumption, increasing by 5.9%, 33.2% and 111.4%, for AMVA, Colombian and AMVA+S, respectively compared to the WLTC, and with maximum decreases of 2% for HVO and 0.4% for B20. The effect of B20 ($p = 0.9657$) and HVO20 ($p = 0.27$) on CO emissions was not statistically significant. Local driving cycles were statistically significant for CO_2 and CO emissions ($p = 0.0000$).

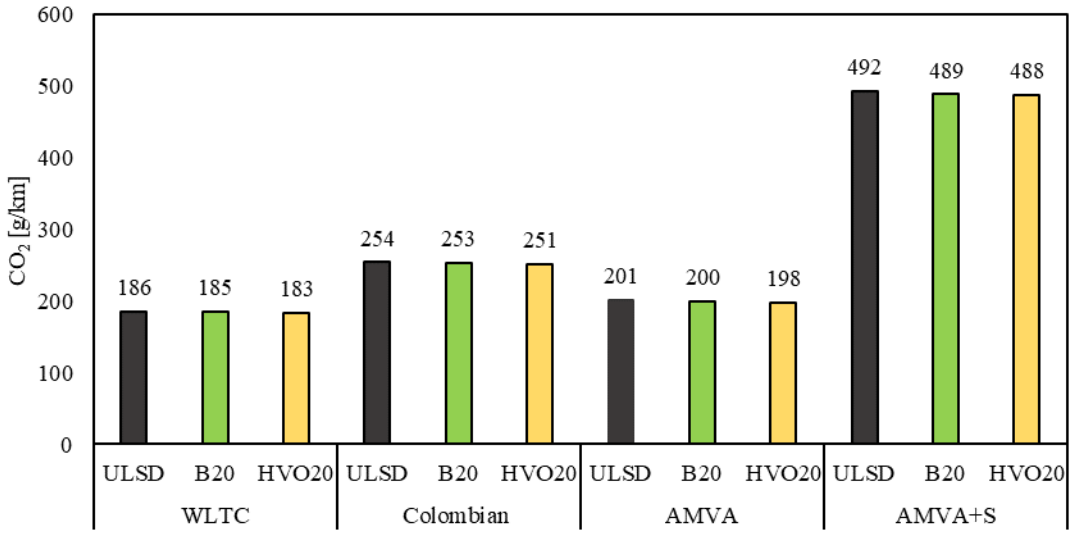

Figure 74. Simulated emission factors of CO2 and comparison between fuels under the studied driving cycles.

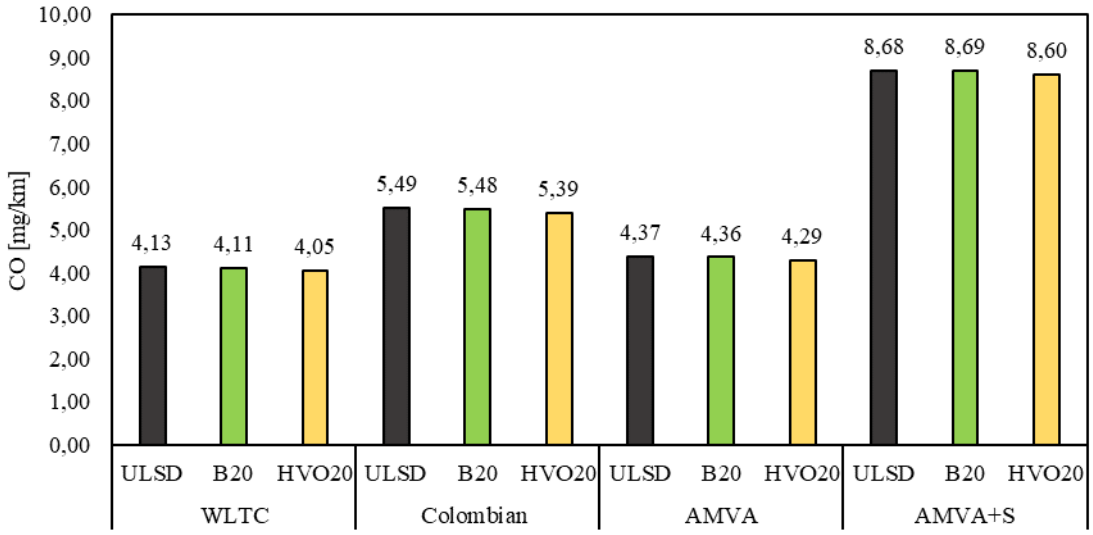

Figure 75. Simulated emission factors of CO and comparison between fuels under the studied driving cycles.

NOx emissions increased significantly for the local DC ($p = 0.000$), namely, 11%, 37.8% and 190.3% for AMVA, Colombian and AMVA+S driving cycles, respectively. High concentration of operating conditions (OC) in the mid-range engine speeds and higher loads (see Figure 72) explains the markedly higher NOx emissions in AMVA+S cycle (see **Figure *76***). NOx emissions were increased with the use of B20. While the change was small in the cycles without slope (up to 3.6%), the effect of the slope was evident, increasing up to 15.6%. These findings are consistent with exhibited B20 behavior in Engine maps (Figure 59), with an increase in NOx for most of the OC.

HVO20 leads to increased NOx emissions in all cases except for AMVA+S, which shows high concentrations of OC below 2000 rpm. As shown in Figure 57, NOx emissions tend to decrease

under these conditions, thus reducing NOx emissions by 0.7%. In contrast, WLTC, Colombian and AMVA resulted in increased NOx emissions of up to 1.2%. Despite the differences shown in all cases, both B20 ($p = 0.05$) and HVO20 ($p = 0.6729$) effects on NOx emissions were not statistically significant

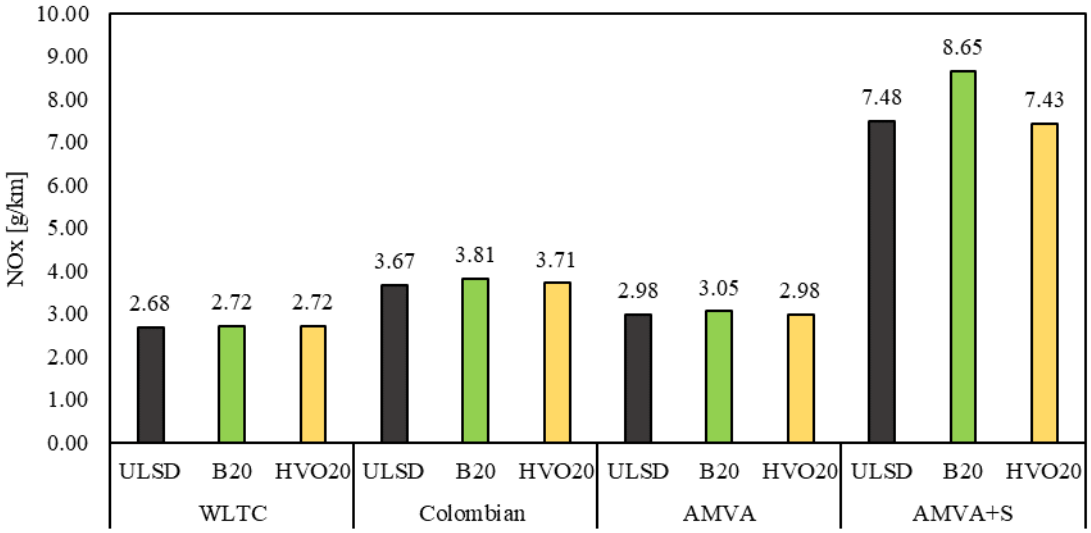

Figure 76. Simulated emission factors of NOx and comparison between fuels under the studied driving cycles.

HC emissions increase for Colombian DC respect to WLTC by 15.7%, and decrease by 10.3 and 39.6%, for AMVA and AMVA+S, respectively, the high loads region demanded in AMVA +S being the one with lowest HC concentration due to the improved combustion fostered by higher residence times at high temperatures, as seen in the emission maps (Figure 60). B20 and HVO20 had a significant positive impact on HC emissions, reducing these pollutants from 12.3 to 20.5% and 15.6 to 19.5%, respectively. ANOVA analysis shows that DC ($p = 0.0000$) and fuel type, B20 ($p = 0.0003$) and HVO20 ($p = 0.0003$), are statistically significant for HC emissions. This result reflects the conclusion drawn from **Figure** *77*, where local DCs were the most influential factor for the variation in CO emissions.

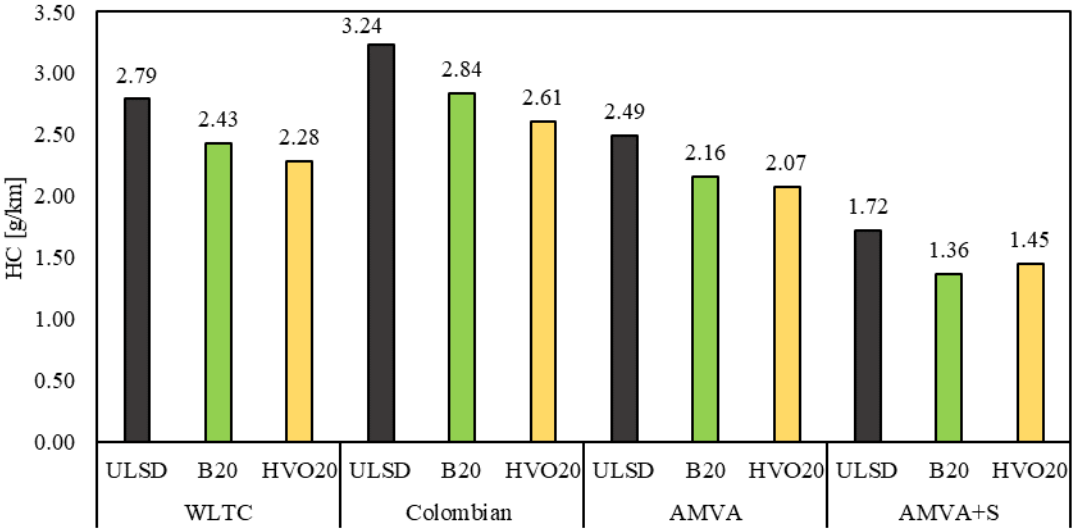

Figure 77. Simulated emission factors of HC and comparison between fuels under the studied driving cycles.

Effect of DCs on PN emissions (Figure 78) showed similar trends to CO_2 and fuel consumption, increasing by 1.7 %, 34.0% and 79.6% for AMVA, Colombian and AMVA+S driving cycles, respectively. B20 leads to significant reduction in PN emissions in all cases, from 27.2 to 34.6%, AMVA+S presenting the lowest PN emissions of the other local DCs, which indicates that the benefits of biodiesel are best achieved in AMVA+S. The higher in-cylinder temperature at high loads enhances PN emission reduction, as suggested by [141] who also found that biodiesel causes larger decreases in PN emissions at the higher load conditions. On the other hand, HVO20 had a smaller favorable impact on these emissions compared with B20, with a PN reduction up to 5.3% for AMVA DC. ANOVA analysis shows that DC ($p = 0.0000$) and fuel type, B20 ($p = 0.0001$) are statistically significant for PN emissions, but HVO20 ($p = 0.0876$) is not.

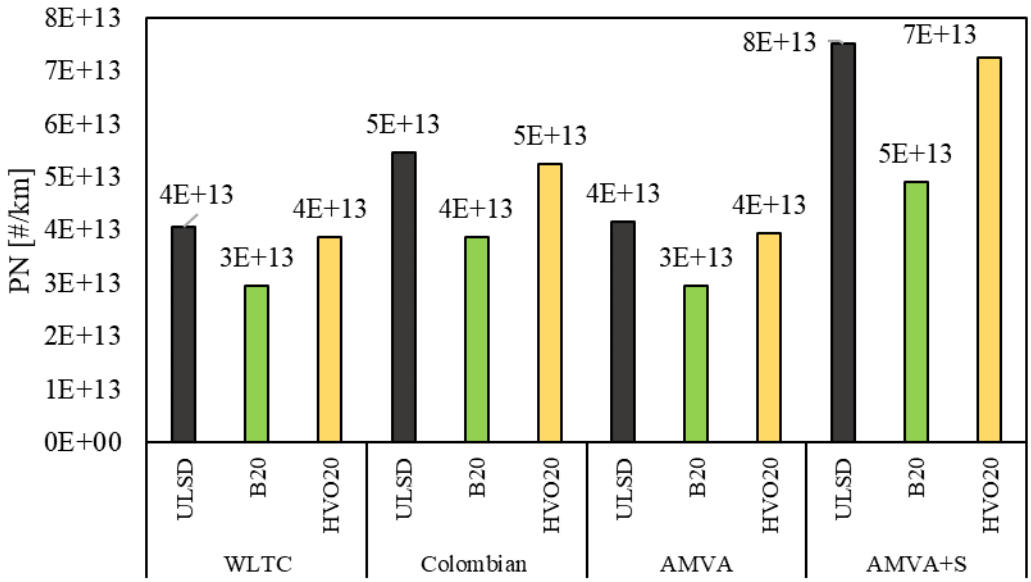

Figure 78. Simulated emission factors of PN and comparison between fuels under the studied driving cycles.

Colombian and AMVA+S DCs increased total PAH emissions up to 24.5% and 19.8%, respectively, (**Figure *79***) compared to WLTC, while AMVA showed a slightly smaller difference. B20 and HVO20 decreased PAH emissions in a similar proportion for cycles without slope, by up to 33.2% and 58.2%, respectively, compared to WLTC. A3 is not visible in the figure because of its lowest values.

A2 and A4 showed different trends. While A4 followed similar trends to CO and fuel consumption, A2 trends were similar to HC emissions. This may be due to the effect of load and speed, as discussed before. Higher loads and speeds may increase A4 emissions because more fuel is needed [123]. A2 showed the opposite trend, with higher concentrations at low speeds and loads because these species decompose more quickly at high in-cylinder temperatures [124]. Therefore, AMVA+S had higher emissions of A2 and lower emissions of A4. ANOVA analysis showed that DC ($p = 0.0001$), B20 ($p = 0.0000$), and HVO20 ($p = 0.0001$) had a statistically significant effect on PAH emissions.

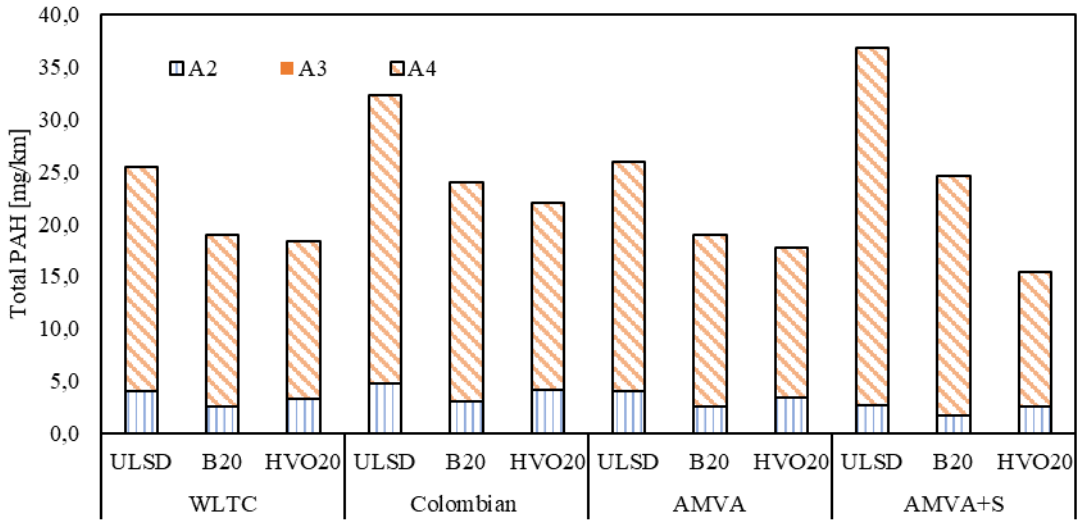

Figure 79. Simulated emission factors of PAHs and comparison between fuels under the studied driving cycles.

Benzene emissions increase for Colombian DC by 13.8% and decrease for AMVA with and without slope by 48.3 and 12.9%, respectively (**Figure *80***), while Toluene increases for Colombian DC by 14.8% and decreases for AMVA with and without slope by 59.4 and 20.4%, respectively (**Figure *81***). As mentioned before, the higher concentration of OC at high loads demanded in AMVA+S leads the overall decrease in BTX emissions, because higher loads enhance oxidation of BTX due to higher temperatures [131]. B20 decreases Benzene in all cases up to 24% and toluene up to 35.8%. On the other hand, HVO20 showed improved reduction of Benzene emissions up to 38.2% and toluene up to 94.3%. ANOVA analysis showed that DC, B20 and HVO had statistically significant effects on Benzene and Toluene emissions (DC with $p = 0.0001$ and 0.0059, respectively; B20 and HVO with $p = 0.0000$ in all cases).

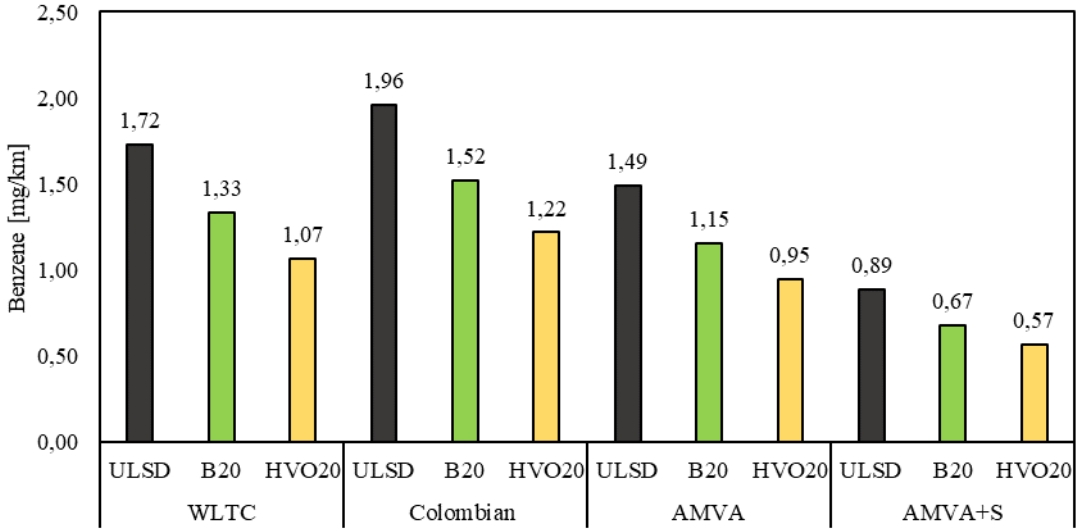

Figure 80. Simulated emission factors of Benzene and comparison between fuels under the studied driving cycles.

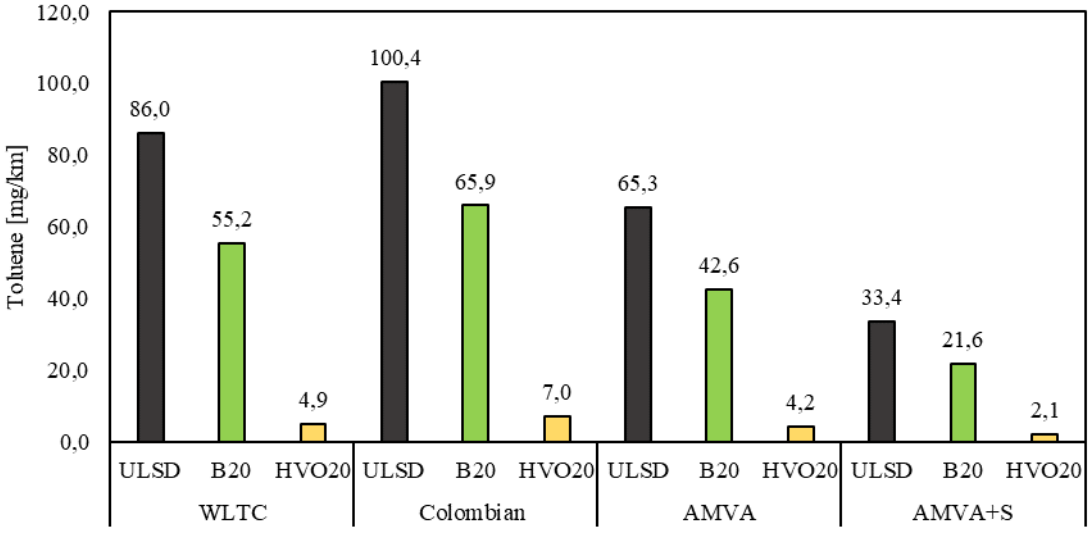

Figure 81. Simulated emission factors of Toluene and comparison between fuels under the studied driving cycles.

Formaldehyde increases for Colombian DC by 12% and decreases for AMVA with and without slope by 52.5 and 11.8%, respectively, (**Figure *82***). B20 decreases Formaldehyde (up to 7.9 % in all cases) may be related to a high concentration of OC in all DCs (Figure 65 and 70) in regions where formaldehyde emissions decrease with the use of B20. Although Biodiesel blends tend to increase this emission according to some authors, others report that biodiesels help reduce carbonyl emissions or even not significant differences were observed between fuels [6]. HVO20 decreases Formaldehyde in all cases up to 92.4 %. ANOVA analysis showed that DC ($p = 0.0001$),

B20 (p = 0.0000), and HVO20 (p = 0.0035) had a statistically significant effect on Formaldehyde emissions.

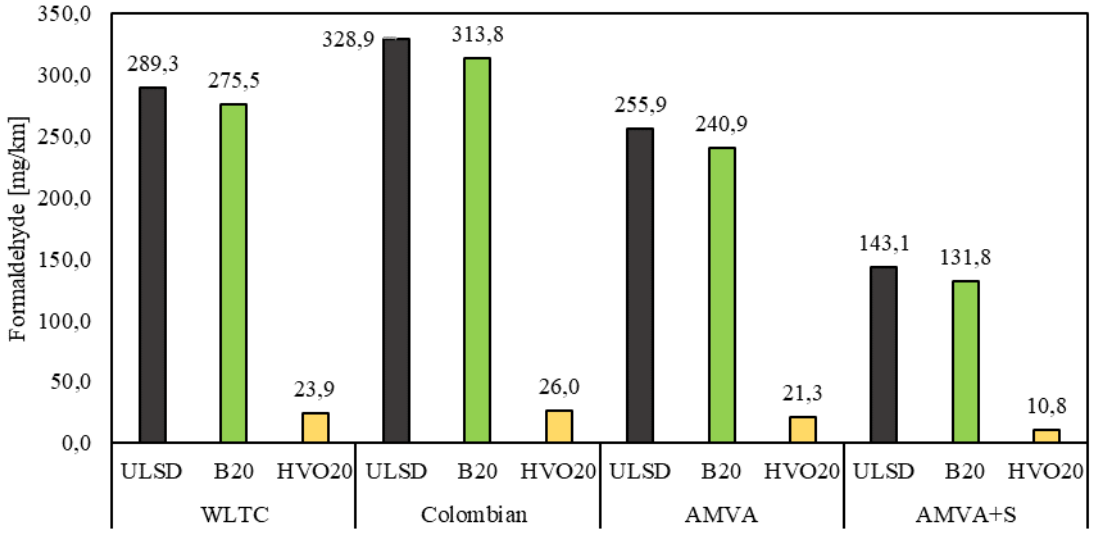

Figure 82. Simulated emission factors of Formaldehyde and comparison between fuels under the studied driving cycles.

Overall, the results suggest that the choice of fuel type, driving cycle, and additional factors (such as slope) significantly impact vehicle emissions and fuel consumption. The use of biodiesel (B20) and hydrotreated vegetable oil (HVO20) generally result in reduced emissions of CO, HC, and particulate number (PN), while the effect on NOx and CO_2 was not significant.

Regarding unregulated emissions, B20 decreased polycyclic aromatic hydrocarbon (PAH) emissions by up to 33.2% without significantly impacting carbonyl emissions. HVO20 showed a more pronounced effect, reducing PAH emissions by up to 58.2% and carbonyl emissions by up to 92.5%.

The AMVA+S driving cycle with slope inclusion (AMVA+S slope) exhibited the most significant differences in emissions between tested fuels for all measured species. This scenario also resulted in the highest overall emissions across all fuels. These findings emphasize the importance of considering multiple factors when evaluating the environmental impact of various fuels and driving conditions.

Summary

Considering the large amount of information presented, a summary is included with the most relevant results of this research.

This study successfully implemented a CI engine model within GT-Suite software. The model predicted various combustion parameters using a DI-pulse combustion approach, including IMEP (Indicated Mean Effective Pressure) and CA50 (crank angle at 50% cumulative heat release). While most predicted values exhibited acceptable levels of error, some cases, particularly at low engine speeds, showed higher discrepancies.

The model demonstrated good agreement with experimental data for key parameters. The simulated peak in-cylinder pressure closely matched real-world measurements, and the predicted in-cylinder burn rates aligned well with the crank angle data. Additionally, CO2 emissions predictions displayed a strong correlation with measured values for both ULSD (Ultra-Low Sulfur Diesel) and B20 biodiesel blend. Most results fell within established error targets or close to the upper limits.

The correlation for NOx emissions was less pronounced compared to CO2, but the model still met accuracy requirements and successfully captured the emission trends for both B20 and ULSD. The provided correlation (R) and determination (R^2) coefficients indicated strong relationships for parameters like IMEP and CA50, signifying a good match between model predictions and experimental data. Some discrepancies observed in B20 model predictions, particularly higher errors in performance parameters, were attributed to inherent model simplifications. Overall, validation against experimental data revealed good agreement for most parameters, with R^2 values often exceeding 0.90. This suggests the model's effectiveness in predicting engine behavior and emissions across various operating conditions.

To simulate unregulated species like polycyclic aromatic hydrocarbons (PAHs) including benzene, toluene (BT), and formaldehyde, a second predictive combustion model named DISRM was required. Its calibration involved determining the most suitable mechanism and surrogates for the tested fuels. Various mechanisms were evaluated for ULSD (Ultra-Low Sulfur Diesel). Mechanism 2 proposed by Wang et al., with 109 species and 543 reactions, was chosen due to its lower errors in predicting parameters like CA50, peak pressure, NOx, and CO2 emissions. Mechanisms for biodiesel (B100) were also evaluated. Mechanism 1 proposed by Luo et al., with 115 species and 460 reactions, was selected because it exhibited similar errors to mechanism 2 but required less simulation time. Following the pre-selection of mechanisms for ULSD and BD (Biodiesel), this study implemented the merging of these mechanisms into a single, comprehensive one. Subsequently, the most suitable surrogates for ULSD, B20, and HVO20 were determined.

Three surrogates for ULSD were found to be acceptable. Surrogate 1 (82.2% n-Heptane and 17.8% Toluene, mass composition) showed the lowest errors in performance parameters and NOx emissions prediction.

Surrogates for B20 were evaluated, and Surrogate 2 (5.9% Methyl decanoate, 5.3% Metil-9-decenoato, 74.8% n-Heptane and 14.0% Toluene, mass composition) was selected because it displayed better agreement with experimental ignition timing and had a closer match to the cetane number.

The performance of DISRM was evaluated using consistency checks and simulation results. For both ULSD and B20, most cases were within acceptable limits for parameters like CA50 and peak pressure. However, some discrepancies were observed in NOx and CO_2 emissions, especially for B20, indicating the challenges in modeling biodiesel blends. DISRM demonstrated similar errors to the DI pulse model in IMEP, CA50, and peak pressure, suggesting a strong capability in combustion prediction. However, the challenges associated with modeling biodiesel blends were highlighted, especially in predicting CO_2 and NOx emissions. The results showed that the model generally performed well in replicating combustion parameters and emissions, but challenges remained in predicting emissions for biodiesel blends such as B20. Additionally, the choice of surrogates and mechanisms significantly influenced the model performance.

The simulated BTE for all fuels showed similar trends, namely, an increase in engine load resulted in improved BTE. This improvement is likely due to higher loads allowing the engine to operate closer to its peak thermal efficiency, resulting in higher air-to-fuel ratios and more complete combustion. B20 and HVO20 showed a slight increase in BTE compared to ULSD. HVO20 exhibited slightly higher thermal efficiency. The BSFC exhibited a high correlation with BTE. Lower BSFC values were observed under the same speed and load conditions as higher BTE. Higher speeds and lower loads resulted in higher BSFC, consistent with the literature. B20 and HVO20 had different effects on BSFC: B20 caused an increase in BSFC due to its higher energy density, while HVO20 caused a decrease in BSFC because of its lower energy density. There were no significant differences in VE between the three fuels. Engine model did not capture the effects of biodiesel and HVO on mechanical efficiency due to the simplicity of the friction model. The literature suggests that biodiesel tends to have a positive effect on mechanical efficiency because of its lubricity properties, reducing friction between engine components. In contrast, HVO, with low lubricity, may have a negative impact. Generally, η_m decreases at higher speeds due to higher frictional losses, while higher loads often result in better combustion efficiency and more useful work, favoring mechanical efficiency.

Higher engine speeds and loads led to increased CO_2 emissions due to the higher fuel consumption required to produce the necessary power output, B20 leading to a slight maximum increase of 1.35% in CO_2 emissions at speeds lower than 1500 rpm and loads between 4 and 10 bar. This is mainly due to its higher oxygen content, which enhances the oxidation of CO to CO_2. At higher speeds, there is a reduction in CO_2 emissions of up to 2.11% with B20 and 1.35% with HVO20. NOx emissions increase by 1-20% for B20 in almost all operating conditions. This increase is attributed to higher in-cylinder temperatures during combustion and the higher oxygen content in biodiesel molecules. The effect of HVO20 on NOx emissions is dependent on the operation conditions, with decrease of up to 3.7% at lower speeds and increase of up to 1% at higher speeds. The absence of oxygen and aromatics in HVO20 prevents NOx formation, while its high cetane number may promote NOx formation. Higher HC and CO emissions are observed at higher speeds and loads due to higher fuel requirements and less efficient combustion. B20 significantly reduces HC emissions by up to 70.2% at high loads, and HVO20 also reduces HC emissions under almost all operating conditions, with reductions of up to 8.4%. B20 and HVO20 had similar effects on CO emissions, with a change of -5.44 to 3.52% under most operating conditions. These changes are attributed to the shorter ignition delay and higher oxygen content in biodiesel, which enhance the combustion process.

Several conclusions can be drawn regarding unregulated emissions and their response to different fuels under steady state conditions. Higher engine speeds tend to increase A3 and A4 emissions, possibly due to incomplete combustion at lower residence times. A2, on the other hand, shows

higher concentrations at low speeds and loads. B20 and HVO20 generally reduce PAH emissions. Biodiesel reduced A4 emissions by up to 60% for almost all speed and load combinations, whereas A3 and A2 are reduced by up to 100%. HVO20 decreases PAH emissions, with reductions of up to 50%. These reductions are attributed to factors such as oxygen enrichment and lower content of PAH precursors in biodiesel and the absence of aromatics in HVO, which contribute to lower PAH emissions.

Benzene emissions tend to increase at lower loads and speeds, with the highest concentrations at idle speed. Toluene emissions follow similar trends but with the highest concentrations at speeds between 2000 and 2500 rpm. B20 and HVO20 generally reduce benzene and toluene emissions. This complex behavior is attributed to the interplay of factors such as exhaust temperature and oxygen enrichment in biodiesel. Formaldehyde emissions tend to decrease with increasing load, with a slight increase with speed from idle speed to 2000 rpm followed by a decrease from 2000 to 3500 rpm. This decrease is attributed to high in-cylinder temperatures at higher speeds and loads. B20 increases formaldehyde emissions under specific speed and load conditions, up to 159.8% at certain points. This behavior is linked to the fuel oxygen content and the formation of short-chain carbonyl compounds. HVO20 generally reduces formaldehyde emissions, with reductions ranging from 30 to 100%.

PN emissions show similar trends to A3 and A4 emissions, increasing at higher loads and speeds due to incomplete combustion. B20 results in the lowest PN emissions, with a drop of 5 to 37% in most speed and load conditions. This reduction is attributed to factors such as oxygen enrichment, reduced carbon content, and the higher cetane number of biodiesel. HVO20 shows a slight reduction (up to 5%) in PN emissions, but no clear conclusion can be drawn regarding its effect on PN emissions, as it depends on the operation mode.

The engine model provided insights into how different fuels (ULSD, B20 and HVO20) impact unregulated emissions, including PAH, BT, formaldehyde, and PN emissions. The effects are influenced by engine speed, load, and various fuel properties. While B20 and HVO20 generally exhibit positive effects on reducing these emissions, there are complex interactions and exceptions depending on specific operating conditions and the composition of the fuels used. The results highlight the importance of considering unregulated emissions under different operating conditions when assessing the environmental impacts of different fuels in internal combustion engines.

Regarding to the vehicle model, the results indicate excellent agreement between the target and actual speeds, with correlation (R) and determination (R2) coefficients of 0.999 for all driving cycles, demonstrating the model ability to accurately follow the driving cycles. The model demonstrated good accuracy in simulating NOx and CO_2 emissions when compared to experimental data. For NOx emissions, the DI-pulse-based vehicle model showed good agreement with experimental values, with errors below 11% for all tested fuels and within the experimental uncertainty range.

Simulated PAH emissions exhibited larger differences compared to experimental data due to limitations in the model. The predicted emissions maps represent in-cylinder conditions at exhaust valve opening and neglect post-combustion effects and interactions within the exhaust system, which significantly influence PAH formation. Despite these limitations, the model captured the trend of reduced PAH emissions with Biodiesel (BD) compared to Ultra-Low Sulfur Diesel (ULSD), consistent with experimental findings. However, the model may not fully capture the

effect of Hydrotreated Vegetable Oil (HVO20) on light PAHs, although the trend of decreasing heavier PAHs aligns with experimental data.

Significant differences were found between experimental and simulated fuel consumption, with errors of up to 37%. However, the simulated trends matched the experimental trends, showing slight increases for B20 and decreases for HVO20, which reflects their respective energy densities.

For PN emissions, experimental results showed increases with B20 and HVO20, while simulated emissions factors exhibited decreases. The experimental uncertainty range did not enable a clear conclusion about the effect on PN, but other studies have reported reductions with BD.

In summary, the vehicle model demonstrated accuracy in simulating key emissions such as NOx and CO_2, but it exhibited larger discrepancies in simulating unregulated emissions (PAH) and fuel consumption. While the model captured some of the effects of BD and HVO20, it also showed areas where further refinement and consideration of post-combustion effects may be necessary to align better with experimental data.

Local driving cycles, such as AMVA and Colombian, exhibit more scattered distributions of operating conditions and higher load requirements compared to the World Harmonized Light Vehicle Test Cycle (WLTC). This dispersion in operating conditions in local driving cycles can be attributed to their stop-and-go nature. WLTC and AMVA driving cycles have similarities in their operating conditions, with a concentration of operating points in the mid-range of engine speed and lower loads. Colombian driving cycle, on the other hand, shows a more uniform distribution of operating points across engine speeds. The AMVA with a slope includes a high number of operating points concentrated at high loads due to the slope conditions.

B20 results in a slight increase in fuel consumption of less than 3%, while HVO20 shows a slight improvement in fuel economy, reducing fuel consumption by up to 1%. National driving cycles (AMVA, Colombian, AMVA+S) lead to higher fuel consumption, with increases ranging from 7.8% to 156.3% compared to WLTC, primarily due to the frequent stop-and-go phases and road gradients in local driving cycles. Multifactor ANOVA analysis indicates that driving cycles and the use of B20 are statistically significant factors affecting fuel consumption, while the use of HVO20 does not show statistical significance on fuel consumption. On the other hand, there is no significant effect of B20 and HVO20 on CO_2 emissions. The differences in CO_2 emissions between the fuels are less than 1.3% for all driving cycles; local driving cycles increase CO_2 emissions ranging from 8.2% to 165.2% compared to WLTC. Local driving cycles have a statistically significant impact on CO and HC emissions, leading to increased emissions compared to WLTC. HC emissions increase for the Colombian driving cycle by 15.7% and decrease for AMVA with and without slope by 39.6 and 10.3%, respectively. B20 and HVO20 significantly reduce HC emissions, with reductions ranging from 12.3% to 20.5% and 15.6% to 19.5%, respectively. Driving cycles and the use of B20 and HVO20 are statistically significant factors on HC emissions. NOx emissions increase significantly for local driving cycles, with up to 190.3% higher NOx emissions for AMVA+S. B20 and HVO20 show varied effects on NOx emissions, with increases in cycles without slope (up to 3.6%) and more substantial effects on slopes (up to 15.6%). Local driving cycles lead to an increase in PN emissions, ranging from 1.7% to 79.6%. B20 significantly reduces PN emissions in all cases, with reductions ranging from 27.2% to 34.6%. HVO20 has a smaller favorable impact on PN emissions, with reductions up to 5.3%. Both driving cycles and the use of B20 are statistically significant factors affecting PN emissions, while the use of HVO20 does not show statistical significance.

Colombian and AMVA+S driving cycles increase total PAH emissions by 24.5% and 19.8%, respectively, compared to WLTC. B20 and HVO20 decrease total PAH emissions in regular cycles by up to 33.2% and 58.2%, respectively. Driving cycles, the use of B20, and the use of HVO20 are statistically significant factors affecting PAH emissions. The effect of driving cycles on Benzene and Toluene emissions varies. Benzene increases for the Colombian driving cycle but decreases for AMVA with and without slope. Toluene increases for the Colombian driving cycle but decreases for AMVA with and without slope. B20 significantly reduces Benzene and Toluene emissions in all cases, while HVO20 shows more substantial reductions. Driving cycles and the use of B20 and HVO20 are statistically significant factors affecting Benzene and Toluene emissions. Formaldehyde emissions increase for the Colombian driving cycle but decrease for AMVA with and without slope. B20 reduces Formaldehyde emissions in all cases. HVO20 significantly decreases Formaldehyde emissions. Driving cycles, the use of B20, and the use of HVO20 are statistically significant factors affecting Formaldehyde emissions.

Chapter 4. Conclusions and future work

4.1 Conclusions

A methodology was developed for simulating emissions of regulated pollutants (CO, CO_2, and NOx) and unregulated pollutants (PAH, carbonyls, and PN) from a diesel engine using biodiesel/diesel and HVO/diesel mixtures. This methodology involves literature review, collection of input data, experimental measurements, model construction, model calibration and validation, and, finally, results analysis. One of the primary challenges in developing the model is gathering input data. While a substantial amount of data is available from various sources, some specific parameters, such as valve lift profiles, pulse ejection time and mass, and injection profiles, may be difficult to acquire. However, the simplification inherent to one-dimensional models and the inclusion of multiple adjustment parameters allow to overcome these challenges. On the other hand, the quality of the experimental data plays a crucial role in ensuring a successful calibration process. Therefore, meticulous equipment, fine-tuning procedures, and verification of repeatable measurements are essential. Another aspect of great relevance is the combustion model, in particular the software used GT-Suit allows for choosing different options according to the requirements and results that are intended to be achieved. The use of the DI-Pulse model offers a solution with a good capacity of prediction of combustion parameters and engine performance, with the advantage of a low computational cost, which makes it viable to evaluate many operating conditions, but it is limited to the prediction of regulated species. On the other hand, the DISRM model offers a solution based on kinetic mechanisms, demanding more computational resources but with the major advantage of including a wide variety of unregulated species, which are currently of great interest due to their potential toxicity. One of the challenges of this model is the need for representative kinetic mechanisms and fuel surrogates. No kinetic mechanisms that allow the simulation of biodiesel-diesel and HVO-diesel blends and that have also been validated under engine conditions were found in the literature. Thus, a merged mechanism was used, but its exhaustive validation was outside the scope of this project.

The developed engine DI-pulse model demonstrates the ability to predict regulated emissions and performance parameters with good precision. It effectively captures the effects of biodiesel-diesel blends and HVO-diesel blends up to 20% by volume. However, predicting unregulated emissions using the DISRM, usually present in trace amounts, remains challenging, as it requires considering various phenomena that occur in exhaust systems and aftertreatment units, which were not addressed in this project. Nevertheless, the effects of biodiesel addition on these contaminants appear reasonable. On the other hand, the low computational cost associated with these models enabled the generation of engine performance and emissions maps under a wide range of operating conditions. These maps can serve as input data in a vehicle model with a quasi-transitional solution, permitting the evaluation of emissions under driving conditions that closely resemble real-world scenarios.

The model developed for the vehicle has a good capacity to predict emission factors under transient conditions, showing a good correlation between the simulated and experimental results. The simulation of the different fuel blends and transient operating conditions studied in the project let to observe the impact of each variable on polluting emissions, showing not only the influence of type of fuel but that driving conditions have a significant impact. Particularly, the road grade had the most significant effect, the driving cycle with slope showing the highest emissions with all fuels and for all the species observed. It was found that Colombian driving cycles and the use

of B20 and HVO20 are statistically significant factors affecting most of the regulated and unregulated emissions. The use of B20 led to a decrease of 27 – 35% in PN emissions, and 12 – 20.5% in HC emissions with respect to ULSD, while the effect was not significant in CO and CO_2, and a slight increase in NOx emissions was observed. The use of B20 decreased PAH emissions by up to 33.2%, while it did not have a significant impact on carbonyl emissions. The use of HVO20 did not have a significant impact on CO, CO_2, NOx and PN emissions, while a positive impact was observed on HC emissions, with reductions ranging between 15.6% and 19.5%. Finally, the use of HVO20 decreased PAH emissions by up to 58.2%, and carbonyl emissions by up to 92.5%.

Based on the results obtained in this project, the use of blends of biodiesel and renewable diesel (HVO) up to 20% vol does not affect the performance in terms of fuel efficiency or combustion properties, such as heat release rate and pressures, which allows the use of the engine without modification. However, this study did not perform wear tests on parts and other material properties, and the effect of these blends on the durability of mechanical parts, filter change and wear on polymeric parts should also be studied.

4.2 Future work

The proposed research plan outlines several exciting steps to improve understanding and optimize the use of biodiesel (BD) and hydrotreated vegetable oil (HVO) as fuels. Here's a breakdown of each point:

1. Studying New Fuel Blends:

This investigates blends with a higher concentration of the studied compounds (presumably those identified in previous research). Analyzing these blends can reveal their impact on engine performance and emissions compared to lower concentration blends.

Additionally, testing pure BD and pure HVO will provide valuable insights into their individual characteristics and potential challenges.

2. Engine Model Refinement:

This focuses on improving the accuracy of the existing engine model. Two key areas are highlighted:

Alternative Surrogates: Developing more representative surrogates for diesel-biodiesel and diesel-HVO mixtures will enhance the model's ability to predict emissions from these fuels.

Implementing a DISRM approach for the full engine model can provide a more detailed picture of the combustion process within the engine. This can lead to a better understanding of how these fuels affect engine behavior.

3. Engine Model Calibration:

This step involves calibrating the engine model using experimental data obtained from running an engine on an HVO20 blend (20% HVO, 80% diesel). This calibration ensures the model accurately reflects real-world behavior with this specific blend.

4. Pure HVO Tests for Reaction Kinetics:

Studying pure HVO will provide valuable data for understanding the reaction kinetics, which is the study of how fast chemical reactions occur during combustion. This information can be used to improve the models used to predict engine performance and emissions with HVO blends.

5. Considering Exhaust Systems and Aftertreatment Units:

This expands the research scope to include the effect of exhaust systems and aftertreatment units on unregulated emissions. Unregulated emissions are pollutants not currently subject to strict regulations but can still have environmental and health impacts. This will provide a more comprehensive picture of the overall environmental impact of these fuels.

Chapter 5. References

[1] J. Unosson *et al.*, “Acute cardiovascular effects of controlled exposure to dilute Petrodiesel and biodiesel exhaust in healthy volunteers: a crossover study,” 2021. doi: 10.1186/s12989-021-00412-3.

[2] A. A. Mehus *et al.*, “Comparison of Acute Health Effects from Exposures to Diesel and Biodiesel Fuel Emissions,” *J Occup Environ Med*, vol. 57, no. 7, pp. 705–712, 2015, doi: 10.1097/JOM.0000000000000473.

[3] D. Singh *et al.*, “A Comprehensive Review on 1st-Generation Biodiesel Feedstock Palm Oil: Production, Engine Performance, and Exhaust Emissions,” Mar. 01, 2021, *Springer*. doi: 10.1007/s12155-020-10171-2.

[4] M. N. Ashraf *et al.*, “Sustainability of Palm Biodiesel in Transportation: a Review on Biofuel Standard, Policy and International Collaboration Between Malaysia and Colombia,” 2020, doi: 10.1007/s12155-020-10165-0/Published.

[5] H. Aatola, M. Larmi, and T. Sarjovaara, “Hydrotreated Vegetable Oil (HVO) as a Renewable Diesel Fuel : Trade-off between NO x , Particulate Emission , and Fuel Consumption of a Heavy Duty Engine,” vol. 1, no. 1, 2008.

[6] C. Patel, J. Hwang, C. Bae, and A. K. Agarwal, “Review of Regulated, Unregulated and Particulate Emissions from Biodiesel Fuelled Compression Ignition Engines,” Dec. 01, 2022, *Korean Society of Automotive Engineers*. doi: 10.1007/s12239-022-0154-3.

[7] C. Lim, J. Lee, J. Hong, C. Song, J. Han, and J. S. Cha, “Evaluation of regulated and unregulated emissions from a diesel powered vehicle fueled with diesel/biodiesel blends in Korea,” *Energy*, vol. 77, pp. 533–541, 2014, doi: 10.1016/j.energy.2014.09.040.

[8] R. Williams, R. Pettinen, P. Ziman, K. Kar, and R. Dauphin, “Fuel effects on regulated and unregulated emissions from two commercial euro v and euro vi road transport vehicles,” *Sustainability (Switzerland)*, vol. 13, no. 14, pp. 1–38, 2021, doi: 10.3390/su13147985.

[9] G. Karavalakis, S. Stournas, and E. Bakeas, “Light vehicle regulated and unregulated emissions from different biodiesels,” *Science of the Total Environment*, vol. 407, no. 10, pp. 3338–3346, 2009, doi: 10.1016/j.scitotenv.2008.12.063.

[10] G. Karavalakis, E. Bakeas, and S. Stournas, “Influence of oxidized biodiesel blends on regulated and unregulated emissions from a diesel passenger car,” *Environ Sci Technol*, vol. 44, no. 13, pp. 5306–5312, 2010, doi: 10.1021/es100831j.

[11] Y. Chen and J. Borken-Kleefeld, “Real-driving emissions from cars and light commercial vehicles - Results from 13 years remote sensing at Zurich/CH,” *Atmos Environ*, vol. 88, pp. 157–164, 2014, doi: 10.1016/j.atmosenv.2014.01.040.

[12] R. Suarez-Bertoa *et al.*, “On-road emissions of passenger cars beyond the boundary conditions of the real-driving emissions test,” *Environ Res*, vol. 176, Sep. 2019, doi: 10.1016/j.envres.2019.108572.

[13] S. Lopp, E. Wood, and A. Duran, “Evaluating the Impact of Road Grade on Simulated Commercial Vehicle Fuel Economy Using Real-World Drive Cycles,” in *SAE Technical Papers*, SAE International, 2015. doi: 10.4271/2015-01-2739.

[14] H. Achour and A. G. Olabi, “Driving cycle developments and their impacts on energy consumption of transportation,” *J Clean Prod*, vol. 112, pp. 1778–1788, Jan. 2016, doi: 10.1016/j.jclepro.2015.08.007.

[15] M. Tutuianu *et al.*, “Development of a World-wide Worldwide harmonized Light duty driving Test Cycle (WLTC),” 2013.

[16] A. Gebisa, G. Gebresenbet, R. Gopal, and R. B. Nallamothu, “Driving Cycles for Estimating Vehicle Emission Levels and Energy Consumption,” *Future Transportation*, vol. 1, no. 3, pp. 615–638, Nov. 2021, doi: 10.3390/futuretransp1030033.

[17] M. Giraldo and J. I. Huertas, “Real emissions, driving patterns and fuel consumption of in-use diesel buses operating at high altitude,” *Transp Res D Transp Environ*, vol. 77, pp. 21–36, Dec. 2019, doi: 10.1016/j.trd.2019.10.004.

[18] J. I. Huertas, J. Díaz, D. Cordero, and K. Cedillo, “A new methodology to determine typical driving cycles for the design of vehicles power trains,” *International Journal on Interactive Design and Manufacturing*, vol. 12, no. 1, pp. 319–326, Feb. 2018, doi: 10.1007/s12008-017-0379-y.

[19] Grupo Manejo Eficiente de la Energía [GIMEL] and Unidad de Planeación Minero Energética [UPME], “Informe final de convenio FECOC+,” 2020. Accessed: Jun. 06, 2022. [Online]. Available: https://www1.upme.gov.co/DemandayEficiencia/Documents/Informe_final_FECOC.pdf

[20] B. T. Kannan and P. S. Srivathsan, “Numerical simulation of spark ignition engine using OpenFOAM®,” *Perspect Sci (Neth)*, vol. 8, pp. 13–15, 2016, doi: 10.1016/j.pisc.2016.01.004.

[21] P. Pal, Y. Wu, T. Lu, S. Som, Y. C. See, and A. Le Moine, “Multidimensional numerical simulations of knocking combustion in a cooperative fuel research engine,” *Journal of Energy Resources Technology, Transactions of the ASME*, vol. 140, no. 10, 2018, doi: 10.1115/1.4040063.

[22] P. Pal *et al.*, “Development of a Virtual CFR Engine Model for Knocking Combustion Analysis,” *SAE Int J Engines*, vol. 11, no. 6, pp. 1069–1082, 2018, doi: 10.4271/2018-01-0187.

[23] G. Fernando, G. Sánchez, and A. Chaves, “Modelling of combustion in Diesel engines: a review of the state of the art,” 2013. [Online]. Available: https://www.researchgate.net/publication/262459144

[24] T. D. ve D. B. Dergisi, “Investigation of performance characteristics using Stochastic Reactor Model in a biodiesel pilot-fueled natural gas engine,” *Archives of Anesthesiology and Critical Care*, vol. 4, no. 4, pp. 527–534, 2019.

[25] H. Omidvarborna, A. Kumar, and D. S. Kim, “Prediction of NOx emissions from a simplified biodiesel surrogate by applying stochastic simulation algorithms (SSA),” *Combustion Theory and Modelling*, vol. 21, no. 2, pp. 346–357, 2017, doi: 10.1080/13647830.2016.1235729.

[26] J. Van Gerpen, *Basics of Diesel Engines and Diesel Fuels*, Second Edi. AOCS Press, 2010. doi: 10.1016/B978-1-893997-62-2.50008-5.

[27] J. B. Heywood, *Internal Combustion Engine Fundamentals, 2nd Edition*, 2nd ed. 2018 McGraw-Hill Education, 2018.

[28] P. M. Merritt, V. Ulmet, R. L. Mccormick, W. E. Mitchell, and K. J. Baumgard, "Regulated and Unregulated Exhaust Emissions Comparison for Three Tier II Non-Road Diesel Engines Operating on Ethanol-Diesel Blends," 2005.

[29] A. K. Agarwal *et al.*, "Unregulated emissions and health risk potential from biodiesel (KB5, KB20) and methanol blend (M5) fuelled transportation diesel engines," *Renew Energy*, vol. 98, pp. 283–291, 2016, doi: 10.1016/j.renene.2016.03.058.

[30] V. L. Chumakov, S. N. Devyanin, and A. V. Bijaev, "Nitrogen oxide formation with nonuniform fuel distribution in diesel engine," *J Phys Conf Ser*, vol. 1679, no. 5, 2020, doi: 10.1088/1742-6596/1679/5/052089.

[31] B. S. Haynes and H. G. Wagner, "Soot formation," *Prog Energy Combust Sci*, vol. 7, no. 4, pp. 229–273, 1981, doi: 10.1016/0360-1285(81)90001-0.

[32] C. Chen and X. Jiang, "Molecular dynamics simulation of soot formation during diesel combustion with oxygenated fuel addition," 2020. doi: 10.1039/d0cp01917h.

[33] S. Sahay, *Handbook of Biofuels*. 2022. doi: 10.1016/C2019-0-04999-0.

[34] A. Datta and B. K. Mandal, "A comprehensive review of biodiesel as an alternative fuel for compression ignition engine," *Renewable and Sustainable Energy Reviews*, vol. 57, pp. 799–821, 2016, doi: 10.1016/j.rser.2015.12.170.

[35] J. Ghazanfari, B. Najafi, S. Faizollahzadeh Ardabili, and S. Shamshirband, "Limiting factors for the use of palm oil biodiesel in a diesel engine in the context of the ASTM standard," *Cogent Eng*, vol. 4, no. 1, 2017, doi: 10.1080/23311916.2017.1411221.

[36] S. Radhakrishnan, Y. Devarajan, A. Mahalingam, and B. Nagappan, "Emissions analysis on diesel engine fueled with palm oil biodiesel and pentanol blends," *J Oil Palm Res*, vol. 29, no. 3, pp. 380–386, 2017, doi: 10.21894/jopr.2017.2903.11.

[37] M. S. Gad, R. El-Araby, K. A. Abed, N. N. El-Ibiari, A. K. El Morsi, and G. I. El-Diwani, "Performance and emissions characteristics of C.I. engine fueled with palm oil/palm oil methyl ester blended with diesel fuel," *Egyptian Journal of Petroleum*, vol. 27, no. 2, pp. 215–219, 2018, doi: 10.1016/j.ejpe.2017.05.009.

[38] J. Agudelo, E. Gutiérrez, and P. Benjumea, "Experimental combustion analysis of a hsdi diesel engine fuelled with palm oil biodiesel-diesel fuel blends," *Combustion*, pp. 103–113, 2009, Accessed: Jul. 17, 2022. [Online]. Available: https://repositorio.unal.edu.co/bitstream/handle/unal/26376/13046-35919-1-PB.pdf?sequence=1

[39] J. Agudelo, I. Bedoya, and A. Agudelo, "Emisiones gaseosas y opacidad del humo de un motor operando con bajas concentraciones de biodiesel de palma," *Ingeniería y desarrollo: revista de la División de Ingeniería de la Universidad del Norte*, no. 18, pp. 1–22, 2005.

[40] J. Agudelo, P. Benjumea, and A. P. Villegas, "Evaluation of nitrogen oxide emissions and smoke opacity in a HSDI diesel engine fuelled with palm oil biodiesel," *Revista Facultad de Ingenieria*, no. 51, pp. 69–78, 2010.

[41] J. R. Agudelo, A. F. Agudelo, and I. G. Cuadrado, “Análisis de primera y segunda ley de un motor operando con biodiesel de aceite de palma,” *Energetica*, vol. 35, pp. 1–8, 2006.

[42] J. R. Agudelo S., A. F. Agudelo S., and J. F. Pérez B., “Caracterización de la combustión del biodiesel de aceite de palma en un motor diesel Characterization of the combustion of palm oil biodiesel combustión in a diesel engine,” *Revista Energía y Computación*, vol. 15, no. 1, pp. 37–44, 2007.

[43] S. Arias, F. Molina, and J. R. Agudelo, “Palm oil biodiesel : An assessment of PAH emissions , oxidative potential and ecotoxicity of particulate matter,” *Journal of Environmental Sciences*, vol. 101, pp. 326–338, 2021, doi: 10.1016/j.jes.2020.08.022.

[44] C. J. Hor *et al.*, “Techno-economic assessment of hydrotreated vegetable oil as a renewable fuel from waste sludge palm oil,” *Environ Res*, vol. 220, Mar. 2023, doi: 10.1016/j.envres.2022.115169.

[45] A. Dimitriadis, I. Natsios, A. Dimaratos, and D. Katsaounis, “Evaluation of a Hydrotreated Vegetable Oil (HVO) and Effects on Emissions of a Passenger Car Diesel Engine,” vol. 4, no. July 2018, pp. 1–19, 2020, doi: 10.3389/fmech.2018.00007.

[46] O. Shepel, J. Matijošius, A. Rimkus, K. Duda, and M. Mikulski, “Research of parameters of a compression ignition engine using various fuel mixtures of hydrotreated vegetable oil (Hvo) and fatty acid esters (fae),” *Energies (Basel)*, vol. 14, no. 11, 2021, doi: 10.3390/en14113077.

[47] F. Millo, T. Vlachos, and A. Piano, “Physicochemical and mutagenic analysis of particulate matter emissions from an automotive diesel engine fuelled with fossil and biofuel blends,” *Fuel*, vol. 285, no. July 2020, p. 119092, 2021, doi: 10.1016/j.fuel.2020.119092.

[48] C. Paul, K. Jin, N. Fogla, K. Roggendorf, and S. Wahiduzzaman, “A Zero-Dimensional Velocity-Composition-Frequency Probability Density Function Model for Compression-Ignition Engine Simulation,” *SAE Technical Papers*, vol. 2020-April, no. April, pp. 1–17, 2020, doi: 10.4271/2020-01-0659.

[49] A. Matrisciano, T. Franken, L. C. Gonzales Mestre, A. Borg, and F. Mauss, “Development of a computationally efficient tabulated chemistry solver for internal combustion engine optimization using stochastic reactor models,” *Applied Sciences (Switzerland)*, vol. 10, no. 24, pp. 1–31, 2020, doi: 10.3390/app10248979.

[50] H. Li, W. Yang, D. Zhou, and W. Yu, “Numerical study of the effects of biodiesel unsaturation on combustion and emission characteristics in diesel engine,” *Appl Therm Eng*, vol. 137, pp. 310–318, 2018, doi: 10.1016/j.applthermaleng.2018.03.066.

[51] T. L. C. C. Novaes, J. R. Henríquez, and A. A. V. Ochoa, “Numerical simulation of the performance of a diesel cycle operating with diesel-biodiesel mixtures,” *Energy Convers Manag*, vol. 180, no. November 2018, pp. 990–1000, 2019, doi: 10.1016/j.enconman.2018.11.039.

[52] U. Rajak and T. N. Verma, “A comparative analysis of engine characteristics from various biodiesels: Numerical study,” *Energy Convers Manag*, vol. 180, no. August 2018, pp. 904–923, 2019, doi: 10.1016/j.enconman.2018.11.044.

[53] R. D. Reitz, “Directions in internal combustion engine research,” *Combust Flame*, vol. 160, no. 1, pp. 1–8, 2013, doi: 10.1016/j.combustflame.2012.11.002.

[54] A. Malik, J. Schramm, C. Nielsen, and T. Lovas, “Development of surrogate for fischer-tropsch biofuel and reduced mechanism for combustion in diesel engine,” *SAE Technical Papers*, vol. 11, 2013, doi: 10.4271/2013-01-2599.

[55] J. Y. W. Lai, K. C. Lin, and A. Violi, “Biodiesel combustion: Advances in chemical kinetic modeling,” *Prog Energy Combust Sci*, vol. 37, no. 1, pp. 1–14, 2011, doi: 10.1016/j.pecs.2010.03.001.

[56] F. Zhao *et al.*, “Numerical study of soot particles from low temperature combustion of engine fueled with diesel fuel and unsaturation biodiesel fuels,” *Appl Energy*, vol. 211, no. May 2017, pp. 187–193, 2018, doi: 10.1016/j.apenergy.2017.11.056.

[57] X. Cheng, H. K. Ng, S. Gan, J. H. Ho, and K. M. Pang, “Development and validation of a generic reduced chemical kinetic mechanism for CFD spray combustion modelling of biodiesel fuels,” *Combust Flame*, vol. 162, no. 6, pp. 2354–2370, 2015, doi: 10.1016/j.combustflame.2015.02.003.

[58] H. M. Ismail, H. K. Ng, S. Gan, T. Lucchini, and A. Onorati, “Development of a reduced biodiesel combustion kinetics mechanism for CFD modelling of a light-duty diesel engine,” *Fuel*, vol. 106, pp. 388–400, 2013, doi: 10.1016/j.fuel.2012.10.015.

[59] S. Arias *et al.*, “Environmental and health risk implications of unregulated emissions from advanced biofuels in a Euro 6 engine,” *Chemosphere*, vol. 313, Feb. 2023, doi: 10.1016/j.chemosphere.2022.137462.

[60] J. J. Hernández, J. Sanz-Argent, and E. Monedero-Villalba, “A reduced chemical kinetic mechanism of a diesel fuel surrogate (n-heptane/toluene) for HCCI combustion modelling,” *Fuel*, vol. 133, pp. 283–291, Oct. 2014, doi: 10.1016/j.fuel.2014.05.029.

[61] H. Wang, M. Yao, Z. Yue, M. Jia, and R. D. Reitz, “A reduced toluene reference fuel chemical kinetic mechanism for combustion and polycyclic-aromatic hydrocarbon predictions,” *Combust Flame*, vol. 162, no. 6, pp. 2390–2404, Jun. 2015, doi: 10.1016/j.combustflame.2015.02.005.

[62] S. Ren, S. L. Kokjohn, Z. Wang, H. Liu, B. Wang, and J. Wang, “A multi-component wide distillation fuel (covering gasoline, jet fuel and diesel fuel) mechanism for combustion and PAH prediction,” *Fuel*, vol. 208, pp. 447–468, 2017, doi: 10.1016/j.fuel.2017.07.009.

[63] W. Yu, F. Zhao, W. Yang, K. Tay, and H. Xu, “Development of an optimization methodology for formulating both jet fuel and diesel fuel surrogates and their associated skeletal oxidation mechanisms,” *Fuel*, vol. 231, pp. 361–372, Nov. 2018, doi: 10.1016/j.fuel.2018.05.121.

[64] Y. Bai, Y. Wang, X. Wang, and P. Wang, “Development of a skeletal mechanism for tri-component diesel surrogate fuel: N-hexadecane/iso-cetane/1-methylnaphthalene,” *Fuel*, vol. 259, Jan. 2020, doi: 10.1016/j.fuel.2019.116217.

[65] Z. Luo *et al.*, “A reduced mechanism for biodiesel surrogates for compression ignition engine applications,” *Fuel*, vol. 99, pp. 143–153, Sep. 2012, doi: 10.1016/j.fuel.2012.04.028.

[66] J. L. Brakora and R. D. Reitz, “Investigation of NOx predictions from biodiesel-fueled HCCI engine simulations using a reduced kinetic mechanism,” in *SAE Technical Papers*, SAE International, 2010. doi: 10.4271/2010-01-0577.

[67] L. Zhang, X. Ren, and Z. Lan, “A reduced reaction mechanism of biodiesel surrogates with low temperature chemistry for multidimensional engine simulation,” *Combust Flame*, vol. 212, pp. 377–387, Feb. 2020, doi: 10.1016/j.combustflame.2019.11.002.

[68] Y. Bai, Y. Wang, and X. Wang, “Development of a skeletal mechanism for four-component biodiesel surrogate fuel with PAH,” *Renew Energy*, vol. 171, pp. 266–274, Jun. 2021, doi: 10.1016/j.renene.2021.02.054.

[69] V. Vijayakrishnan and K. Masoom, “Predictive Diesel Combustion Using DI-Pulse in GT-Power,” 2015. [Online]. Available: http://publications.lib.chalmers.se/records/fulltext/225450/225450.pdf

[70] Gamma Technologies LLC, “GT-SUITE Engine Performance Application Manual,” 2022.

[71] J. McCrady, A. Hansen, and C. F. Lee, “Modeling biodiesel combustion using GT-power,” *2007 ASABE Annual International Meeting, Technical Papers*, vol. 12 BOOK, no. 07, 2007, doi: 10.13031/2013.23435.

[72] M. Y. T. Rafidah Rahim, Rizalman Mamat, “Comparative Study of Biofuel and Biodiesel Blend with Mineral Diesel Using One-Dimensional Simulation Comparative Study of Biofuel and Biodiesel Blend with Mineral Diesel Using One-Dimensional Simulation,” 2011, doi: 10.1088/1757-899X/36/1/012009.

[73] K. S. Varde and S. K. Veeramachineni, “Simulation of combustion in a di diesel engine operating on biodiesel blends,” in *ASME 2011 International Mechanical Engineering Congress and Exposition, IMECE 2011*, 2011, pp. 1–7. doi: 10.1115/imece2011-64504.

[74] M. Farid, M. Said, M. Said, and A. Abdul, “Modelling of Diesel Engine fuelled with biodiesel using Engine Simulation Software,” vol. 313, no. Imat 2011, pp. 307–313, 2012, doi: 10.1063/1.4704231.

[75] I. Yahuza, H. Dandakouta, and M. H. I. | D. Y. Dasin, “Modelling and Simulation of Some Combustion Parameters Intport-1 and Intvalve-1 using Gt-Power Engine Simulation Software with Biodiesel-Ethanol-Diesel Blends as Fuel,” *International Journal of Trend in Scientific Research and Development*, vol. Volume-3, no. Issue-1, pp. 1206–1214, 2018, doi: 10.31142/ijtsrd19188.

[76] D. F. Ruan, W. L. Cheng, and C. F. Lee, “Comparison of performance and combustion characteristics of diesel fuel and vegetable oils in di diesel engine,” *SAE Int J Fuels Lubr*, vol. 1, no. 1, pp. 1049–1055, 2009, doi: 10.4271/2008-01-1639.

[77] H. P. Liu, S. Strank, M. Werst, R. Hebner, and J. Osara, “Combustion emissions modeling and testing of conventional diesel fuel,” in *ASME 2010 4th International Conference on Energy Sustainability, ES 2010*, 2010. doi: 10.1115/ES2010-90037.

[78] S. Ahmadipour, M. H. Aghkhani, and J. Zareei, “Investigation of injection timing and different fuels on diesel engine performance and emissions,” *Journal of Computational and Applied Research in Mechanical Engineering*, vol. 9, no. 2, pp. 385–396, 2020, doi: 10.22061/jcarme.2019.4143.1497.

[79] S. Saurabh, N. Hawes, and T. Hemami, “An evaluation of process to model Hydrotreated Vegetable Oil (HVO) using GT-Power,” in *Global GT Conference 2021*, 2021, pp. 1–10. doi: 10.13140/RG.2.2.30057.36967.

[80] E. G. Giakoumis and G. Triantafillou, “Analysis of the effect of vehicle, driving and road parameters on the transient performance and emissions of a turbocharged truck,” *Energies (Basel)*, vol. 11, no. 2, 2018, doi: 10.3390/en11020295.

[81] H. C. Watson, E. E. Milkins, M. O. Preston, C. Chittleborough, and B. Alimoradian, “Predicting fuel consumption and emissions-transferring chassis dynamometer results to real driving conditions,” *SAE Technical Papers*, 1983, doi: 10.4271/830435.

[82] L. Pelkmans, P. Debal, T. Hood, G. Hauser, and M. R. Delgado, “Development of a simulation tool to calculate fuel consumption and emissions of vehicles operating in dynamic conditions,” *SAE Technical Papers*, no. 724, 2004, doi: 10.4271/2004-01-1873.

[83] C. Ericson, B. Westerberg, and R. Egnell, “Transient emission predictions with quasi stationary models,” *SAE Technical Papers*, no. 724, 2005, doi: 10.4271/2005-01-3852.

[84] Z. Gao, J. C. Conklin, C. S. Daw, and V. K. Chakravarthy, “A proposed methodology for estimating transient engine-out temperature and emissions from steady-state maps,” *International Journal of Engine Research*, vol. 11, no. 2, pp. 137–151, 2010, doi: 10.1243/14680874JER05609.

[85] M. Tutuianu *et al.*, “Development of a World-wide Worldwide harmonized Light duty driving Test Cycle (WLTC) Draft Technical Report UN / ECE / WP . 29 / GRPE / WLTP-IG DHC subgroup,” 2013. [Online]. Available: https://www2.unece.org/wiki/download/attachments/9798086/WLTP-DHC-18-06e.doc?api=v2

[86] J. R. Agudelo Santamaría, “Informe final Entregable 2 de 4 Ciclos de conducción de vehículos ligeros y motocicletas para el Valle de Aburrá,” 2017. Accessed: Apr. 02, 2022. [Online]. Available: https://www.metropol.gov.co/ambiental/calidad-del-aire/Biblioteca-aire/Estudios-calidad-del-aire/Ciclos-conduccion-AMVA.pdf

[87] CAPELEC, “CAP3010 SMART CAP.” Accessed: Feb. 18, 2022. [Online]. Available: https://www.capelec.com/es

[88] CAPELEC, “FICHA TECNICA ANALIZADOR DE GASES CAPELEC.” Accessed: Feb. 18, 2022. [Online]. Available: https://www.capelec.com/es

[89] S. Amanatidis, L. Ntziachristos, Z. Samaras, K. Janka, and J. Tikkanen, “Applicability of the Pegasor particle sensor to measure particle number, mass and PM emissions,” *SAE Technical Paper 2013-24-0167, 2013*, vol. 6, 2013, doi: 10.4271/2013-24-0167.

[90] A. Leonardo and S. Torres, “IMPLEMENTACIÓN DE UN SISTEMA DE ADQUISICIÓN DE DATOS BASADO EN FPGA PARA EL MONITOREO Y CONTROL DE MOTORES DE COMBUSTIÓN INTERNA,” 2019. Accessed: Jul. 18, 2022. [Online]. Available: https://bibliotecadigital.udea.edu.co/handle/10495/15165

[91] A. F. A. Santamaría, J. R. A. Santamaría, and P. N. Benjumea Hernández, *Diagnóstico de la combustión de biocombustibles en motores*. Medellín : Universidad de Antioquia , 2007. Accessed: Mar. 18, 2022. [Online]. Available: https://descubridor.minagricultura.gov.co/buscador/Record/ir-123456789-80397

[92] B. Mason, W. Bradley, and A. Pezouvanis, “Repeatable steady-state measurement of particulate number emissions in engine experiments,” *International Journal of Engine Research* , 2016, doi: 10.1177/1468087416643667.

[93] T. A *et al.*, “Particle Measurement Programme (PMP),” no. KJ-NA-29277-EN-N, 2018, doi: 10.2760/859241.

[94] T. Yokoi, M. Shinzawa, and Y. Matsumoto, “Measurement repeatability improvement for particle number size distributions from diesel engines,” *JSAE Review*, vol. 22, pp. 545–551, 2001, doi: 10.1016/s0389-4304(01)00136-9.

[95] A. F. Agudelo, J. R. Agudelo, and P. N. Benjumea, “CARIBE - Programa para el diagnóstico de combustión en motores Diésel. Manual científico,” 2007.

[96] Cummins, “Calificación de Servicio Completa ISF 2.8 & ISF 3.8 CM2220,” 2014.

[97] R. Payri, F. J. Salvador, M. Carreres, and J. De La Morena, “Fuel temperature influence on the performance of a last generation common-rail diesel ballistic injector. Part II: 1D model development, validation and analysis,” *Energy Convers Manag*, vol. 114, pp. 376–391, 2016, doi: 10.1016/j.enconman.2016.02.043.

[98] S. N. Krivtsov, I. V. Yakimov, and S. P. Ozornin, “Numerical analysis and experimental studies on solenoid common rail diesel injector with worn control valve,” in *IOP Conference Series: Materials Science and Engineering*, Institute of Physics Publishing, Apr. 2018. doi: 10.1088/1757-899X/327/4/042057.

[99] B. Giechaskiel, M. Cresnoverh, H. Jörgl, and A. Bergmann, “Calibration and accuracy of a particle number measurement system,” *Meas Sci Technol*, vol. 21, no. 4, 2010, doi: 10.1088/0957-0233/21/4/045102.

[100] X. Wang, X. Jing, X. Gu, T. Gao, L. Wu, and B. Hao, “Future Regulation-based Particle Number Emission Characteristics for a Heavy-duty Diesel Engine,” in *IOP Conference Series: Earth and Environmental Science*, IOP Publishing Ltd, Oct. 2021. doi: 10.1088/1755-1315/859/1/012087.

[101] G. Piñeiro, S. Perelman, J. P. Guerschman, and J. M. Paruelo, “How to evaluate models: Observed vs. predicted or predicted vs. observed?,” *Ecol Modell*, vol. 216, no. 3–4, pp. 316–322, Sep. 2008, doi: 10.1016/j.ecolmodel.2008.05.006.

[102] E. F. Andric, Jelena, Daniel Schimmel, Anton D. Sediako, Jonas Sjoblom, “Development and Calibration of One Dimensional Engine Model for Hardware-In-The-Loop Applications,” *SAE Technical Papers*, 2018, doi: 10.4271/2018-01-0874.Abstract.

[103] L. R. Uppalapati, B. Vernham, and Y. Wei, “Development and validation of engine calibration using 1d predictive models,” in *SAE Technical Papers*, SAE International, Apr. 2019. doi: 10.4271/2019-01-1135.

[104] Gamma Technologies LLC, “Vehicle Driveline and HEV Application Manual GT-SUITE,” 2022.

[105] “Target Normas: ABNT NBR 6601 NBR6601 Veículos rodoviários.” Accessed: Jun. 06, 2024. [Online]. Available: https://www.normas.com.br/visualizar/abnt-nbr-nm/2995/nbr6601-veiculos-rodoviarios-automotores-leves-determinacao-de-hidrocarbonetos-monoxido-de-carbono-oxidos-de-nitrogenio-dioxido-de-carbono-e-material-particulado-no-gas-de-escapamento

[106] E. Özgül and H. Bedir, “Fast NO x emission prediction methodology via one-dimensional engine performance tools in heavy-duty engines,” *Advances in Mechanical Engineering*, vol. 11, no. 4, pp. 1–16, 2019, doi: 10.1177/1687814019845954.

[107] A. Krishnasamy and K. R. Bukkarapu, “A comprehensive review of biodiesel property prediction models for combustion modeling studies,” *Fuel*, vol. 302, no. April, p. 121085, 2021, doi: 10.1016/j.fuel.2021.121085.

[108] M. Yildiz and B. A. Çeper, “Estimation of equilibrium combustion products of diesel-biodiesel fuel blends using the developed solving process for CnHm and CαHβOγ fuel types,” *International Journal of Automotive and Mechanical Engineering*, vol. 14, no. 2, pp. 4332–4347, Jun. 2017, doi: 10.15282/ijame.14.2.2017.16.0345.

[109] H. P. Liu, S. Strank, M. Werst, R. Hebner, and J. Osara, “Combustion emissions modeling and testing of neat biodiesel fuels,” in *ASME 2010 4th International Conference on Energy Sustainability, ES 2010*, 2010. doi: 10.1115/ES2010-90038.

[110] P. Hellier, N. Ladommatos, R. Allan, and J. Rogerson, “Combustion and emissions characteristics of toluene/n-heptane and 1-octene/n-octane binary mixtures in a direct injection compression ignition engine,” *Combust Flame*, vol. 160, no. 10, pp. 2141–2158, Oct. 2013, doi: 10.1016/j.combustflame.2013.04.016.

[111] J. Brakora and R. Reitz, “A comprehensive combustion model for biodiesel-fueled engine simulations,” in *SAE Technical Papers*, SAE International, 2013. doi: 10.4271/2013-01-1099.

[112] A. G. Erman, P. Hellier, and N. Ladommatos, “The impact of ignition delay and further fuel properties on combustion and emissions in a compression ignition engine,” *Fuel*, vol. 262, Feb. 2020, doi: 10.1016/j.fuel.2019.116155.

[113] E. Geo Varuvel, N. Mrad, F. Aloui, and M. Tazerout, “Experimental analysis of biofuel as an alternative fuel for diesel engines Experimental analysis of biofuel as an alternative fuel for diesel engines Experimental analysis of biofuel as an alternative fuel for diesel engines,” *Appl Energy*, vol. 94, pp. 224–231, 2012, doi: 10.1016/j.apenergy.2012.01.067ï.

[114] Y. Palani, C. Devarajan, D. Manickam, and S. Thanikodi, “Performance and emission characteristics of biodiesel-blend in diesel engine: A review,” 2022. doi: 10.4491/eer.2020.338.

[115] A. Mejiá, M. Leiva, A. Rincón-Montenegro, A. Gonzalez-Quiroga, and J. Duarte-Forero, “Experimental assessment of emissions maps of a single-cylinder compression ignition engine powered by diesel and palm oil biodiesel-diesel fuel blends,” *Case Studies in Thermal Engineering*, vol. 19, p. 100613, 2020, doi: 10.1016/j.csite.2020.100613.

[116] K. Cheikh, A. Sary, L. Khaled, L. Abdelkrim, and T. Mohand, “Experimental assessment of performance and emissions maps for biodiesel fueled compression ignition engine,” *Appl Energy*, vol. 161, pp. 320–329, Jan. 2016, doi: 10.1016/j.apenergy.2015.10.042.

[117] S. Firoz, “A review: Advantages and Disadvantages of Biodiesel,” *International Research Journal of Engineering and Technology*, vol. 04, no. 11, 2017.

[118] S. Saravanan, G. Nagarajan, S. Anand, and S. Sampath, “Correlation for thermal NOx formation in compression ignition (CI) engine fuelled with diesel and biodiesel,” *Energy*, vol. 42, no. 1, pp. 401–410, 2012, doi: 10.1016/j.energy.2012.03.028.

[119] M. Lapuerta, O. Armas, and J. Rodríguez-Fernández, “Effect of biodiesel fuels on diesel engine emissions,” *Prog Energy Combust Sci*, vol. 34, no. 2, pp. 198–223, 2008, doi: 10.1016/j.pecs.2007.07.001.

[120] A. Calle-Asensio, J. J. Hernández, J. Rodríguez-Fernández, M. Lapuerta, A. Ramos, and J. Barba, “Effect of advanced biofuels on WLTC emissions of a Euro 6 diesel vehicle with SCR under different climatic conditions,” *International Journal of Engine Research*, vol. 22, no. 12, pp. 3433–3446, Dec. 2021, doi: 10.1177/14680874211001256.

[121] C. A. Buckner *et al.*, “Diesel Exhaust Emissions and Mitigations,” in *Intech*, vol. 11, 2016, p. 13. [Online]. Available: https://www.intechopen.com/books/advanced-biometric-technologies/liveness-detection-in-biometrics

[122] P. X. Pham, N. V. T. Pham, T. V. Pham, V. H. Nguyen, and K. T. Nguyen, “Ignition delays of biodiesel-diesel blends: Investigations into the role of physical and chemical processes,” *Fuel*, vol. 303, Nov. 2021, doi: 10.1016/j.fuel.2021.121251.

[123] J. Schramm, S. Hori, and T. Abe, “The emission of PAH from a di diesel engine operating on fuels and lubricants with known PAH content,” *SAE Technical Papers (1994)*, no. 412, pp. 65–80, 1994, doi: 10.4271/940342.

[124] H. Yamada *et al.*, “Detailed analysis of diesel vehicle exhaust emissions: Nitrogen oxides, hydrocarbons and particulate size distributions,” *Proceedings of the Combustion Institute*, vol. 33, no. 2, pp. 2895–2902, 2011, doi: 10.1016/j.proci.2010.07.001.

[125] X. Wang, C. Song, G. Lv, J. Song, H. Li, and B. Li, “Evolution of in-cylinder polycyclic aromatic hydrocarbons in a diesel engine fueled with n-heptane and n-heptane/toluene,” *Fuel*, vol. 158, pp. 322–329, Jun. 2015, doi: 10.1016/j.fuel.2015.05.053.

[126] Y. Zhang, D. Lou, Z. Hu, and P. Tan, “Particle number, size distribution, carbons, polycyclic aromatic hydrocarbons and inorganic ions of exhaust particles from a diesel bus fueled with biodiesel blends,” *J Clean Prod*, vol. 225, pp. 627–636, Jul. 2019, doi: 10.1016/j.jclepro.2019.03.344.

[127] C. He, Y. Ge, J. Tan, K. You, X. Han, and J. Wang, “Characteristics of polycyclic aromatic hydrocarbons emissions of diesel engine fueled with biodiesel and diesel,” *Fuel*, vol. 89, no. 8, pp. 2040–2046, 2010, doi: 10.1016/j.fuel.2010.03.014.

[128] H. H. Mi, W. J. Lee, C. B. Chen, H. H. Yang, and S. J. Wu, “Effect of fuel aromatic content on PAH emission from a heavy-duty diesel engine,” *Chemosphere*, vol. 41, no. 11, pp. 1783–1790, 2000, doi: 10.1016/S0045-6535(00)00043-6.

[129] A. R. Collier, M. M. Rhead, C. J. Trier, and M. A. Bell, “Polycyclic aromatic compound profiles from a light-duty direct-injection diesel engine,” *Fuel*, vol. 74, no. 3, pp. 362–367, 1995, doi: 10.1016/0016-2361(95)93468-S.

[130] K. L. Pereira *et al.*, “Technical note: Use of an atmospheric simulation chamber to investigate the effect of different engine conditions on unregulated VOC-IVOC diesel exhaust emissions,” *Atmos Chem Phys*, vol. 18, no. 15, pp. 11073–11096, Aug. 2018, doi: 10.5194/acp-18-11073-2018.

[131] X. J. Man, C. S. Cheung, Z. Ning, L. Wei, and Z. H. Huang, “Influence of engine load and speed on regulated and unregulated emissions of a diesel engine fueled with diesel fuel blended with waste cooking oil biodiesel,” *Fuel*, vol. 180, pp. 41–49, Sep. 2016, doi: 10.1016/j.fuel.2016.04.007.

[132] H. A. Dandajeh, M. Talibi, N. Ladommatos, and P. Hellier, “Influence of combustion characteristics and fuel composition on exhaust PAHs in a compression ignition engine,” *Energies (Basel)*, vol. 12, no. 13, 2019, doi: 10.3390/en12132575.

[133] J. C. Ge and N. J. Choi, “Soot particle size distribution, regulated and unregulated emissions of a diesel engine fueled with palm oil biodiesel blends,” *Energies (Basel)*, vol. 13, no. 21, 2020, doi: 10.3390/en13215736.

[134] I. Bortel, J. Vávra, and M. Takáts, “Effect of HVO fuel mixtures on emissions and performance of a passenger car size diesel engine,” *Renew Energy*, vol. 140, pp. 680–691, Sep. 2019, doi: 10.1016/j.renene.2019.03.067.

[135] J. Preuß, K. Munch, and I. Denbratt, “Performance and emissions of renewable blends with OME3-5 and HVO in heavy duty and light duty compression ignition engines,” *Fuel*, vol. 303, Nov. 2021, doi: 10.1016/j.fuel.2021.121275.

[136] E. B. Bakeas and G. Karavalakis, “Regulated, carbonyl and polycyclic aromatic hydrocarbon emissions from a light-duty vehicle fueled with diesel and biodiesel blends,” *Environmental Sciences: Processes and Impacts*, vol. 15, no. 2, pp. 412–422, 2013, doi: 10.1039/c2em30575e.

[137] S. Hu *et al.*, “Emissions of polycyclic aromatic hydrocarbons (PAHs) and nitro-PAHs from heavy-duty diesel vehicles with DPF and SCR,” *J Air Waste Manage Assoc*, vol. 63, no. 8, pp. 984–996, 2013, doi: 10.1080/10962247.2013.795202.

[138] A. Prokopowicz, M. Zaciera, A. Sobczak, P. Bielaczyc, and J. Woodburn, “The Effects of Neat Biodiesel and Biodiesel and HVO Blends in Diesel Fuel on Exhaust Emissions from a Light Duty Vehicle with a Diesel Engine,” *Environ Sci Technol*, vol. 49, no. 12, pp. 7473–7482, Jun. 2015, doi: 10.1021/acs.est.5b00648.

[139] F. Salihu, Y. K. Demir, and H. G. Demir, “Effect of road slope on driving cycle parameters of urban roads,” *Transp Res D Transp Environ*, vol. 118, May 2023, doi: 10.1016/j.trd.2023.103676.

[140] S. Mafi, A. Kakaee, B. Mashadi, A. Moosavian, S. Abdolmaleki, and M. Rezaei, “Developing local driving cycle for accurate vehicular CO2 monitoring: A case study of Tehran,” *J Clean Prod*, vol. 336, Feb. 2022, doi: 10.1016/j.jclepro.2021.130176.

[141] T. Kaya, O. A. Kutlar, and O. O. Taskiran, “Evaluation of the Effects of Biodiesel on Emissions and Performance by Comparing the Results of the New European Drive Cycle and Worldwide Harmonized Light Vehicles Test Cycle,” *Energies (Basel)*, vol. 11, no. 10, 2018, doi: 10.3390/en11102814.

Appendix 1. Technical details

Chapter 2. Methodology

2.2 Modeling

2.2.1. Engine model

Direct-Injection Diesel Multi-Pulse Model ('EngCylCombDIPulse') [70]**.**

- **Fuel Injection** – Every consecutive occurrence of injecting fuel is characterized as an injection pulse and is individually monitored, distinct from all other pulses. A variable quantity of pulses can be introduced, and there is no inherent differentiation between pilot, main, or post-injection pulses. The fuel injected is integrated into the spray unburned zone.
- **Entrainmen**t – As the spray penetrates, it slows down as the surrounding unburned and burned gases are entrained into the pulse. The intermixing of pulses occurs through entrainment. The position and velocity of each packet are determined using an empirical correlation for spray tip penetration.
  The entrainment rate is determined by applying conservation of momentum and can be modified by the *Entrainment Rate Multiplier (C_{ent})*.
- **Evaporation** – Droplet evaporation is modeled with a coupled solution of heat and mass transfer which appropriately accounts for both diffusion-limited and boiling-limited evaporation.
- **Ignition** – The mixture in each pulse undergoes an ignition delay modeled with an Arrhenius expression which can be modified by the *Ignition Delay Multiplier (C_{ign})*. The ignition delay is calculated separately for each pulse based on the conditions within the pulse, and accounts for entrainment and evaporation within the pulse as well as pulse-to-pulse interactions.
- **Premixed Combustion** – When a pulse ignites, the mixture present at that time is set aside for premixed combustion. The rate of this combustion is assumed to be kinetically limited and can be modified by the *Premixed Combustion Rate Multiplier (C_{pm})*.
- **Diffusion Combustion** – After a pulse ignites, the remaining unmixed fuel and entrained gas in the pulse continue to mix and burn in a primarily diffusion-limited phase. The rate of this combustion can be modified by the *Diffusion Combustion Rate Multiplier (C_{df})*. Diffusion combustion rate is reduced at high loads (long injection duration) due to spray-wall and spray-spray interactions.

Direct-Injection Stochastic Reactor Model ('EngCylCombDISRM')

- **Scalar Mixing Multiplier**: Multiplier to the scalar mixing. Increasing this multiplier will lead to increased scalar mixing among the particles. Typical values are between 1.5 and 3.0.
- **Frequency Decay Constant**: Constant that controls the rate of decay for the turbulent frequency. Typical values are between 1.0 and 2.5. This attribute is only visible when the VCF Turbulence Model is selected.

- **Minimum Frequency Decay Rate:** Constant that defines the minimum rate of decay for the turbulent frequency. Typical values are between 0.25 and 1.25. This attribute is only visible when the VCF Turbulence Model is selected.
- **Cutoff Frequency Multiplier:** Multiplier to the cutoff mixing frequency that determines which particles will participate in scalar mixing. This multiplier can be used to tune the heat release from premixed combustion. Typical values are between 0.5 and 5.0.
- **Dissipation Decay Term Multiplier:** Multiplier to the dissipation decay term. A larger dissipation decay term multiplier will result in lower mixing. Typical values are between 0.5 and 5.0. This attribute is only visible when the Flow Turbulence Model is selected.

2.2.2. Engine model calibration and validation

Direct-Injection Diesel Multi-Pulse Combustion Model (DIPulse) [70]

Consistency checks.

- **Reasonable IMEP**: The integrated IMEP is available as a pressure analysis result and should be greater than the BMEP by an amount appropriate for friction MEP. If the IMEP is not reasonable, there could be inaccuracies in the collected pressure data [70].
- **Cumulative Burn During Compression**: In the compression stroke, fuel combustion should not occur, making any computed fuel burning a sign of input data inaccuracies. While most pressure curves show a slight non-zero apparent burn rate during compression, cumulative burn exceeding 2% of the total fuel is marked as an error [70].
- **Compression Slope**: The slope of the LogP vs. LogV curve, as measured during compression from IVC to combustion start, should maintain a relatively constant value. It should closely align with the polytropic coefficient applicable to the trapped gas. As the piston nears top dead center, this gradient will slightly decrease due to rising gas temperature. In engines directly injecting fuel into the cylinder, the polytropic coefficient closely approximates the one of air (1.4 at 300K, dropping to 1.33 at 1000K) [70].
- **Fraction of Fuel Injected Late:** If there is no sufficient fuel in the cylinder to sustain the predictive burn rate before or during direct injection, the "missing" fuel quantity is monitored and integrated throughout the cycle. This fuel deficit is presented in pressure analysis results as a fraction of the total injected fuel, termed "Fraction of Fuel Injected Late." A value of 0.0 is expected, a fraction larger than 0.02 is indicated as an error [70].
- **Large LHV change required**: The LHV multiplier provides an indication of the cumulative error in the burn rate calculation. If the required LHV adjustment is greater than 5%, it is flagged as an error [70].
- **Combustion efficiency or burned fuel fraction comparison to target:** The adjustment of LHV is performed to align the combustion efficiency or burned fuel fraction at the analysis's conclusion with the desired value (usually 100%, unless specified differently in the 'EngBurnExhMeasure' object). If the code cannot attain the target within a 5% margin, it is marked as an error [70].

Genetic Algorithm

For the search algorithm, the "Genetic Algorithm" option is recommended with the following settings [70]:

Table 27. Recommended settings for search algorithm.

Population size	30
Number of Generations	34
Mutation Rate	0.5
Mutation Rate Distribution Index	15

2.2.3. Vehicle model

The essential templates for the vehicle modeling.

- **EngineMap - Advanced Map-Based Engine Model:** This object is used in GT-SUITE to represent an internal combustion engine through a map-based engine model, using several maps that describe engine performance (power output and friction), fuel consumption, heat rejection, emissions, and other characteristics.
- **Lumped 1D Discrete Ratio Transmission Model:** The object acts to replicate the impact of discrete transmissions on torque amplification and speed reduction. The transmission is conceptualized as having an input and an output side, represented as combined inertias that are kinematically connected through a transmission or gear ratio. Several parameters can be set for each discrete gear, including the gear ratio itself, the inertias on the input and output side, and additional factors such as transmission efficiency and friction torque. This enables a detailed representation of how transmissions influence the performance of the vehicle.
- **ICEController – Map-Based Internal Combustion Engine Simple Controller for Idle and Fuel Cut (Compound):** This compound object is used to simulate engine control functions such as idling, and fuel cut for a variety of conditions. ICEController is recommended for applications where maximizing fuel economy is important, such as when running driving cycles.
- **VehDriverAdvanced – Advanced Driver for Open and Closed Loop Maneuvers:** This template is intended to be used as a vehicle driver who controls accelerator position, brake pedal position, transmission gear number and clutch pedal position. This control component is primarily used for controlling vehicles with manual transmissions as it contains the necessary functions for vehicle launch and shifting.
- **VehicleBody – Vehicle Representation for Longitudinal Vehicle Dynamics**: This object is used to calculate the longitudinal motion of a vehicle, as well as the normal loads on each axle. The vehicle acceleration is calculated from the longitudinal force balance and integrated to calculate vehicle speed, and displacement. The longitudinal force balance includes, on an instantaneous basis, the effect of tractive forces applied at the tires, tire rolling resistance, aerodynamic drag, road grade and curvature, as well as wind velocity and direction.